UNIVERSIDAD NACIONAL DE INGENIERÍA

FACULTAD DE CIENCIAS

TESIS

"CALIBRATION UPDATES IN MINERVA TB2 DETECTOR AS A REFERENCE WORK FOR FUTURE TUNINGS IN NEUTRINO DETECTORS"

PARA OBTENER EL GRADO ACADÉMICO DE MAESTRO EN CIENCIAS EN FÍSICA

ELABORADO POR:

Alberto Edgar Chavarria Rodriguez

ASESORES:

Dr. Carlos Javier Solano Salinas

Dr. Leo Bellantoni

LIMA – PERÚ

2018

Dedication

"Look deep into nature, and then you will understand everything better."

Albert Einstein

I dedicate this work to all those who supported me this whole time; I deeply thank my parents Maria and Jose, my sister Anais the one that always told me to not give up, my uncle Wilder and aunt Rosmery.

Acknowledgements

I would like to thank FONDECYT/CONCYTEC for the support in this Master Program; also FERMILAB for granting this 1 year-internship opportunity, specially the MINERνA Collaboration which I was part of. I would like to thank personally Dr. Jorge Morfin, Dr. Deborah Harris and Dr. Laura Fields for hosting. **Special mention to Dr. Leo Bellantoni that supervised my progress while I stayed around FERMILAB** , my advisor Dr. Javier Solano and all members of the MINERνA Collaboration that helped me a lot when I really needed to get my bearings.

Finally, to my home university UNI, specially to Faculty of Sciences for having me as an Undergrad Student and now as a Master Student. To all my Undergrad and Master Teachers that paved the way to my journey in Physics.

Summary

In the Neutrino Physics Field, a lot of careful measurements are made such as : cross section measurement, neutrino oscillation, atmospheric neutrino,etc. In such experimental measurements one has to get the most accurate numbers as possible but in doing so one meets a lot of constraints and variables. Such is the case of the Test Beam detector (a replica of the full MINERνA detector where we test and compare new targets and devices to put them further in the MINERνA detector). The way we detect some signal in the detector is by using a scintillator material attached to a photomultiplier (when a charged particle passes through the scintillator, this emits a photon of certain spectra and this light works as input for the PMT which uses the photoelectric effect to magnify the signal (gain)), in the same way the PMT is wired to the Data Acquisition System (DAQ) in order to process the raw data to give some human-readable numbers. In ideal laboratory conditions, one would expect to get accurate results just by carefully mount the electronics and understand the theory good enough. But nature likes to fool scientists. While making experiments involving fundamental particles, one uses electronic devices that have quantum and technological limitations. One should not miss the effect of variables such as: temperature, moisture, dark current, etc that could impact over our data. In this work, it was explicitly studied the effect of temperature over a special kind of data called Light Injection, which is a type of data used for calibration purposes. Data was taken in two separate time intervals: April and May-July (2015 data already calibrated) which in between was a shutdown period (sometimes a temporal shutdown is done because cooling purposes, repairs in software/hardware, etc). Two "thermometers" were used to get the temperature. One was a thermometer placed near the Test Beam Detector. The other one is a chip built-in the PMT so that it can tell the temperature at all times. The first thermometer was used as a first approximation assuming that everything in the Test Beam Detector was in thermal equilibrium. The second thermometer that was used shows a more realistic distribution of temperatures throughout the time the data was taken. Finally, plots of Gain vs Temperature are shown. These plots, indeed, tell the temperature effect over the data that was considered in this work. However, this temperature effect over the data was in principle ignored by the manufacturer because by dealing with big amounts of data, one notices that this effect causes a decrease of less than 1% in gain of the data analyzed. Nevertheless, in high-accurate measurements this effect should not be neglected if one pursuits to get as close as possible to that number that nature tries to hide.

Key Words: PMT, Test Beam, Gain, Temperature.

Resumen

En el campo de la Física de Neutrinos se realizan muchas mediciones cuidadosas, tales como: medición de la sección transversal, oscilación de neutrinos, neutrinos atmosféricos, etc. En tales mediciones experimentales, uno tiene que obtener los números más precisos posibles, pero al hacerlo uno se encuentra con muchas restricciones y variables. Tal es el caso del detector "Test Beam" (una réplica del detector MINERνA donde probamos y comparamos nuevos "targets" y dispositivos para ponerlos posteriormente en el detector MINERνA). La forma en que detectamos alguna señal en el detector es mediante el uso de un material centelleador conectado a un fotomultiplicador (cuando una partícula cargada pasa a través del centelleador, este emite un fotón de cierto espectro conocido y esta luz funciona como entrada para el PMT que usa el efecto fotoeléctrico para ampliar la señal (ganancia)), de la misma manera que el PMT está conectado al Sistema de Adquisición de Datos (DAQ) para procesar la data y conseguir numeros que sean entendibles para el humano. En condiciones ideales de laboratorio, uno esperaría obtener resultados precisos simplemente con montar cuidadosamente la electrónica y entender la teoría lo suficientemente bien. Pero a la naturaleza le gusta engañar a los científicos. Al realizar experimentos que involucran partículas fundamentales uno usa dispositivos electrónicos que tienen limitaciones cuánticas y tecnológicas. Uno no debe ignorar el efecto de variables tales como: temperatura , la humedad, la "dark current", etc. que podrían afectar nuestros datos. En este trabajo, se estudió explícitamente el efecto de la temperatura sobre un tipo especial de datos llamado "Inyección de Luz" que es un tipo de datos utilizados para fines de calibración. Se tomó datos en dos intervalos de tiempo separados: Abril y Mayo-Julio (datos de 2015 ya calibrados) donde hubo un período de apagado del detector (a veces se realiza un cierre temporal debido a propósitos de refrigeración, reparaciones en software / hardware, etc.). Se usó dos "termómetros" para obtener la temperatura. Uno era un termómetro colocado cerca del Detector "Test Beam". El otro es un chip incorporado en el PMT para que pueda detectar la temperatura en todo momento. Se usó el primer termómetro como una primera aproximación, suponiendo que todo en el detector "Test Beam" se encontraba en equilibrio térmico. El segundo termómetro que se utilizó, muestra una distribución más realista de las temperaturas a lo largo del tiempo en que se tomaron los datos. Finalmente, se está mostrando gráficas de Ganancia vs Temperatura que, de hecho, indican el efecto de la temperatura sobre los datos que se consideraron en este trabajo. Sin embargo, este efecto de temperatura sobre los datos fue, en principio, ignorado por el fabricante porque al manejar grandes cantidades de datos se nota que este efecto causa menos de 1% de disminución en ganancia de los datos analizados. Sin embargo, en mediciones de alta precisión, este efecto no debe descuidarse si uno intenta acercarse lo más posible a ese número (sección transversal, violacion CP, etc) que la naturaleza intenta esconder.

Palabras Clave: PMT, "Test Beam", Ganancia, Temperatura.

Introduction

In the MINERVνA Test Beam experiment one looks for corrections and calibrations in our detector. The purpose of doing this is to get a better tuning for MINERνA main detector (mainly neutrino cross-section experiments). Taking into account certain phenomena, one could rule out what processes may affect our calibrations and measurements. It is well-known that PMT works due to the photo-electric effect. Overall, it is thought that in normal conditions smooth variations in the surroundings (like temperature, pressure, moisture, etc) may not affect our measurements since the provider do not points out that this effects may lead to important variations in the gain (the amplification that occurs in the PMT). Here it will be shown how temperature effects may distort PMT gains in some degree. This analysis uses two thermometers and two datasets (April and May-July). In the Gain vs Temperature plots, one can realize that the small but still not negligible effects of the temperature affect the PMT gains. It was found some evidence in previous works [Chris Marshal, MINERνA] and [Chinese Physics C Vol. 41, No. 1 (2017) 016001, DAMPE] that the temperature changes affect PMT gains. This tells that the temperature effect should not be ignored and this temperature-gain relationship should be implemented in terms of calibrations constants in expressions such as equation C.9 and equation C.12. Before start, I am going to break down the content of this work as follows:

- **Chapter** 1: Here, the main concepts involved in scintillator materials and Photo-multipliers are shown.
- **Chapter** 2: In this Chapter, the basic ideas about the software used in this thesis (ROOT and Gaudi Framework) and also the basic way how one can use this computational tools in data analysis are presented.
- **Chapter** 3: In Chapter 3, the Experimental setup of the detector as the electronics used to collect, read and treat the data are shown.
- **Chapter** 4:In this last Chapter, the results obtained in this thesis project are shown as well as the data involved and how the data and statistics that are expressed in the plots (plots that show the behavior of the PMT gains as a function of the temperature they are exposed). Additionally, as a member of the MINERνA Collaboration, it was possible to participate in two papers, please see [26], [27] for more details.
  - E. Chavarria, J. Solano et al. *Measurement of total and differential cross sections of neutrino and antineutrino coherent $\pi^{\pm}$ production on carbon.*
    PHYSICAL REVIEW D 97, 032014 (2018)
  - E. Chavarria, J. Solano et al. *Measurement of the muon antineutrino double-differential cross section for quasielastic-like scattering on hydrocarbon at $E_{\nu} \sim 3.5GeV$.*
    PHYSICAL REVIEW D 97, 052002 (2018)

Objectives

- To prove that temperature variations affect the PMT gain measurements (photo-electron amplified signal). This effect is not anticipated by the manufacturer.
- To obtain the best fitting-curves for PMT gains vs temperature plots under the chi^2 criterion.
- To show that different thermometers are correlated to PMT gain measurements differently because temperature measurements are highly bias by statistical errors and the environment.
- To report that different thermometers show the same average statistical behavior (drop in PMT gain) when large quantities of data are taken.

Contents

List of Figures

List of Tables

List of Abbreviations

HEP	**H**igh **E**nergy **P**hysics
PMT	**P**hoto **M**ultiplier **T**ube
PM	**P**hoto **M**ultiplier
LI	**L**ight **I**njection
PE	**P**hoto **E**lectrons
MINERνA	**M**ain **IN**jector **E**xperiment **for** ν**-A**
LHCb	**L**arge **H**adron **C**ollider **b**eauty
TB	**T**est **B**eam
FTBF	**F**ermilab **T**est **B**eam **F**acility
FERMILAB	**F**ermi **N**ational **A**ccelerator **L**aboratory
MC	**M**onte **C**arlo
DUNE	**D**eep **U**nderground **N**eutrino **E**xperiment
ToF	**T**ime **o**f **F**light
RMS	**R**oot **M**ean **S**quare
ECAL	**E**lectromagnetic **CAL**orimeter
HCAL	**H**adronic **CAL**orimeter
NUMI	**N**eutrinos at the **M**ain **I**njector
WLS	**W**ave **L**ength **S**hifting
TE	**T**racker **ECAL**
EH	**ECAL HCAL**
FEB	**F**ront **E**nd **B**oard
DAQ	**D**ata **AQ**quisition
HV	**H**igh **V**oltage
CL	**C**onfidence **L**evel
ADC	**A**nalogic **D**igital **C**onversion
VME	**V**ersa **M**odule **E**uro card
CROC	**C**hain **R**eadout **C**ontroller
CRIM	**C**Roc **I**nterface **M**odule
MINOS	**M**ain **I**njector **N**eutrino **O**scillaton **S**earch
PCI	**P**eriperial **C**omponent **I**nterconnect
CMT	**C**onfiguration **M**anagement **T**ool
XML	e**X**tensible **M**arkup **L**anguage

GENIE	**G**enerates **E**vents for **N**eutrino **I**nteraction **E**xperiments
2p2h	**2**particles **2**holes
CCQE	**C**urrent **C**harged **Q**uasi **E**lastic
QCD	**Q**uantum **C**hromo **D**ynamics
RFG	**R**elativistic **F**ermi **G**as
LFG	**L**ocal **F**ermi **G**as
RPA	**R**andom **P**hase **A**pproximation
DIS	**D**eep **I**nelastic **S**cattering

Chapter 1

Theoretical Background

1.1 Scintillation Detectors

Particle Detectors that work due to scintillation principles are one of the most often and broadly used particle detection devices in nuclear and particle physics these days. It takes advantage of the fact that certain materials when hit by a charged particle, emit a small flash of light, i.e. a scintillation. When attached to a device that amplifies the incoming signal such as a PMT, this scintillation light can be transformed into electrical pulses which can be then analyzed and counted electronically to give information about the nature of the incident radiation [1].

1.1.1 General Characteristics

The basic components of a scintillator detector are described below in Fig. 1.1. A typical detector consists of a scintillating material which is optically coupled to a PTM either directly or via a light guide. As radiation hits the scintillator (charged particles), it excites the atoms and molecules making possible light to be emitted.

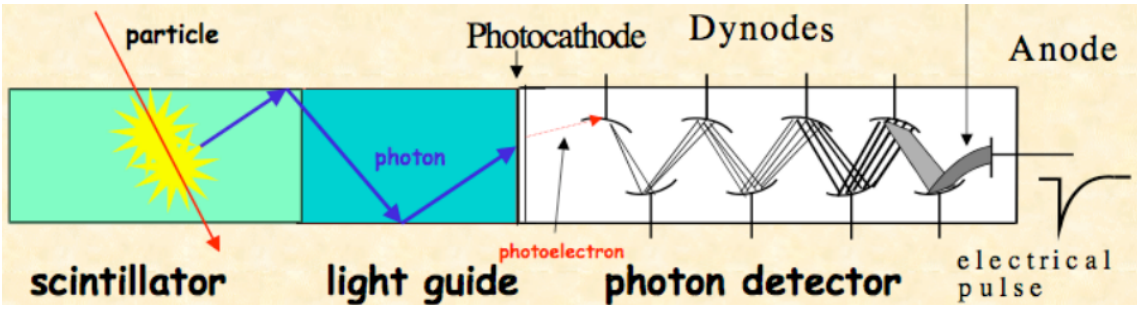

FIGURE 1.1: Schematic diagram of a scintillator counter (Photon detector) [16]

This light is carried through wire fibers (light guide) to (PM or PMT) where is converted into a weak current of PE which is further amplified by an electron-multiplier system (dynode chain) [1].

1.1.2 Organic Scintillators

These variety of scintillators consists of aromatic-hydrocarbon chains that form arrangements of linking benzene-ring molecules. One of their most noticeable attributes is a quit fast decay time roughly speaking on the order of some nanoseconds [1].

Plastics

In particle physics and fields related, plastic scintillators are probably the most broadly used. The plastics of most common use are: polyvinyltoluene, polyphenylbenzene and polystyrene. The light emission spectra of some commercial plastics is shown in Fig. 1.2 and fig. 1.3

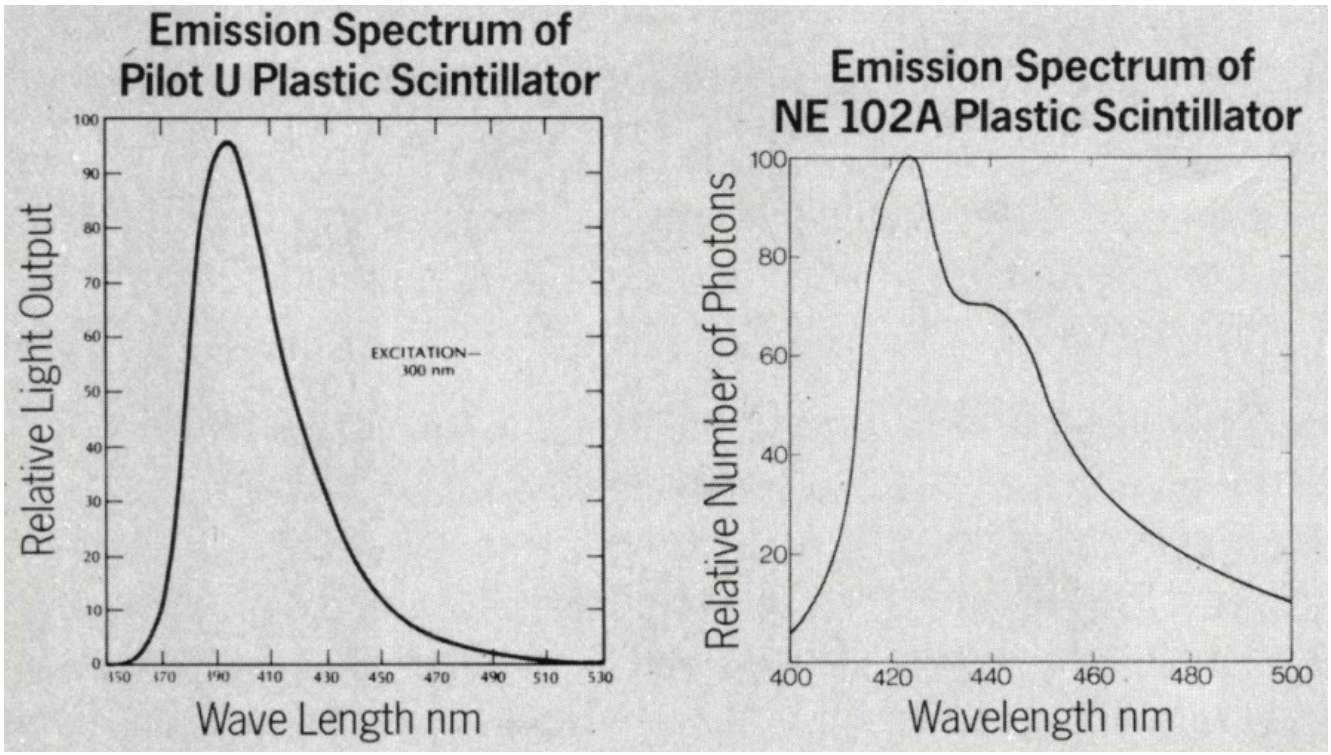

FIGURE 1.2: Light emission spectra for Pilot U and NE 102A plastic scintillators (polyvinyltoluene based scintillators) [52]

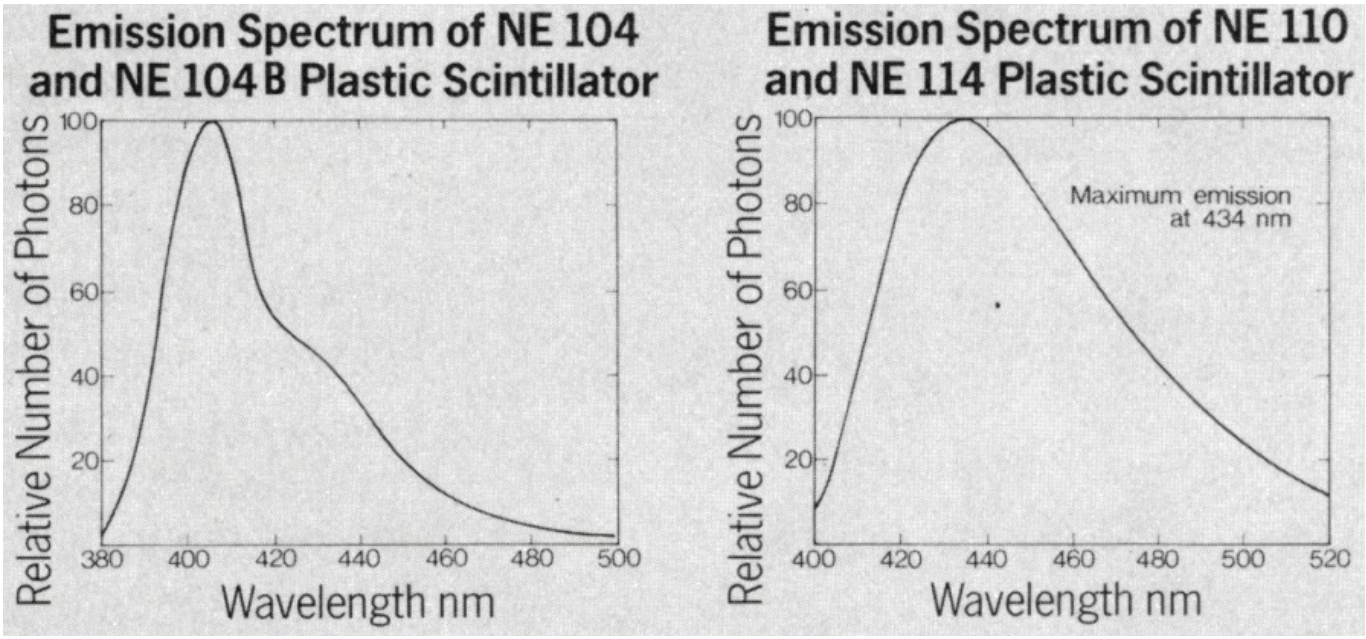

FIGURE 1.3: Light emission spectra for NE 104, NE 104B, NE 110 and NE 114 plastic scintillators (polyvinyltoluene based scintillators) [52]

Plastics show a considerably fast signal with a decay constant of about 2-3 ns and a high light output. The decay constant is the time that takes one photon in average, in being emitted. Because of this fast decay, the finite rise time cannot be ignored in the description of the light pulse as was done in 1.1. The best mathematical description, as shown by *Bengston and Moszynski* [1],appears to be the convolution of a Gaussian with exponential,

$$N(t) = N_0 f(\sigma, t) exp(\frac{-t}{\tau}) \tag{1.1}$$

Where $f(\sigma, t)$ is a Gaussian with a standard deviation σ. Table gives some fitted values of these parameters for a few common plastics. Where N_0 is the total number of photons emitted, τ refers to the decay constant that can have *fast* (τ_f) and *slow* (τ_s) components, although the fast component generally takes over [1].

TABLE 1.1: Gaussian and Exponential parameters for light pulse description for some plastic scintillators (*Bengston and Moszynski*).

Scintillator	$\sigma[ns]$	$\tau[ns]$
NE102A	0.7	2.4
NE111	0.2	1.7
Naton 136	0.5	1.87

1.1.3 Light Output Response

The response of a scintillator (light output) indicates its efficiency to convert incoming charged particles energy to photons. Generally the light output is different considering various kind of particles at the same

energy. Furthermore, for a given type of particle, it is not always the case that the light output is correlated with the energy linearly. Table 1.2 gives a short list of mean energy loss for some scintillators when electrons are the ionizing particles that excite the scintillator in order to generate light output [1].

TABLE 1.2: Average energy loss per scintillator photon for electrons.

Material	$\epsilon[eV/photon]$
Anthracene	60
NaI	25
Plastic	100
BGO	300

In general, this efficiency decreases for heavier particles. This behavior is seen in Fig. 1.4 for the case of plastic. A more complete list of scintillator light outputs is given in table 1.3

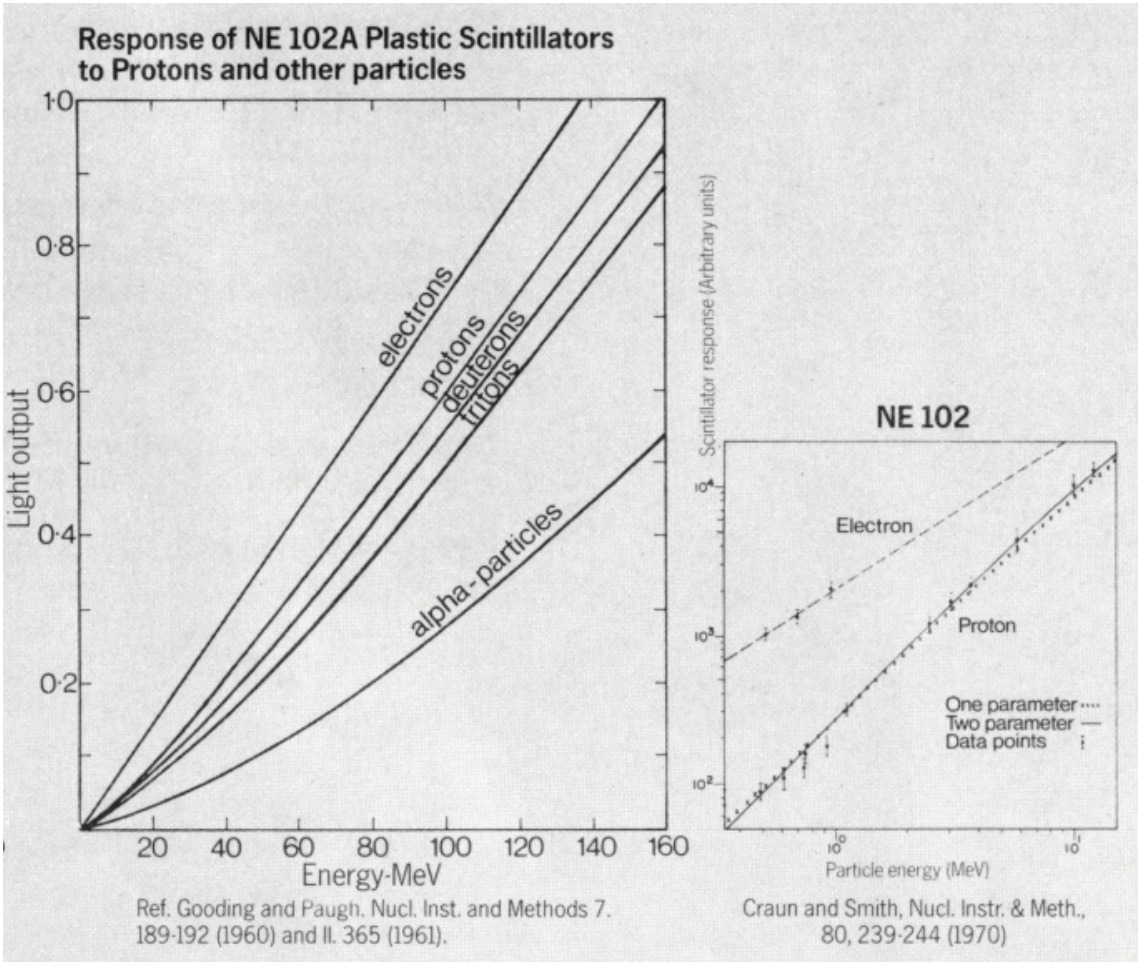

FIGURE 1.4: Response of NE 102 plastic scintillator to different particles [1]

Material	State	$\lambda_{max}[nm]$	$\tau_f[ns]$	$\rho[g/cm^3]$
NE 102A	plastic	423	2.4	1.032
NE 104	plastic	406	1.9	1.032
NE 104B	plastic	406	3.0	1.032
NE 105	plastic	423		1.037
NE 110	plastic	434	3.3	1.032
NE 111A	plastic	370	1.6	1.032
NE 114	plastic	434	4.0	1.032
NE 160	plastic	423	2.3	1.032
Pilot U	plastic	391	1.36	1.032
Pilot 425	plastic	425		1.19

TABLE 1.3: Physical properties of common plastic scintillators [52]

1.1.4 Linearity

it has been assumed as a first approximation that the response of most scintillators to incoming radiation energy L was directly proportinal to the energy, E, deposited by the incoming ionizing particle along it passes through the scintillator material,

$$L \propto E \tag{1.2}$$

The equation 1.2 [1] is thought a fair approximation for many applications in the nuclear and high energy field. In the laboratory one notices that the response of scintillators is a complicated function of energy and the ionizing particle and its specific ionization. The first model to successfully predict this behavior was due to the work of *Birk* in 1951. In his model, the light output per unit of length, dL/dx, is linked to the specific ionization by [2]

$$\frac{dL}{dx} = \frac{A\frac{dE}{dx}}{1 + kB\frac{dE}{dx}} \tag{1.3}$$

Where A: absolute scintillation efficiency; kB: parameter relating the density of ionization centers to dE/dx. In practice, kB is obtained by fitting Birk's formula to experimental data. Some values of kB for different particles in NE102A plastic are given in table 1.4. A higher order formula can be expressed as [1]:

$$\frac{dL}{dx} = \frac{A\frac{dE}{dx}}{1 + B\frac{dE}{dx} + C(\frac{dE}{dx})^2} \tag{1.4}$$

[1] The equations 1.2, 1.3 and 1.4 were taken from [W. Leo [1]]

[2] The specific ionization is defined as the average number of ion pairs created by the passing particle per unit of length. If ϵ is the mean energy loss for each ion pair created, then the specific ionization id $(dE/dx)/\epsilon$.

TABLE 1.4: Measured values of kB for NE102A plastic scintillator [1].

Particle	**Energy**	**dE/dx**	**kB**
	[MeV/nucl.]	[MeV/gcm^2]	[mg/(cm$^2 MeV$)]
Compton electrons and recoil protons	<4	>97	9.1±0.6
Compton electrons and alpha particles	<1.3	>272	9.8±0.8
Compton electrons and protons	1.2-1.4	>34	10±1
Recoil protons	<2.3	>150	10
Recoil protons	<8.4	>50	2
			3±1
Protons	<100	>7	3.7-7.5
Protons	28-148	5.5-20	13.2±2.5
Deuterons	23-60	10-23	
Neutrogen ions	3-9.5	(1-2)x10^3	<10
Protons to oxigen ions	Rigidly	2.0-120	10
	1.5-1.6GV		
Oxigen-iron nuclei	Rigidly	120-1300	10
	1.5-1.6GV		C = -5x10^{-6}
Protons	36-220	4.2-12.3	12.6±2.0
Helio	38-220	17-49	7.2±1.0
Carbon nuclei	95	265	7.8
Oxygen nuclei	105	550	C = -7x10^{-6}

1.1.5 Temperature Dependence

The light output of most scintillators may also be related to temperature changes. This behavior is generally week a room temperature. In organic scintillators, the light output is practically independent within their regular temperature interval: $-60°C$ and $+20°C$ and only drops 95% of this value at $+60°C$. The other kind of scintillators, on the other hand, are known to be more sensitives as shown in fig. 1.5. Both CsI (Tl) and CsI (Na), for instance, exhibit considerably strong variations in the normal range of temperatures, while Nal seems to be less sensitive. BGO (Bismuth Germanate Scintillator) light output has also been reported to show a high temperature dependence. increasing by about $\%1$ per degree Celsius as the temperature is decreased. As the temperature drops, the decay time for BGO also augments however [1].

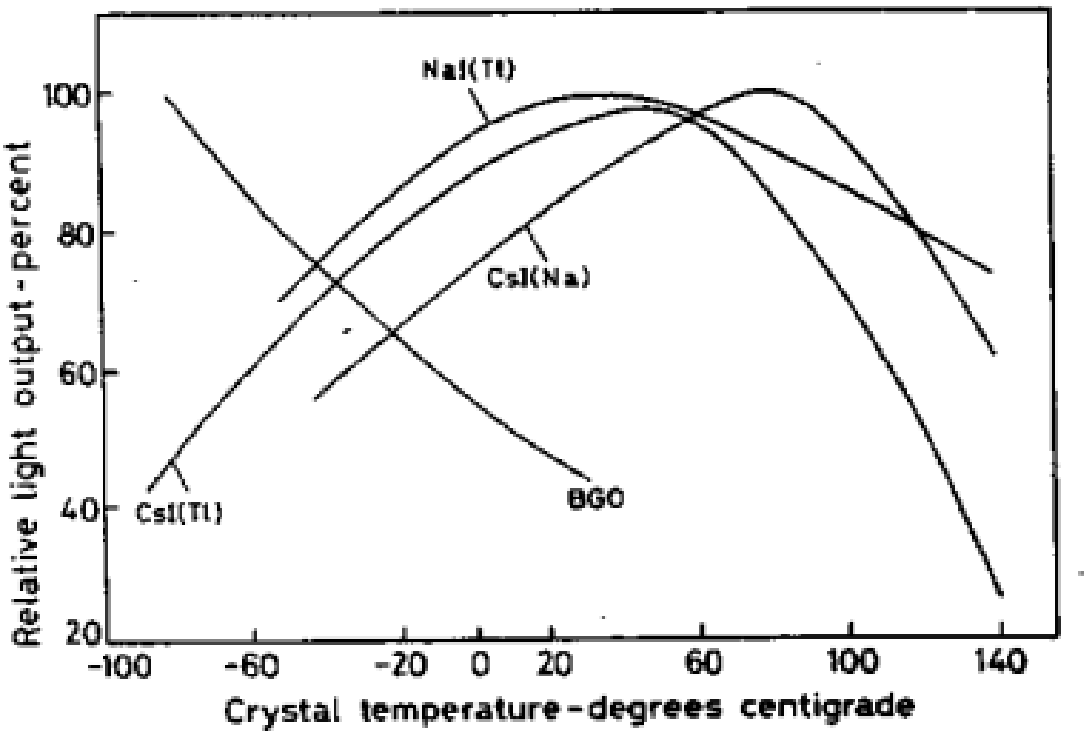

FIGURE 1.5: Temperature dependence of light output from inorganic crystals [1]

1.2 Photomultipliers

PMT are electron tube devices that take light and convert it into electronic signal (measurable electric current). They are known to be extremely sensitive and, in nuclear and high energy physics, are most of the time related to scintillator detectors, nonetheless their uses are quit varied. Fig. 1.7 sketches a diagram of a typical PM transversal cut. It consists of a cathode followed by an electron collection system, an electron multiplier section (or dynode chain as it is usually called) and finally an anode from which the signal can be taken to further analysis. All parts are usually shielded in an evacuated glass tube [1].

1.2.1 Photocathode

The photocathode converts incident light into photo-electron current by the photoelectric effect. To make easy the process of converting light into electric current, the photosensitive material is deposited right after a thin layer on the inside of the PMT window which is usually made of quartz or glass. From Einstein's well-known formula,

$$E = h\nu - \phi \tag{1.5}$$

That is what photo-electric effect states, however, the efficiency of any known cathode material known in the industry is far for being $\%100$ in the production of photo-electrons. Indeed, the photoelectric conversion efficiency varies strongly with the frequency of the incident light and the internal structure of the material. This overall spectral response is expressed by the *quantum efficiency* [1], $\eta(\lambda)$,

$$\eta(\lambda) = \frac{\text{number of PE relesed}}{\text{number of incident photons on cathode } (\lambda)} \tag{1.6}$$

Fig. 1.6 shows a plot of $\eta(\lambda)$ vs λ for some common materials used. When choosing a PM, a primary consideration should be its sensitivity to the incident wavelength.

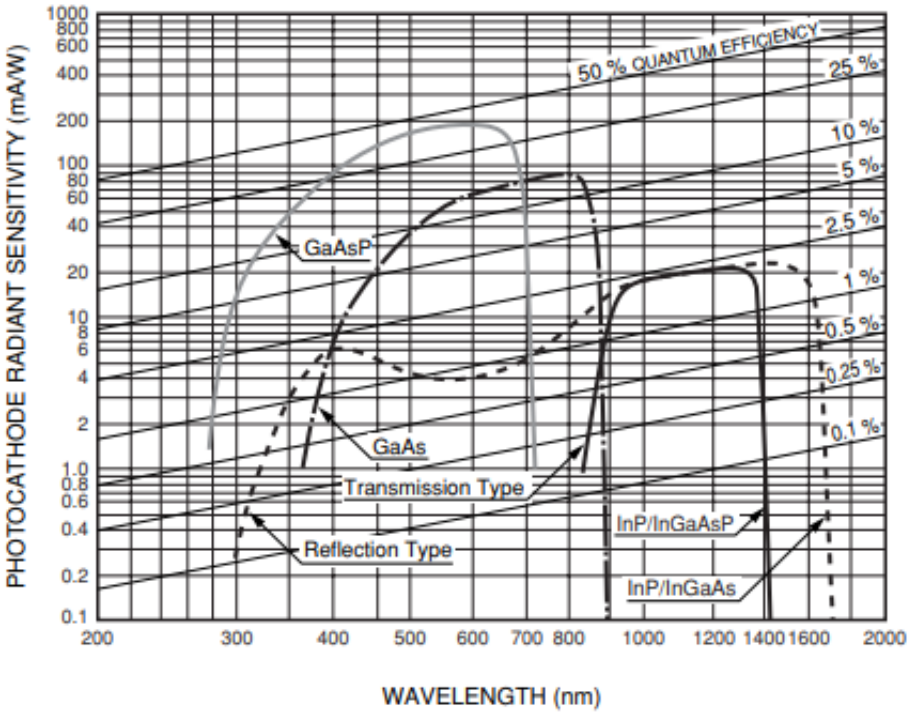

FIGURE 1.6: Quantum efficiency of various photo-cathode materials. It can be noticed that most compounds exhibit a quantum efficiency below $\%50$ [2].

1.2.2 Basic Principles of PMT Tubes

A PMT tube is a tube sealed in vacuum that typically consists of an input window, a photo-cathode, focusing electrodes, an electron multiplier section and an anode. The figure below shows the typical internal arrangement of a PMT.

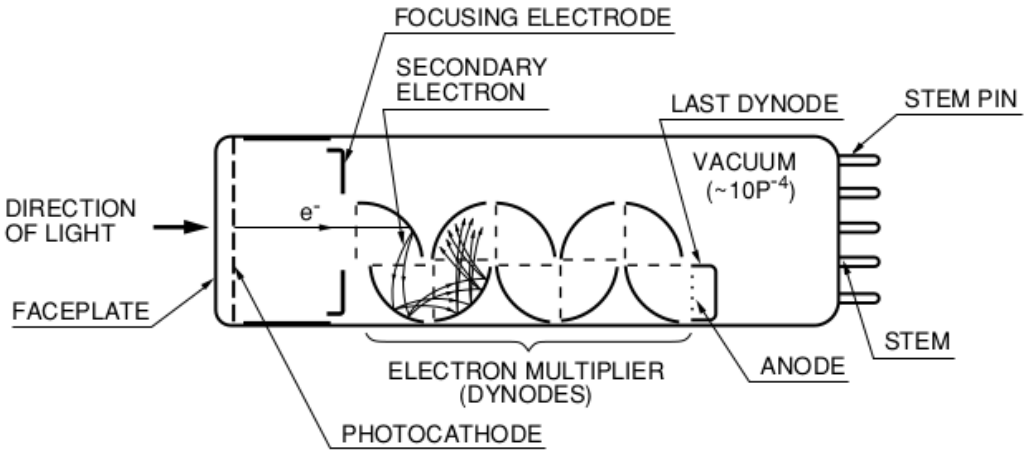

FIGURE 1.7: Internal view of a PMT [2].

Light that make its way to a PMT is detected and generates an output signal (photo-electrons), going through the following cycle [2]:

- Photons enter by the input window though a light guide or directly.
- Photons excite electrons in the photo-cathode, so that photo-electrons are forced to be ejected into the vacuum.
- Photo-electrons generated by the previous step, now are steered by the cathode into the beginning of the dynode chain where they are successively being amplified and accelerated due to the secondary emission. This secondary emission continues in each of the individual dynodes until the very end of the dynode chain.
- Most of the photo-electrons collected in the last dynode are directed into the the anode.

1.2.3 Photo-electron Emission

Photoelectric conversion is usually classified into two categories : internal photoelectric conversion and external photoelectric conversion. The first one is a process in which electrons are excited into the conduction band of the material. The last one happens when the photo-electrons are emitted into the vacuum from the material surface. Due to a photo-cathode is a semiconductor, the photo-electric conversion can be depicted using band models:

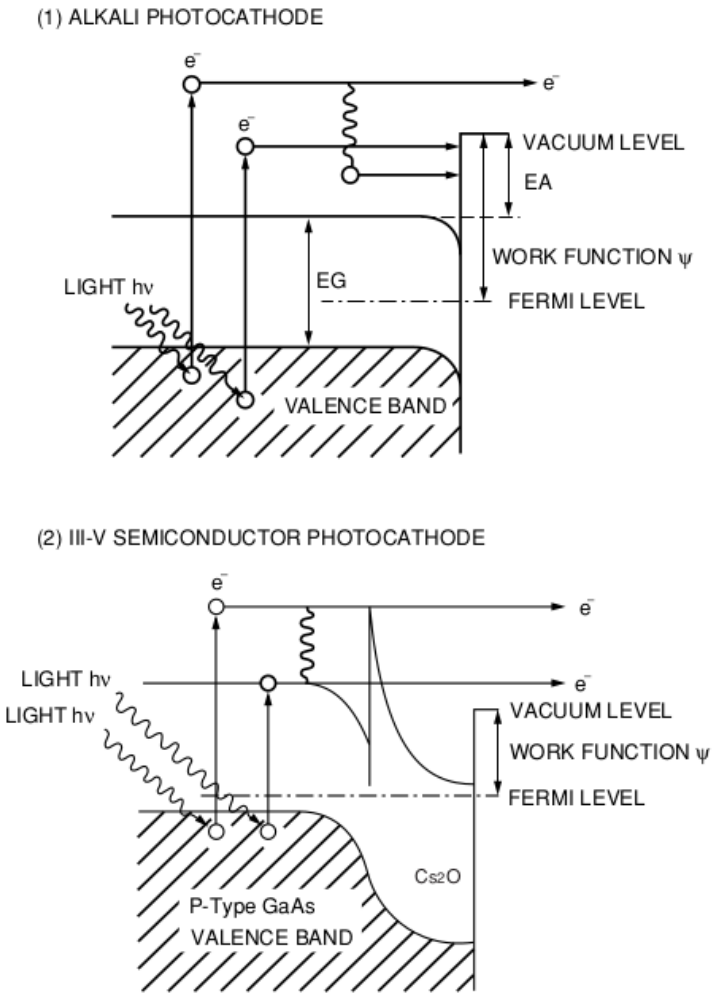

FIGURE 1.8: Photo-cathode band models [2].

Band model taken from Solid State Physics, states that, there exist a forbidden gap or energy gap (EG), where electrons are not allowed to stay, electron affinity (EA) which is an interval between the conduction band and the vacuum level barrier. See fig. 1.8, the work function (ψ) which is the energy difference between the Fermi level and the vacuum level. When light hits an photo-cathode, electrons in the valence band absorb photon energy (hν) and get excited, abandoning the photo-cathode surface. If the ejected electrons have enough energy to get over the vacuum level barrier, they are emitted into the vacuum as photo-electrons. This can be written in terms of probability and the quantum efficiency $\eta(\nu)$, so that the ratio of outgoing photo-electrons and incoming light is given by :

$$\eta(\nu) = (1 - R).\frac{P_\nu}{k}.\frac{1}{1 + 1/kL}.P_s \tag{1.7}$$

Where:

- R: reflection coefficient.

- k: full absorption coefficient of photons.
- P_ν: probability that photon absorption may excite electrons to a level greater than the vacuum level.
- L: mean escape length of excited electrons.
- P_s: probability that electrons reaching the photo-cathode surface may be released into the vacuum.
- ν: light frequency

In the equation 1.7, if we pick the adequate material that controls the appropriate values of R,k and P_ν, the parameters that govern the quantum efficiency equation will be L and P_s, values that can be handled accordingly. L becomes larger by the election of a better crystal and P_s is deeply related on electron affinity (EA) of the compound [2].

1.2.4 Electron Trajectory

The task of getting photo-electrons and secondary electrons in an efficient way on a dynode, is highly recommendable to reduce and optimize the electron transit time spread. Electrode design must be optimized by looking at the analysis of the electron trajectory. Electron velocity in a PMT tube is affected by the electric field which is mainly dominated by the electrode design, and also the voltage applied to the electrode. In order to estimate the electron trajectory in the PMT tube, numerical analysis can be used by providing the appropriate boundary conditions and repeating this process until the calculation error converges to a certain level. In the design of a PMT tube, the electron trajectory from the photo-cathode to the first dynode must be carefully designed taking into consideration the photo-cathode shape (planar or spherical window, see 1.9), the optimal alignment of the the focusing electrode and the supply voltage, so that the photo-electrons generated from the photo-cathode are focused onto the first dynode in the most efficient way as possible. The efficiency of collecting photo-electrons in the first dynode is the ratio of the number of electrons hitting the effective area of the first dynode to the number of released photo-electrons that will strike the second dynode shortly after. This efficiency ranges between 60 to 90%. The dynode chain is, in most cases, designed in more than ten stages of secondary-emissive electrodes (dynodes arranged successively) having a curved surface according the optimization studies planned beforehand. The arrangement of the dynodes must be designed in order to prevent ion or light feedback from the latter stages. Figures 1.9, 1.10 and 1.11 are cross sections of PMT tubes having a circular-cage, box-and-grid, and linear-focused dynode structures, respectively, showing their typical electron trajectories [2].

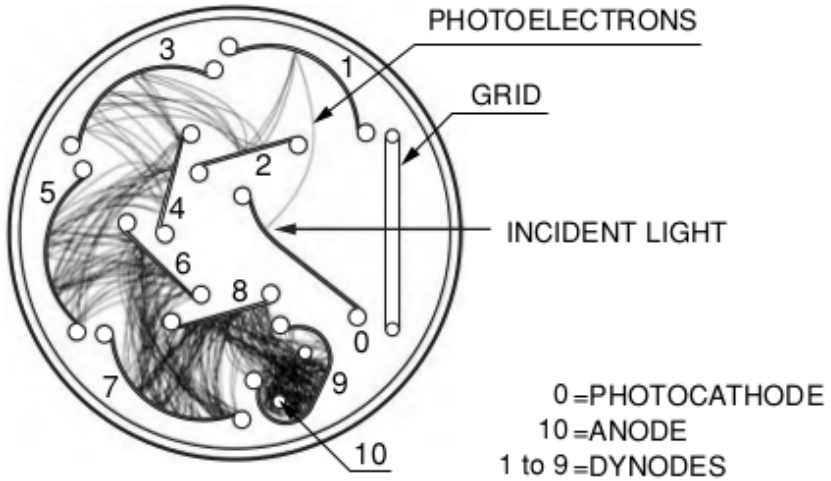

FIGURE 1.9: Circular-cage type dynode chain [2].

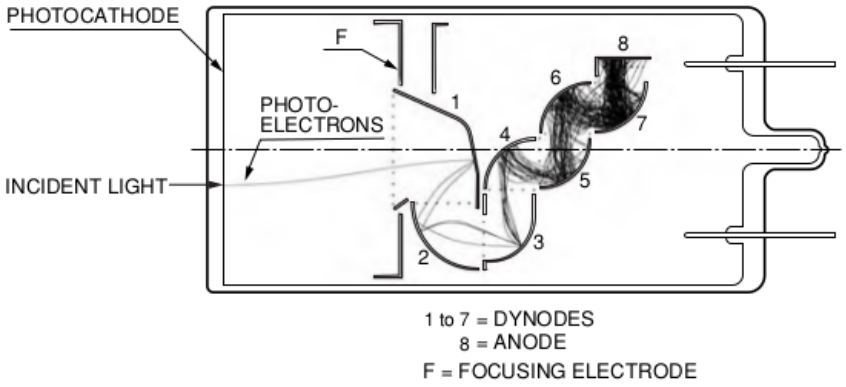

FIGURE 1.10: Box-and-grid type dynode chain [2].

1.2.5 Electron Amplifier (Dynode Chain)

As mentioned before, the electric field and internal cathode structure of a PMT tube is manufacture to provide high and efficient photo-electron convertion. Signal coming from the photo-cathode (photo-electrons) is amplified by the first dynode all the way to the last dynode (up to 19 dynodes), with current amplification on the order of 10 to as much as 108 times larger than the primary emission, and are finally directed to the anode. Most emissive compounds used for manufacturing dynodes are alkali antimonide, beryllium oxide (BeO), magnesium oxide (MgO), gallium phosphide (GaP) and gallium phosphide (GaAsP). These materials present a coating on the substrate electrode made of nickel, stainless steel, or copper-beryllium alloy. Figure 1.12 sketches a representation of the secondary emission multiplication of a typical dynode.

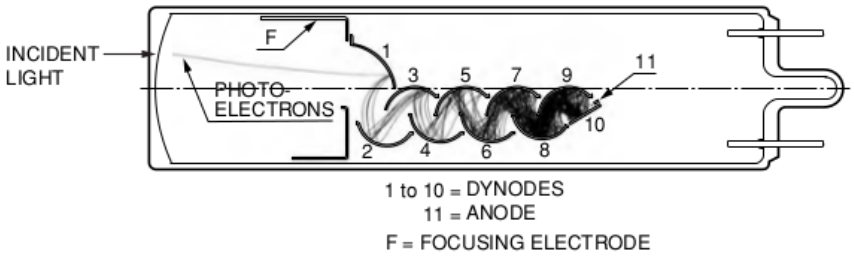

FIGURE 1.11: Linear-focused type dynode chain [2].

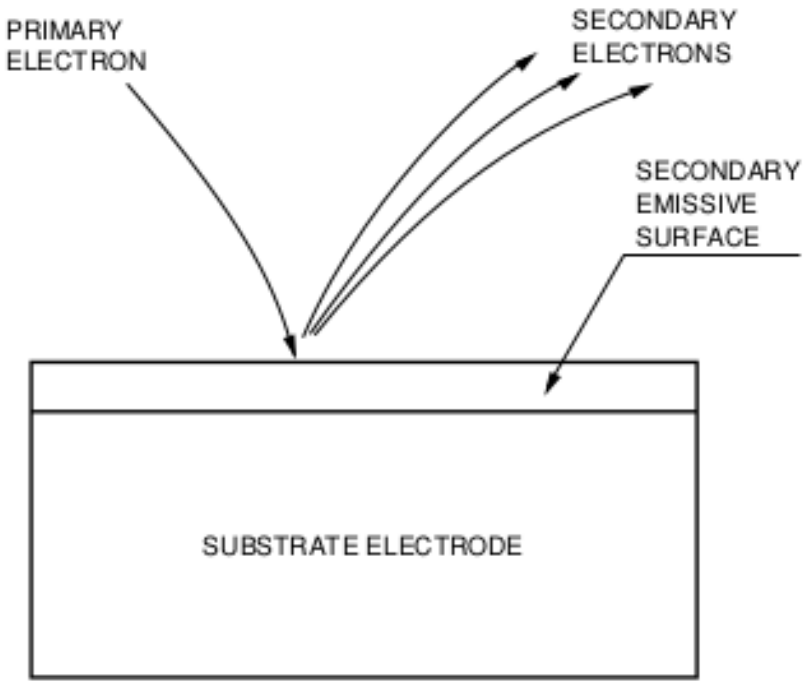

FIGURE 1.12: Secondary emission of dynode [2].

When a primary electron with initial energy E_p hits the surface of a dynode, δ secondary electrons are released. This quantity called δ, the number of secondary electrons per primary electron, is called the secondary emission ratio. Figure 1.13 shows the secondary emission ratio δ for various dynode compounds as a function of the voltage supply for the primary electrons. Ideally, the current amplification or gain of a PMT tube having the number of dynode stages n and the average secondary emission ratio δ per stage will be δ^n. Due to a large variety of dynode structures are available and their gain, time response and linearity differ depending on the number of dynode stages and other factors, the optimum dynode type must be selected according to the given application and results of previous simulations and optimization plan [2].

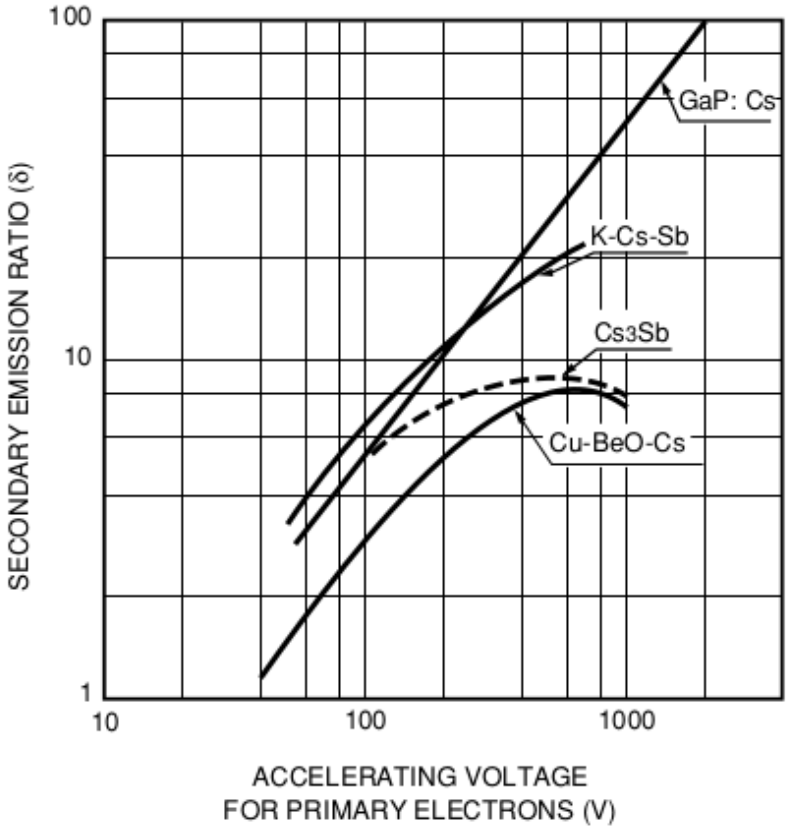

FIGURE 1.13: Secondary emission ratio [2].

1.2.6 Anode

The last stage of the amplification process, the PMT anode, is an electrode that stockpile secondary electrons amplified in a cascade-like process from a series of dynodes arranged is a such a way that the PMT anode collects and focuses the outgoing photo-electrons to external electronics. Generally, an anode is designed and shaped as a rod, plate or mesh electrode. One thing to have in mind while designing an anode is to set an appropriate potential difference between the last dynode and the anode in order to avoid charge effects in the surroundings and get a large and unwanted output current, that may damage the electronics related to the PMT. The PMT manufacturer clearly states in their data-sheet the typical currents that their PMT can hold [2].

1.3 PMT used in MINERνA TB experiment

MINERνA TB experiment uses the HAMMAMATSU PMT series to its experiments. More explicitly, in this work the Photomultiplier tube assembly H8804 was used. Fig 1.14 is what the PMT H8804 look like without scintillator and light fibers attached. Table 1.5 shows the description of the physical characteristics of the H8804.

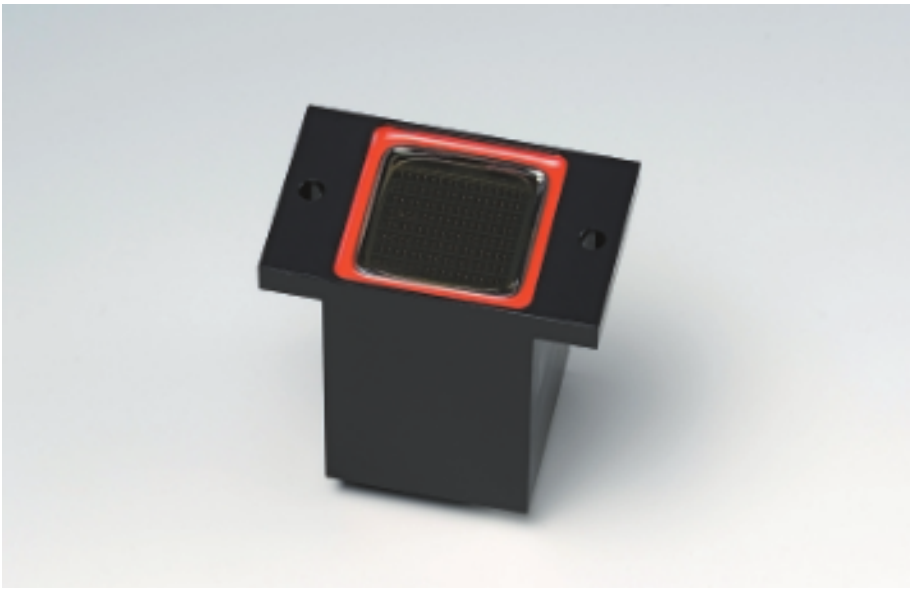

FIGURE 1.14: PMT tube assembly H8804 used in MINERνA TB experiment.

FEATURES:

- 8×8 Multianode, Anode Size: $2mm \times 2mm$ / Anode.
- Effective Area: $18.1mm \times 18.1mm$.
- High Speed Response.
- Low Cross-talk: $2\ \%$ Typical.
- With Mounting Flange.
- Application: High Energy Physics.

GENERAL

Parameter		Description / Value	Unit
Spectral Response		300 to 650	nm
Wavelength of Maximum Response		420	nm
Photocathode	Material	Bialkali	—
	Minimum Effective Area	18.1 × 18.1	mm
Window Material		Borosilicate glass	—
Dynode	Structure	Metal channel dynode	—
	Number of Stages	12	—
Weight		65	g
Operating Ambient Temperature		0 to +50	°C
Storage Temperature		-15 to +50	°C

MAXIMUM RATINGS (Absolute Maximum Values)

Parameter		Value	Unit
Supply Voltage	Between Anode and Cathode	-1000	V
Average Anode Output Current in Total		0.023	mA

CHARACTERISTICS (at 25 °C) with Standard Voltage Divider

Parameter		Min.	Typ.	Max.	Unit
Cathode Sensitivity	Luminous (2856 K)	60	80	—	µA/lm
	Blue Sensitivity Index (CS 5-58)	7.5	9.5	—	—
Anode Sensitivity	Luminous (2856 K)	10	50	—	A/lm
Gain		—	0.6×10^6	—	—
Anode Dark Current per Channel (after 30 min storage in darkness)		—	0.2	2	nA
Time Response	Anode Pulse Rise Time	—	1.0	—	ns
	Electron Transit Time	—	12.0	—	ns
	Transit Time Spread (T.T.S.)	—	0.38	—	ns
Pulse Linearity per Channel at ±5 % Deviation		—	0.6	—	mA
Uniformity Between Each Anode		—	1: 2	1: 3	—

TABLE 1.5: Taken from H8804 series datasheet. This table shows important physical properties of the H8804

Fig. 1.15 shows the typical spectral response of the H8804 under given light wavelengths. Fig. 1.16 indicates the gain (signal amplification) as a function of the voltage supply required to accelerate the photoelectrons coming from the cathode all the way through to the anode. Table 1.6 shows the standard voltage divider and the voltage supply for each electrode of the H8804 PMT. Fig. 1.17 show a schematic diagram that depicts the internal wiring of the last dynode (dynode number 12) with the 64 independent anodes (also called pixels).

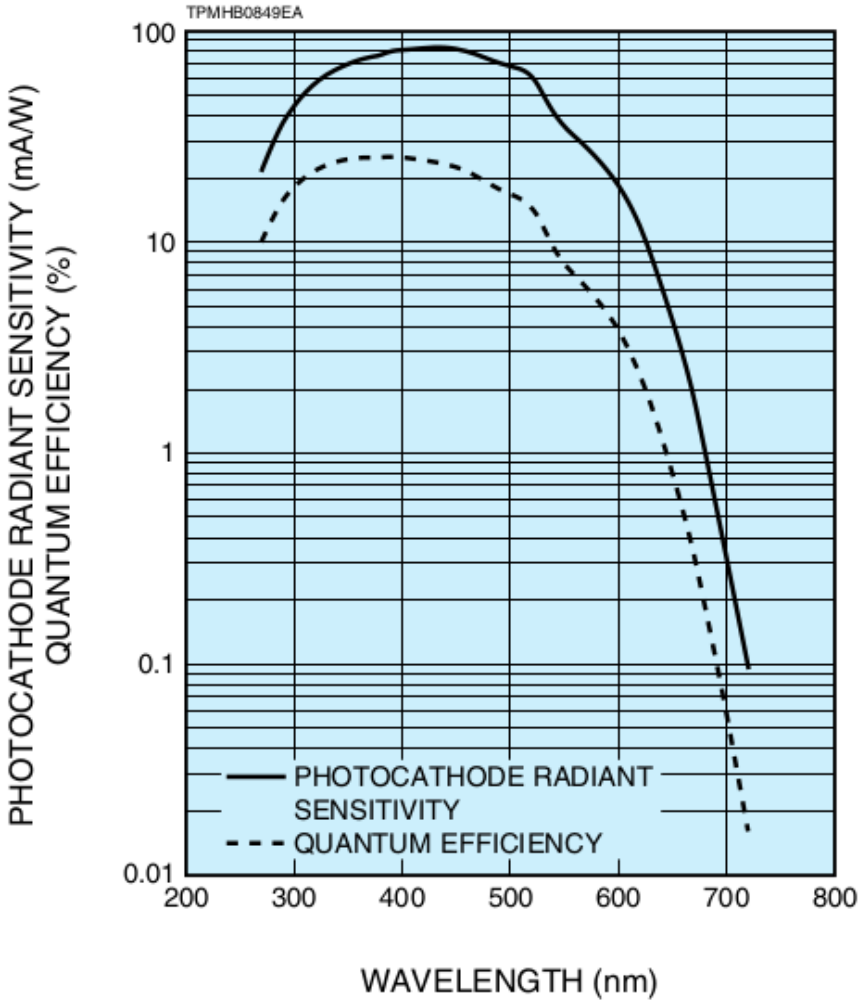

FIGURE 1.15: Taken from H8804 series datasheet. This plot shows the quantum efficiency of the H8804 for different light wavelengths.

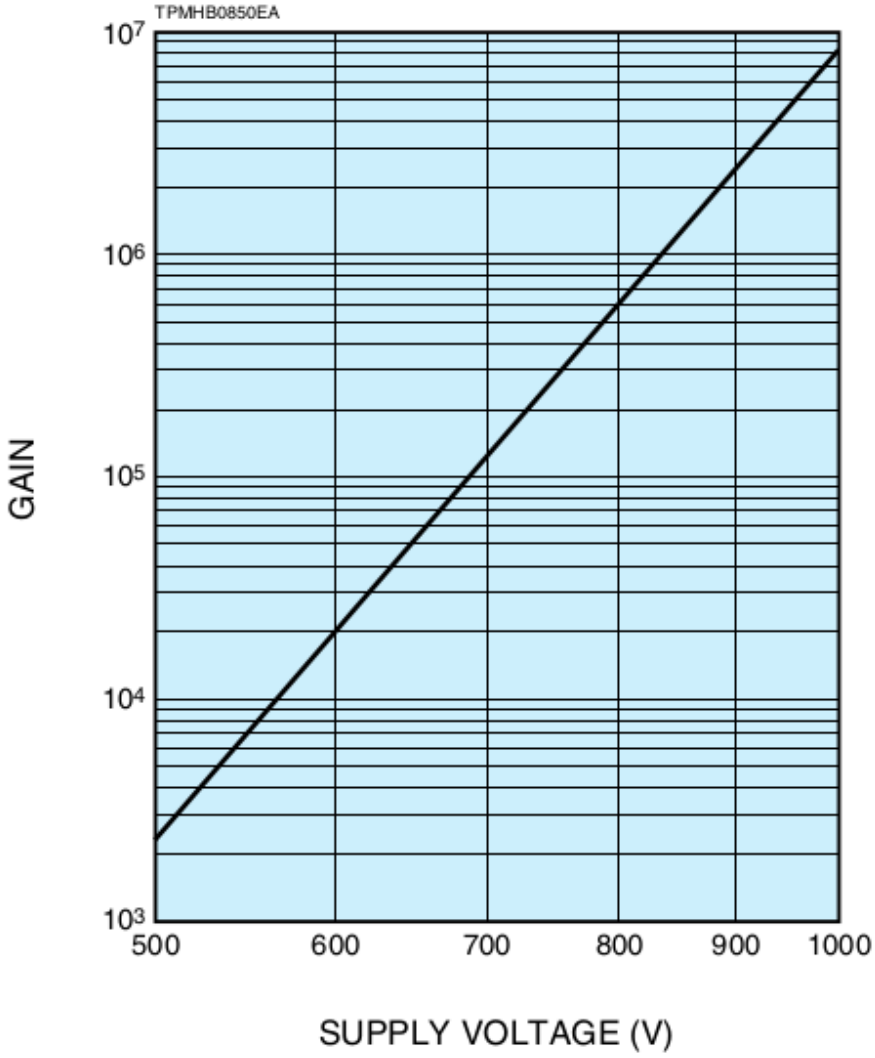

FIGURE 1.16: Taken from H8804 series datasheet. This plot on the other hand, shows the gain as a function of the voltage supply of the PMT.

Electrodes	K	Dy1	Dy2	Dy3	Dy4	Dy5	Dy6	Dy7	Dy8	Dy9	Dy10	Dy11	Dy12	P
Ratio	3	2	2	1	1	1	1	1	1	1	1	2	5	

TABLE 1.6: Taken from H8804 series datasheet. This table shows the standard voltage divider and supply voltage ratio of the H8804 PMT. Where: supply voltage: $-800V$, K: Cathode, Dy: Dynode, P: Anode

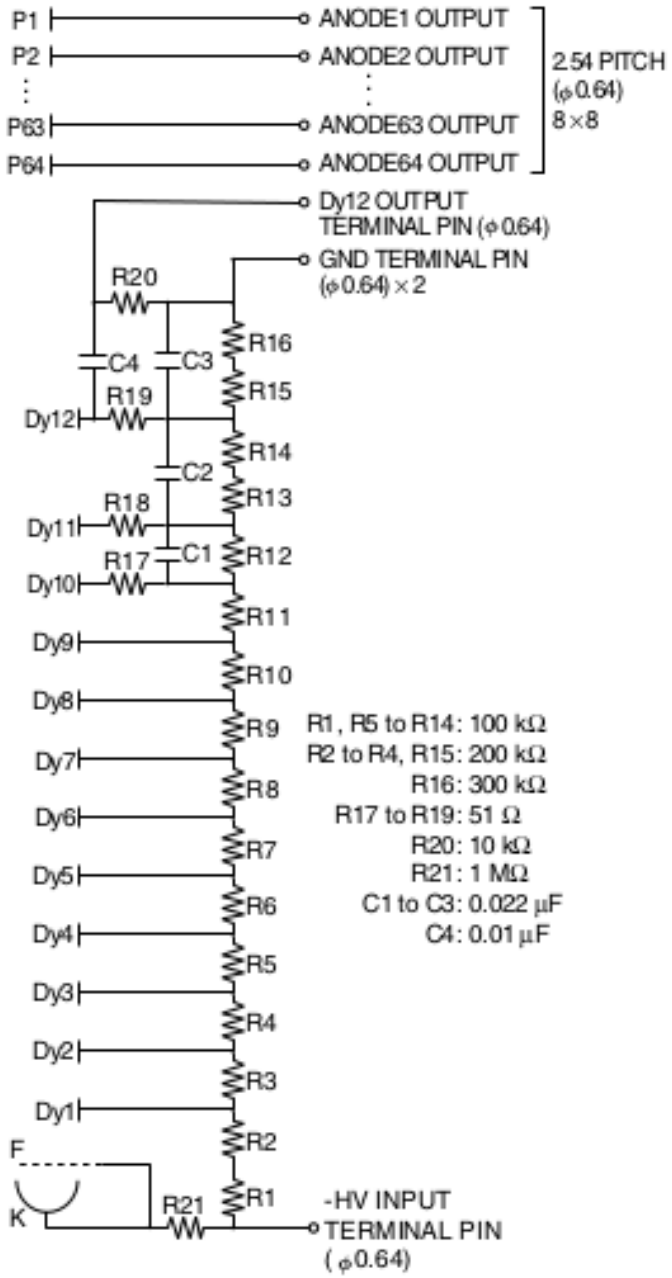

FIGURE 1.17: Taken from H8804 series datasheet. This table shows the internal wiring of the H8804 PMT. As you can see from the diagram there are 64 independent anodes which divide the signal coming from the last dynode.

Chapter 2

Analysis Tools

2.1 Gaudi Framework

It is often needed solid software that makes single pieces of code work together. Most of Particle Physics Processing Data need to perform a common task. For example:

- Loops over certain events.
- Detector geometry and Event Simulation.
- Converting raw data into human-readable numbers (digitalization).
- When particles interact with medium, they go through a lot of processes so they need to be reconstructed considering a given model managed by the physics libraries.
- The goal is to make an analysis in particular (results).

This set of HEP tools was originally proposed and developed by the LHCb experiment. The Gaudi Framework has been extensively used by many experiments worldwide, including MINERνA. It shows additional key features [3]:

- Event model and Detector Geometry is written in XML (extensible markup language) format.
- cpp code is automatically generated from XML file (a macro or a C/C++ code).
- Standard IO file is in POOL file format (a format used in reconstruction analysis).
- Use the CMT (Configuration Management Tool) command in order to upgrade/install new versions of libraries and shared dependencies.

2.2 CMT

When the user need to install/upgrade new analysis tools (often required for example when one needs to analyze higher or lower energy ranges), one of the simplest ways to do it is by calling the cmt command. It install/upgrade and link dependences between libraries/packages [3]. Fig. 2.1 show the basic structure of gaudi environment.

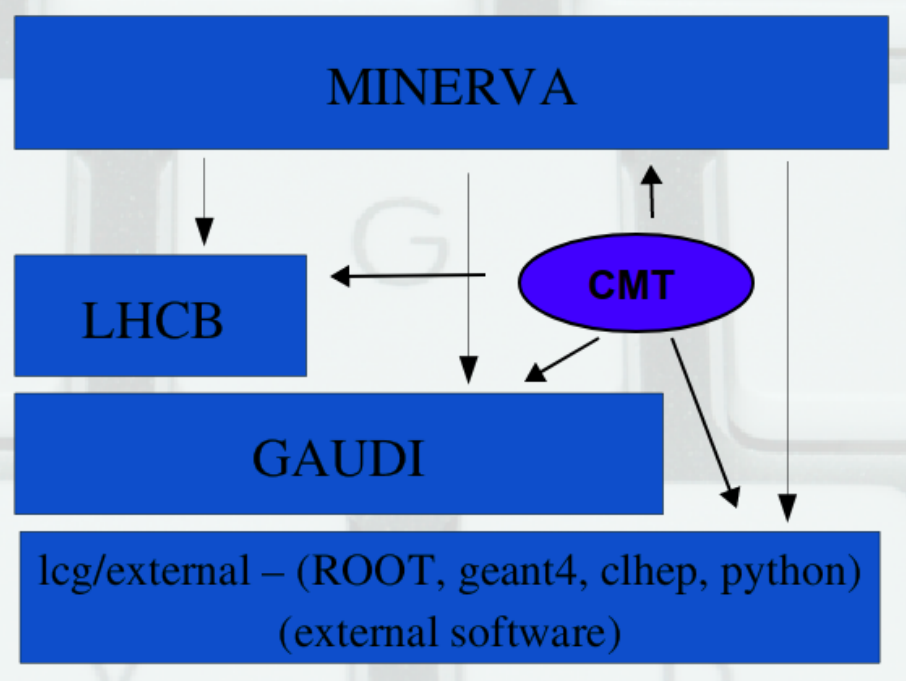

FIGURE 2.1: Organization of The Gaudi Framework in MINERνA. MINERνA uses LHCb libraries to process hadron data and third-party software as well (ROOT, Python, Geant, etc.) [3].

2.3 ROOT

ROOT is an Object-Oriented Data Analysis Framework that was originally coded and developed by physicists at CERN. Before ROOT, René Brun and Fons Rademakers created PAW that was a twenty-year-old FORTRAN libraries and by that time the early 90's they new that PAW was reaching its limits. Although still on demand, PAW tools could not scale up to the challenges offered by the Large Hadron Collider, where the data collected was large compared to anything seen before ROOT was developed on behalf of the NA49 experiment at CERN. NA49 has generated an humongous amount of data at that time, around 10 Terabytes per run. This rate provided the ideal environment to develop and test the next generation data analysis tools. One can not mention ROOT without mention CINT, its C++ interpreter. CINT was created by Masa Goto in Japan. It is an independent product, which ROOT is using for the command line and script processor [4]. Fig. 2.2 is the common tree-like structure of a root file.

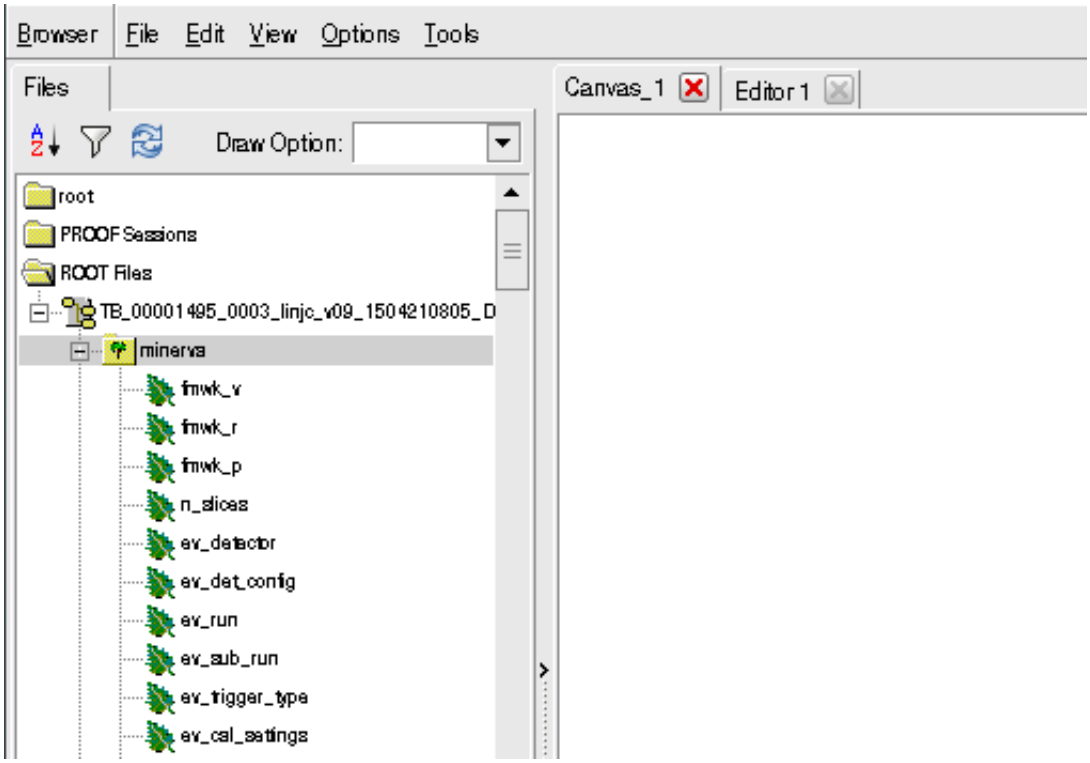

FIGURE 2.2: Typical structure of a root file. In root files the data is organized in a tree-like hierarchy where the branches represent certain variables and the leaves make reference to variables that are related.

ROOT has plenty of libraries and examples intended to High Energy Physics and Statistics in general.

2.3.1 TH1 Hitogram Class

This Class allows the user to take advantages of the ROOT libraries and functions to build customized histograms. Fig. 2.3 shows the different options of the TH1 class. One can draw a simple $1-D$ histogram (top left), a $2-D$ histogram (top right) and a plot with error bars (bottom).

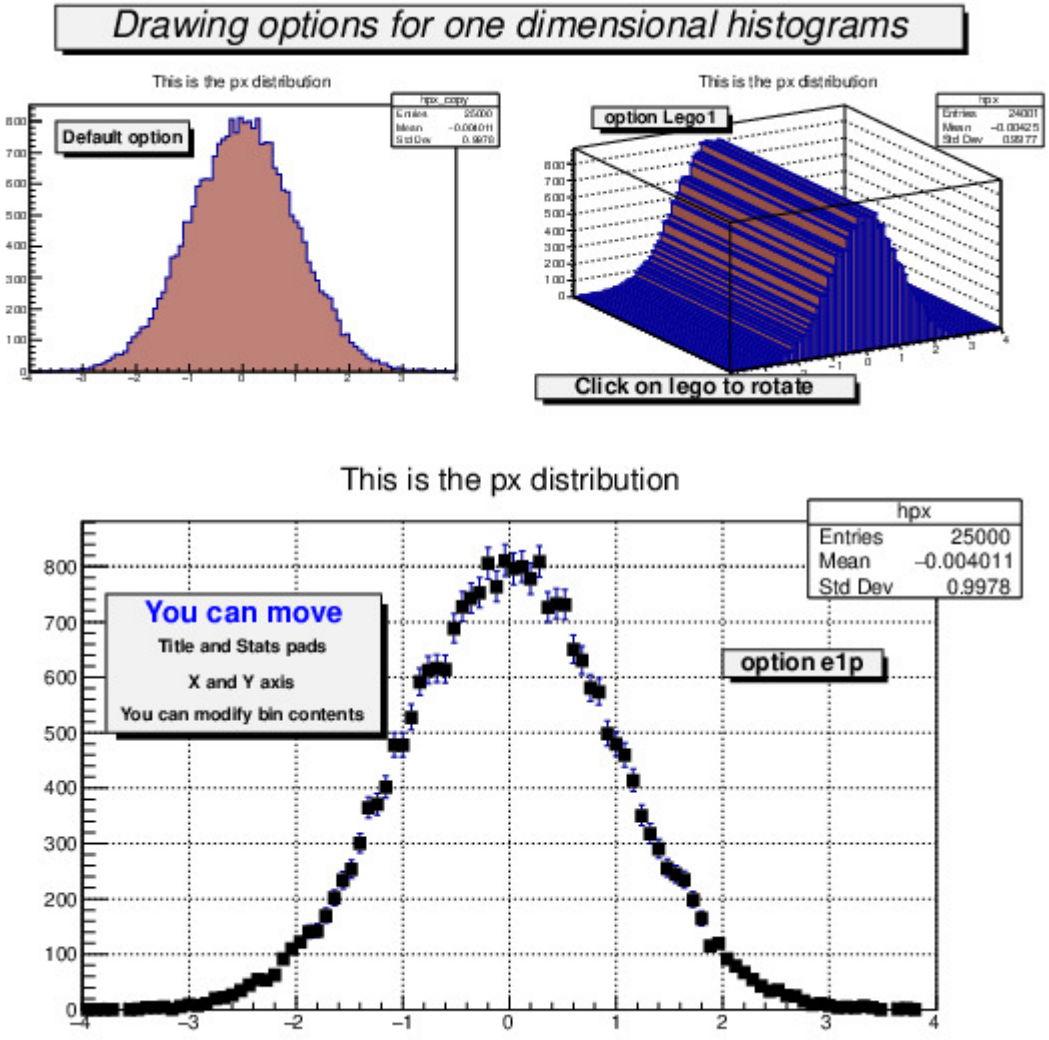

FIGURE 2.3: Built with ROOT v6.10 for more details please see [4].

2.3.2 TGraph Class

This Class makes possible to draw plots with features that let the user to visualize better the Physics and Analysis in the display. Fig. 2.4 shows a graph using log scale, this type of representation comes in handy when manipulating large numbers.

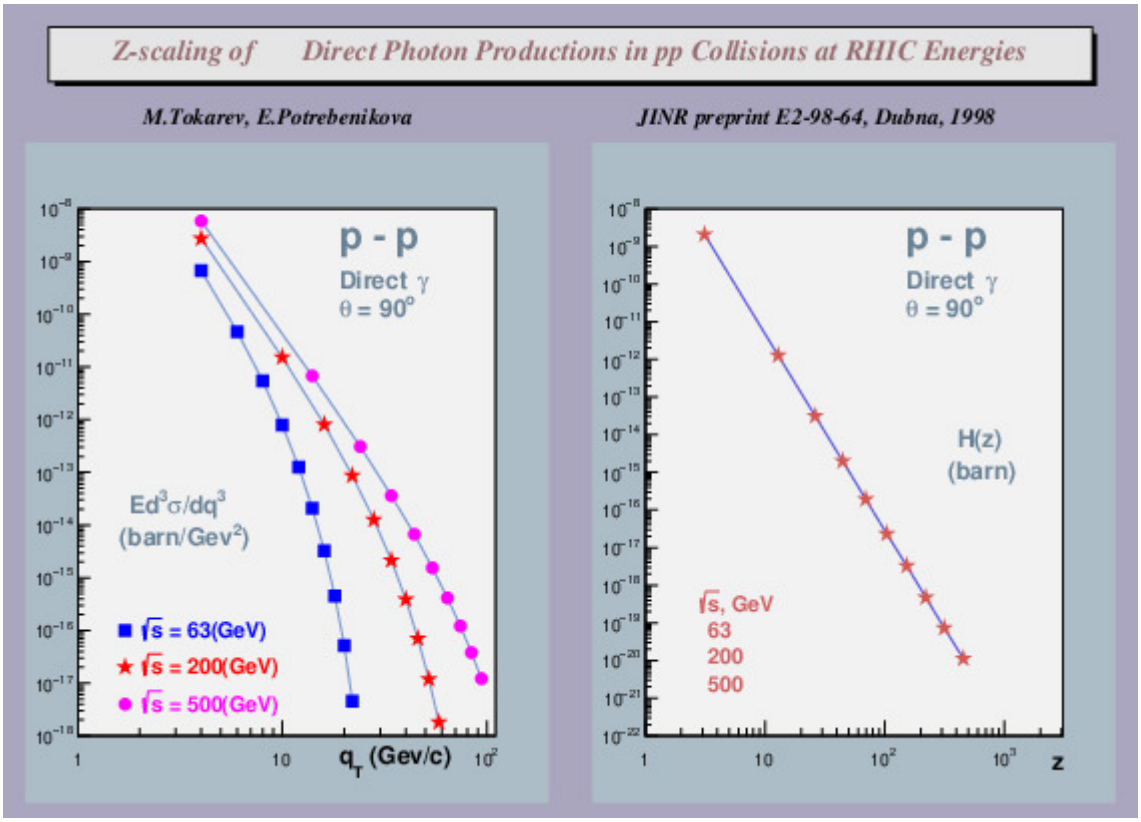

FIGURE 2.4: Built with ROOT v6.10 for more details please see [4].

2.3.3 PyROOT

PyROOT is a Python extension module that allows the user to interact with any ROOT classes from the Python interpreter. This is done generically using the ROOT dictionary, therefore there is no need to generate any Python wrapper code to include new ROOT classes. At the same time PyROOT offers the possibility to execute and evaluate any Python command or start a Python shell from the ROOT/CLING prompt [13]. For a practical tutorial see [17].

2.3.4 Minuit

Minuit is an graphic-conceived application intended to find the minimum (typically used in minimization problems) value of multi-parameter functions and analyze the behavior and shape of the function around the minimum. The main application is in statistical analysis, working on chis-square or log-likelihood functions, in order to compute the optimal fit-parameter values and uncertainties, also including possible correlations between parameters [5] . [The reader can find an application of Minuit in this Thesis Work by looking at fig.4.14 and fig. 4.15 where it is shown Confidence Plots for the best-fit parameters of the data.]

Chapter 3

Experimental Setup

3.1 Introduction and test beam goals

The MINERνA Collaboration is one of the many experiments that runs at FERMILAB which is located in Batavia, Il. The main building is called Wilson Hall named after the 20th century Physicist Robert R. Wilson [22] , where one can find the main offices and people around FERMILAB. One can find more information about FERMILAB at [20] and regarding the MINERνA experiment at [21].

The goal of the TB experiment is to evaluate how accurate the MC simulation of the detector response to hadrons exiting the nucleus. The accuracy of the single-particle response simulation is a high-priority task to perform neutrino cross-section experiments at MINERνA detector. The detector used to take data is a miniature replica of MINERνA [6].

3.2 MINERνA TB detector and calibration

The Test Beam detector is a small version of the MINERνA detector installed in the NuMI neutrino beam (hereafter called the MINERνA detector). The TB detector consist of 40 square planes of 63 nested, triangle-shaped scintillator strips each with length $107cm$ and thickness $1.7cm$. The TB detector runs mainly in two configurations. One configuration has 20 planes with $1.99mm$ thick lead absorber (ECAL) immediately after are placed 20 planes with $26.0mm$ thick iron absorber (HCAL). The absorber is placed between neighbor scintillators, starting the absorber upstream with respect of the scintillator planes. Both detectors MINERνA and TB detectors have the same three-view UXVX pattern of planes with U and V rotated clockwise or counterclockwise 60^o respect to the X plane that sets the vertical coordinate system (in the case of the TB detector) [6].

The other configuration is compose of 20 planes with no absorber (tracker) followed right after by 20 planes of ECAL. For sake of simplicity, these configurations will be labeled as EH and TE, respectively and it can be visualized in fig. 3.3. Additionally, a new TB configuration has been set: SuperHcal which which consists of tracker and double iron plates that HCAL configuration. They show side view of the X planes for a proton in the TE and a pion in the EH detector configurations. The readout chain from scintillator to WLS fiber to PMT [6] to digitization (convertion from binary data to human-readable numbers) [9] is practically the same between the TB and the MINERνA detectors. The main difference is that the TB detector does

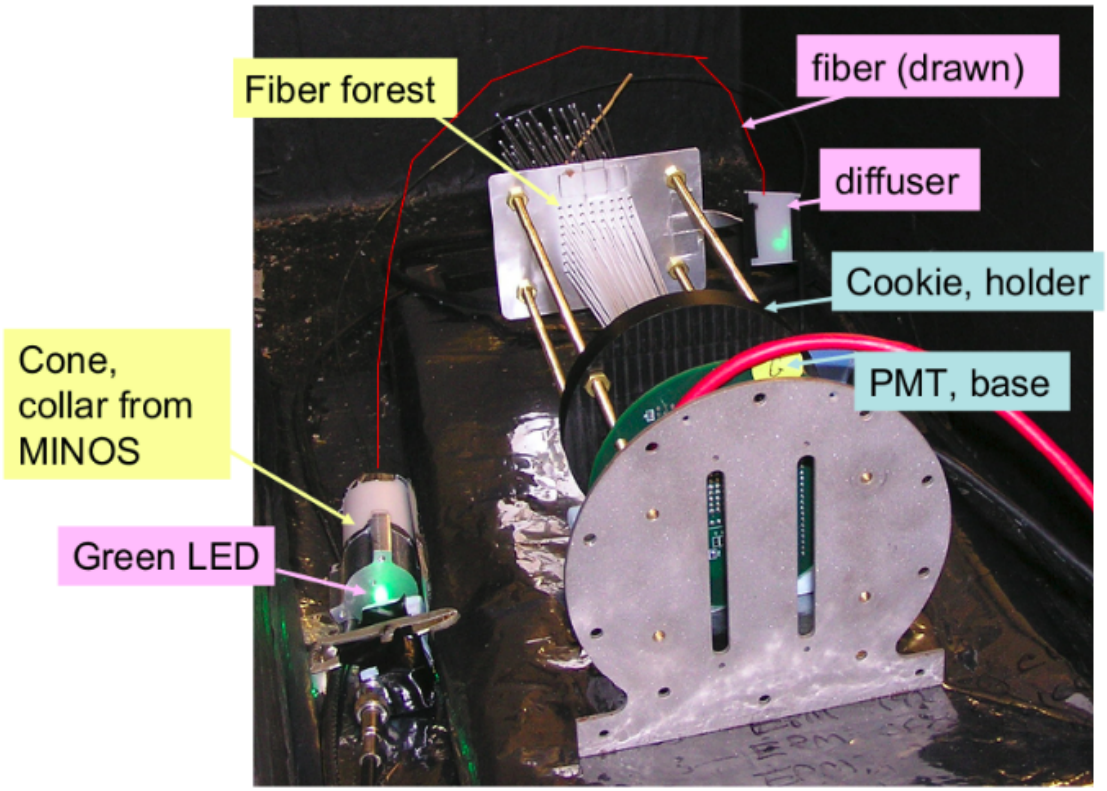

FIGURE 3.1: Setup of a typical PMT+fiber. From the botton the light source is shown (TB initially used green LED), next to the LED source is placed a collar just to avoid the fiber to mover around. On the right side a diffuser is used (a diffuser is employed to make sure that each pixel is irradiated with the same intensity, the diffuser is usually frosted glass. Fig. 3.2 shows how the fiber optics cables are attached to the PMT tube). The cockie is used to attach the Wire Light Fibers (WLS, these are used just in beam mode) to the Front End Board (FEB). The PMT base (metallic frame, is required to firmly attach the FEM to the PMT) [55].

not use clear fiber optical cables; the WLS fiber are attached right after to the PMT a half-meter distance out of the scintillator plane. The consequences of smaller scintillator planes and absence of clear fiber is that the TB detector can offer about 50% higher light yield for a given energy deposit, and better resolution for some types of processes compared to MINERνA detector side by side. TB and MINERνA detector utilize Hamamatsu H8804MOD-2 multi-anode PMT. The FEB and DAQ [9] save the same $16\mu s$ of data in response to the trigger, and are only tuned differently to work in response to a ray trigger scintillator rather than the expected arrival of a trigger from the NuMI beamline. The energy scale of the detector is calibrated using the same strategy described in [6] for the MINERνA detector. An initial approximation for PE yield is given for each strip using *pedestal* subtraction and a gain measurement based on the *light injection* system.

In both, Minerνa and TB experiments, we take and storage the data in short periods of time called "run". Moreover, We divide each run (see fig. 3.4) in "subruns". Each subrun has a distinctive name and corresponds to special modes of the beam and detector.

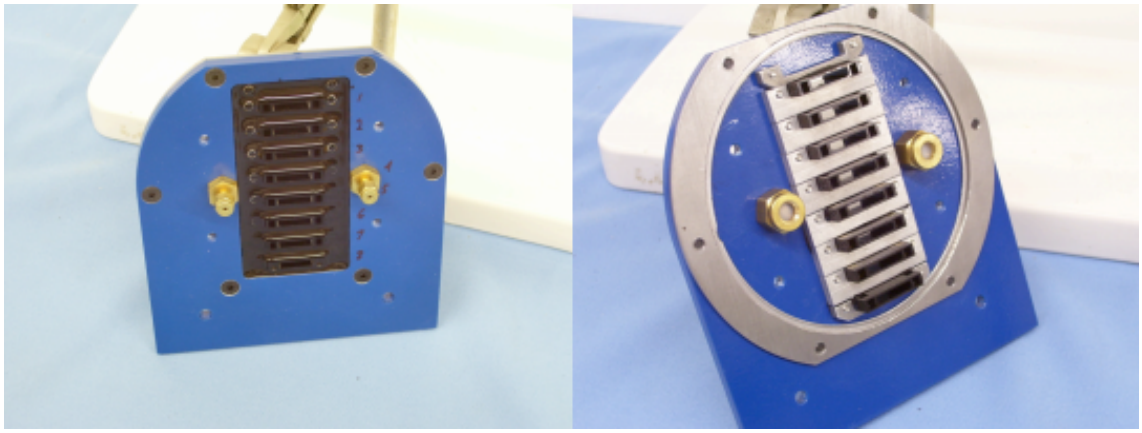

FIGURE 3.2: Two fiber optics cables are connected to each fiber-end faceplant (interior on the left, exterior on the right side) of the PMT tube, carrying light from the LED source. In the interior of each fiber-end faceplant there is a diffuser to spread out the light uniformly. [58].

Light Injection(LI) In LI mode we inject light directly to the PMT from blue ALGaInP LED that has a well-defined light spectra that peaks around $472nm$ with 0.5 Hz. The light goes along a WLS (Wave light shifter) fibers to each pixel of the PMT (64 pixels). The PMT just requires light of certain wavelength as input and gives a flow of electrons as output which can be mapped out into voltage signals through the electronics and this makes possible to record raw data and convert it in digital format. Fig. 3.1 shows the PMT tube setup. The current limit of this LED is around $20mA$, and the pulse width is around $30ns$ which can lead to a current of $200mA$.

Pedestal(Ped) It refers to regular monitoring of noise while the beam is off, this is as a reference point because the pedestal signal is required to be subtracted from regular beam mode. Each readout gate is opened during $16\mu s$. Pedestal mode captures noise from cosmic rays, radioactive sources, electronic noise and PMT dark current signal.

Beam In beam mode we smash our beam against our targets (iron, lead, etc) in order to make calorimetric and particle-interaction studies. We set the beam type (+pion, -pion) and the intensity accordingly. When a charged particle hits a scintillator plane, this one emits light of certain wavelength that is collected into the PMT. In this case each readout gate is opened $10\mu s$ (beam spill)

3.3 Light Injection Setup for TB detector

The strategy used for calibrating the TB detector consists of getting one pedestal run and three LI runs each day. Each pedestal runs is composed of two thousand gates (a gate is a time where the LI data is taken and recorded by the DAQ system). This mechanics is almost performed at the end of the shift (it is the jargon used to name the data-taking period) usually around 6.00 pm (Chicago CDT time) when the secondary beam was off [54]. Each PMT is attached to an FEB through WLS fibers. In the TB detector, FEBs are described uniquely by a given physical address. For example a typical FEB is tagged as: FEB [1][2][3], where the number from the left [1] indicates its croc at which is attached, the digit in the middle [2] refers

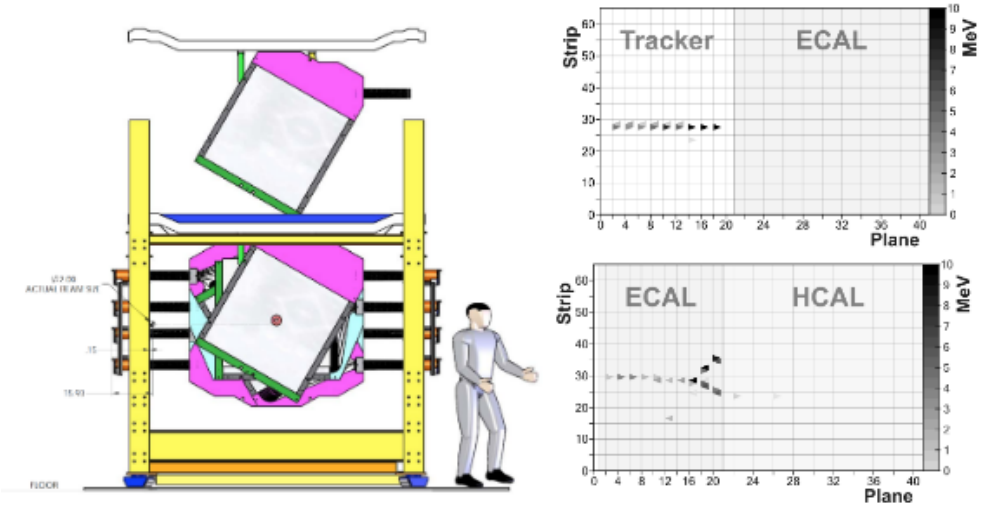

FIGURE 3.3: (left) A sketch of the TB detector from the front side. The third U plane is put down onto the stand behind eight installed planes. The drawing also illustrates the every other side readout in sets of four planes. If this was the ECAL, there would be a plane of lead absorber interleaving each plane. A proton (right top) being stopped at the end of its range in plane 18 of the TE configuration and a pion (right bottom) decaying near plane 16 of the EH configuration [6].

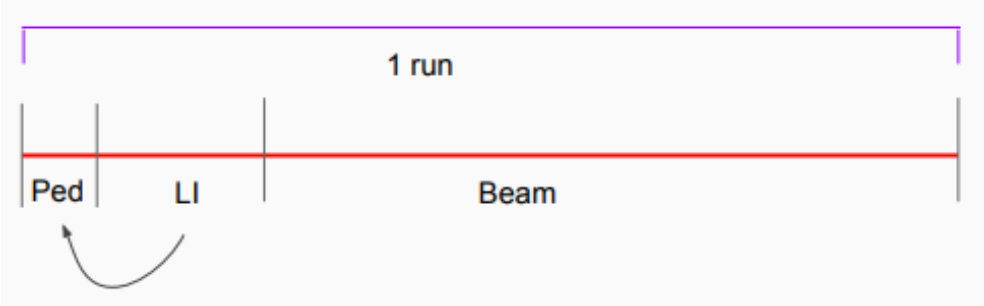

FIGURE 3.4: Composition of a run. In each case the each readout gate is opened $30ns$ for LI, $16\mu s$ for pedestal and $10\mu s$ for beam mode.

to its chain interface to which is connected to and finally the label from the right [3] corresponds to the board it belongs to. The labeling available for the crocs, chains and boards is as follows:

- Crocs from 0 to 3.
- Chains from 0 to 4.
- Boards from 0 to 5.

For a more detailed explanation about TB electronics (croc, chain, board, etc) please see Appendix C. If some combination of croc, chain and board are not present in a given FEB, it means that either one croc, chain or board has been replaced, damaged or discarded. In this work, data with 40 FEBs were taken. Fig. 3.5 sketches the process of a typical LI process at TB detector. First, the LED has to be ready and correctly synced with the DAQ system, after the trigger coming from the DAQ is set a 30 ns pulse of blue ALGaInP LED is directed from the WLS to the PMT. Once the incoming light make its way to each PMT (40 PMTs $\times$ 64 pixels each) the out going photo-electric signal (at this point already amplified $\sim 10^6$ times) goes to the DAQ system in order to get a digital signal.

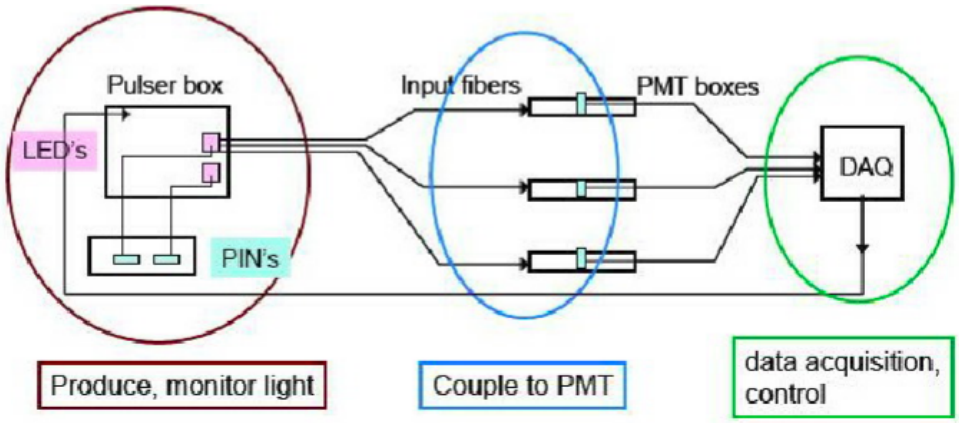

FIGURE 3.5: Diagram of LI setup for TB detector showing each stage of the LI process [55].

Chapter 4

Experimental Results and Conclusions

4.1 Data Taking

4.1.1 Temperature Analysis

- The temperature recorded in the surroundings of the TB facility will be called **"room temperature (T_{room})"**. This means that each PMT will be assumed to have the same "room temperature/date" despite each PMT is placed in a different 3D location (first approximation, zero law of thermodynamics, see fig. 4.1) .

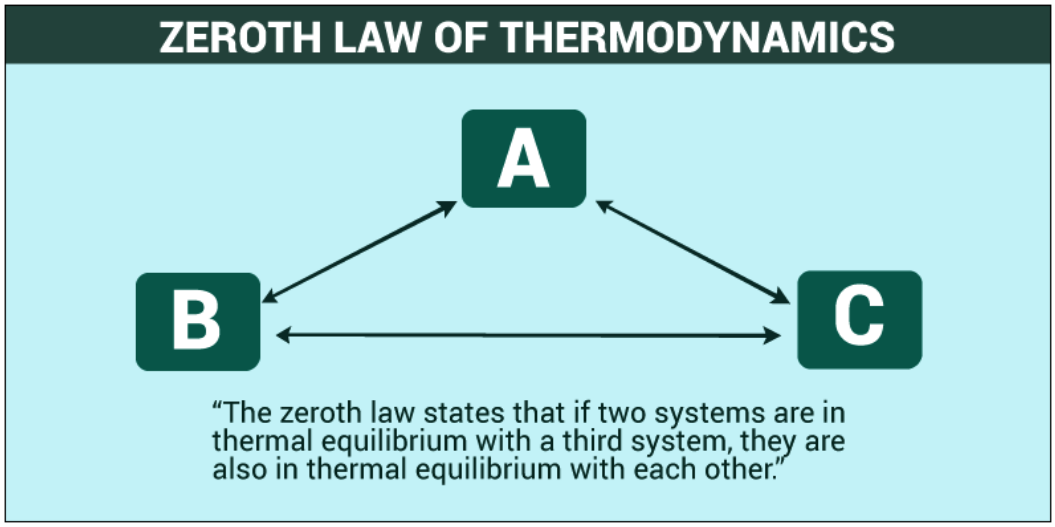

FIGURE 4.1: Sketch of the zeroth law of thermodynamics [59].

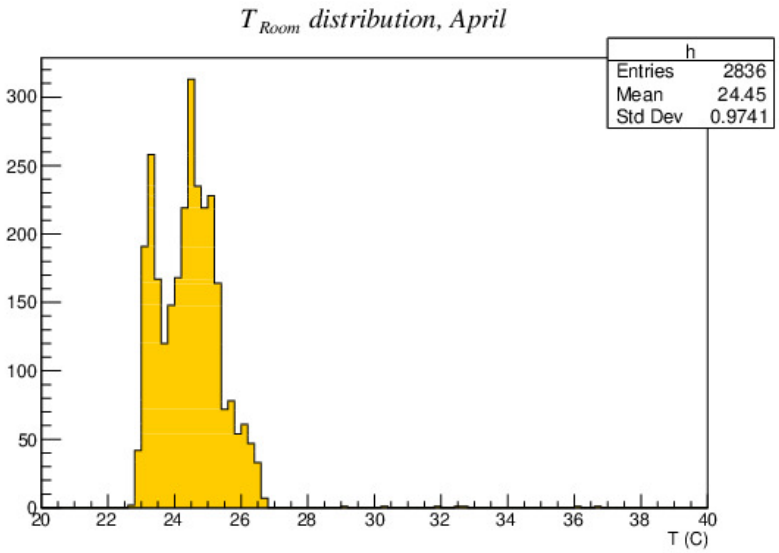

FIGURE 4.2: T_{room} distribution (all FEB) from April 6, 2015 17 : 23 : 20 to April 21, 2015 03 : 08 : 48

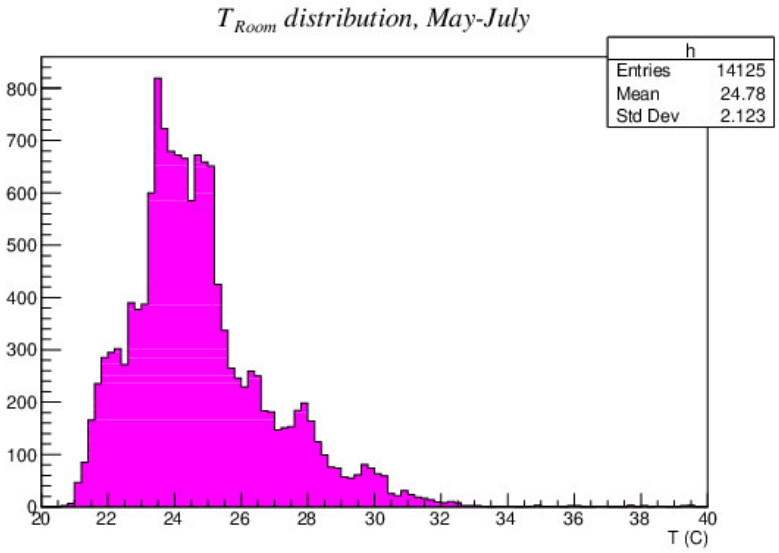

FIGURE 4.3: T_{room} distribution (all FEB) from April 24, 2015 05 : 22 : 48 to July 1, 2015 12 : 55 : 24

- The temperature recorded with the built-in sensor of the PMT will be called **"chip temperature (T_{chip})"**. This case is a more realistic compared to the previous one. The temperature sensor of each PMT records its own temperature and the recordings are independent one another. In this case one gets a temperature distribution as T=T(x,y,z,t).

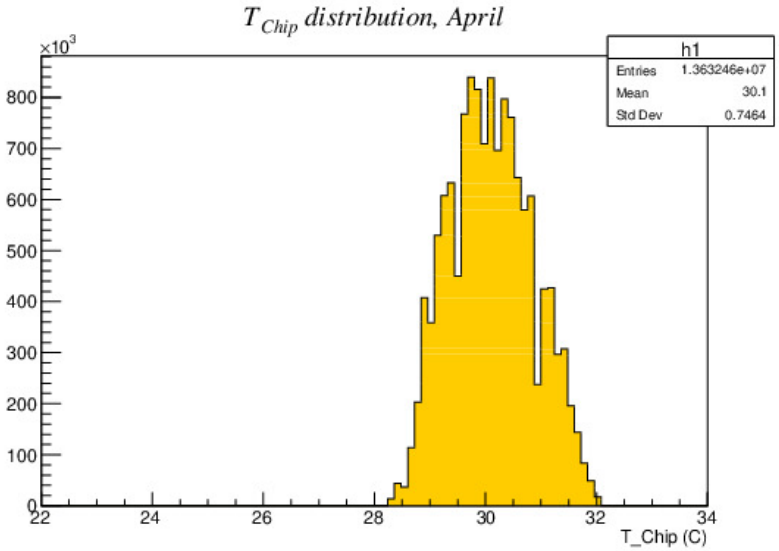

FIGURE 4.4: T_{Chip} distribution (all FEB) from April 6, 2015 17 : 23 : 20 to April 21, 2015 03 : 08 : 48

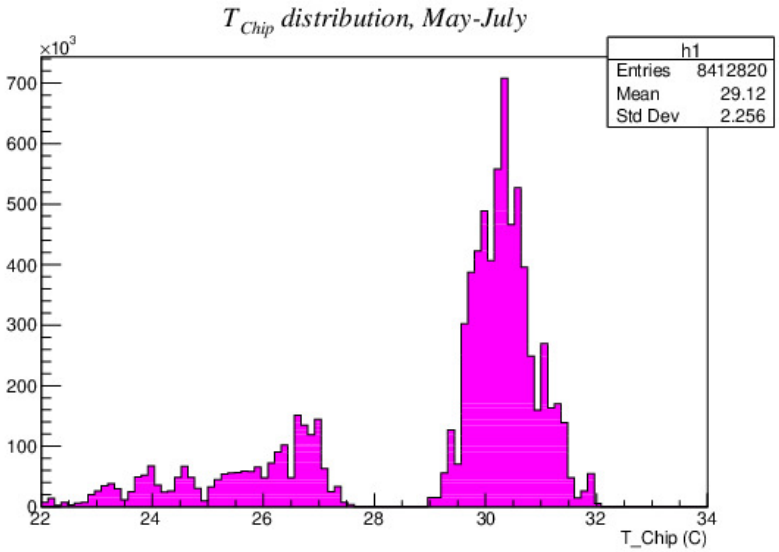

FIGURE 4.5: T_{Chip} distribution (all FEB) from April 24, 2015 05 : 22 : 48 to July 1, 2015 12 : 55 : 24

The T_{chip} was recorded directly from each individual FEB (it were considered 40 tubes out of 43) and stored in root files. To see T_{chip} distribution for each FEB in detail here: Appendix B

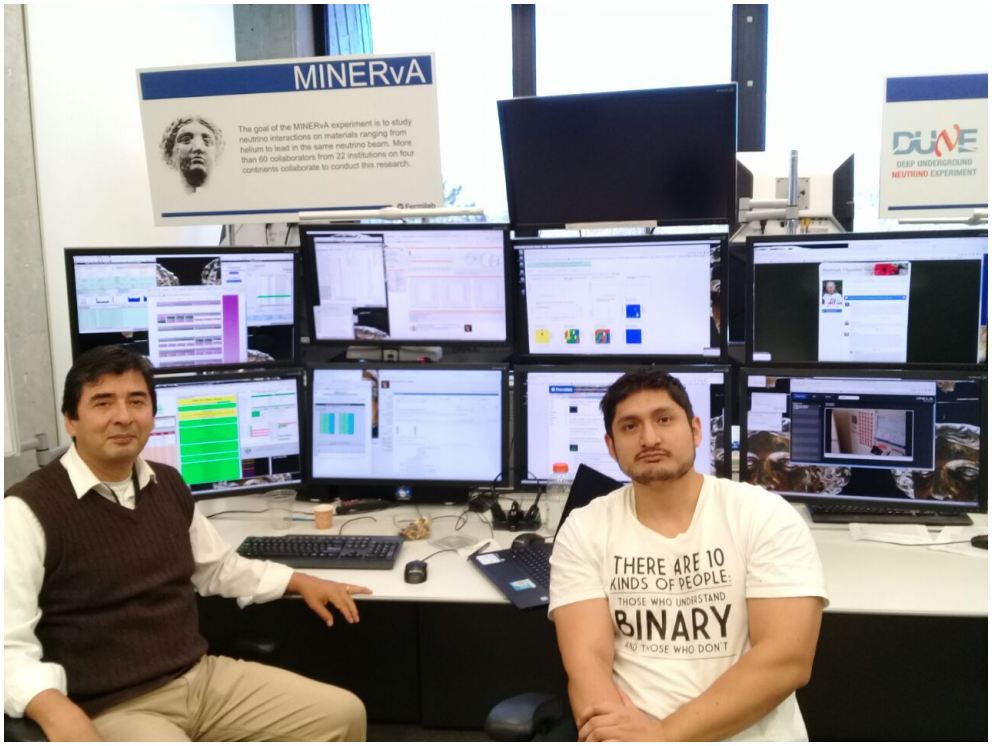

FIGURE 4.6: A usual data-taking period "shift"

For this work, 40 PMT tubes were considered (The manufacturer of this PMT tubes is Hammamatsu electronics), each of them has 64 pixels(channels). We made this study with 22 runs for EH Configuration (April) and 14 runs for SuperHcal Configuration (May-July). **IN TOTAL WERE**: $34 \cdot 40 \cdot 64 = 87040$ pixel-gain considered (**THIS IS A HUGE AMOUNT OF DATA!**)

4.2 PMT Gains Calculations

We compute PMT gains from a controlled light source (LED) and use LI and Ped parameters to generate PMT gain measurements. We calculate such gains as follows [10]:

In order to compute PMT gains, the process showed in pag. 29 has to be done and the parameters generated in LI can be inserted to the next set of equations:

$$g = \frac{\sigma_N^2 - \sigma_P^2}{\overline{Q}(1+w^2)} \tag{4.1}$$

- $\bar{Q}$ is the mean pedestal-subtracted charge of the PMT charge distribution.
- $\sigma(Q)$ is the sample width of the channel's PMT charge distribution.
- $\sigma(P)$ is the sample width of the channel's pedestal distribution.

- 1 + $w(g)^2$ is a correction factor that can be expanded in series.

$$\sigma_g = g\sqrt{\frac{2}{(\sigma_Q^2 - \sigma_P^2)^2}\left(\frac{\sigma_Q^4}{N_Q - 1} + \frac{\sigma_P^4}{N_P - 1}\right) + \frac{1}{\overline{Q^2}}\left(\frac{\sigma_Q^2}{N_Q} + \frac{\sigma_P^2}{N_P}\right)} \tag{4.2}$$

- N_Q Number of gates in the channel's PMT charge distribution.
- N_P Number of gates in the pedestal distribution.

For more details about this formulas 4.1 and 4.2 please check the reference [10].

4.3 Detector Configurations and Data

4.3.1 EH Configuration

This configuration is made of 20 Electromagnetic Calorimeter Planes(Pb) and 20 Hadronic Calorimeter Planes(Fe) with scintillator material interleaved between. For this configuration I used LI data and Ped data from runs: 1301, 1307, 1320, 1327, 1329, 1335, 1404, 1406, 1410, 1417, 1421, 1425, 1450, 1455, 1457, 1460, 1467, 1475, 1479, 1482, 1491 and 1495.

4.3.2 SuperHcal Configuration

This configuration is similar to the former one, but has doubled the number of Hadronic Calorimeter Planes, that's why "Super". For this configuration I used LI data and Ped data from runs: 1515, 1521, 1523, 1525, 1527, 1529, 1533, 1535, 1537 and 1540 (1707, 1722, 1726 and 1729 are not considered).

The following plots were computed using the weighted average approach, please see [19]. In order to get a gain with its error bars out of a bunch of gains and errors with different sizes, the weighted average approach was used. The gains that lie within a bin of temperature (the temperature bins can be divided in any size): g_1,g_2...g_n and their errors: $gerr_1$,$gerr_2$...$gerr_n$.

$$g_{av} = \frac{\sum_{i=1}^{n} w_i g_i}{\sum_{i=1}^{n} w_i}$$
$$gerr_{av} = \frac{1}{\sqrt{\sum_{i=1}^{n} w_i}} \tag{4.3}$$

where : $w_i = 1/gerr_i^2$

4.3.3 Getting the best fitting function under the chi-squared criterion

TABLE 4.1: Different fitting functions for PMT gain vs temperature.

Fitting function	T_{room}		T_{chip}	
	EH (April)	**SuperHcal (May-July)**	**EH (April)**	**SuperHcal (May-July)**
Straight line (chi^2/NDF)	0.422	8.260	3.380	7.905
Exponential (chi^2/NDF)	0.425	8.260	3.385	7.905
Gaussian (chi^2/NDF)	360.666	276.800	632.666	542.200

- Straight line: $g = p_1 T + p_0$
- Exponential: $g = e^{p_1 T + p_0}$
- Gaussian: $g = p_0 e^{-0.5(\frac{T-p_1}{p_2})^2}$

As can be noticed from the table 4.1 the values of chi^2/NDF for the Straight line and Exponential fitting curves are pretty close. The Straight line approach was chosen because is the first approximation in a Taylor's series expansion.

4.3.4 Previous Results from Others

This behavior of the PMT gains with changes in temperature has been previously reported by other authors. Here, it will be cited some previous results. Plots 4.7 and 4.8 show evidence of changes in temperature affect the PMT gains. In the left side shows this effect in the EH configuration. On the other hand, the right side shows a similar behavior for TE configuration

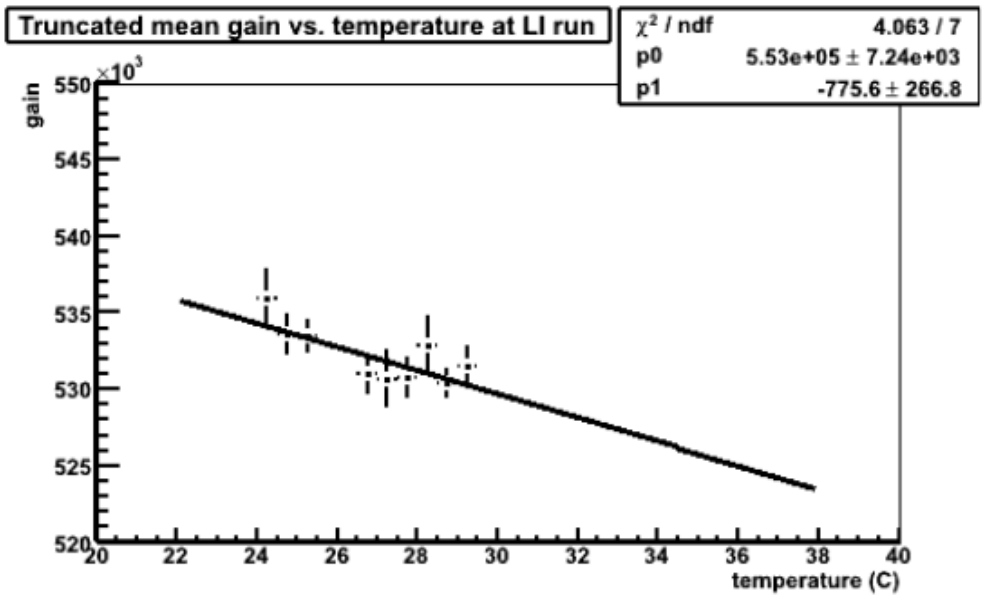

FIGURE 4.7: The effect of temperature changes over LI runs in EH configuration [56].

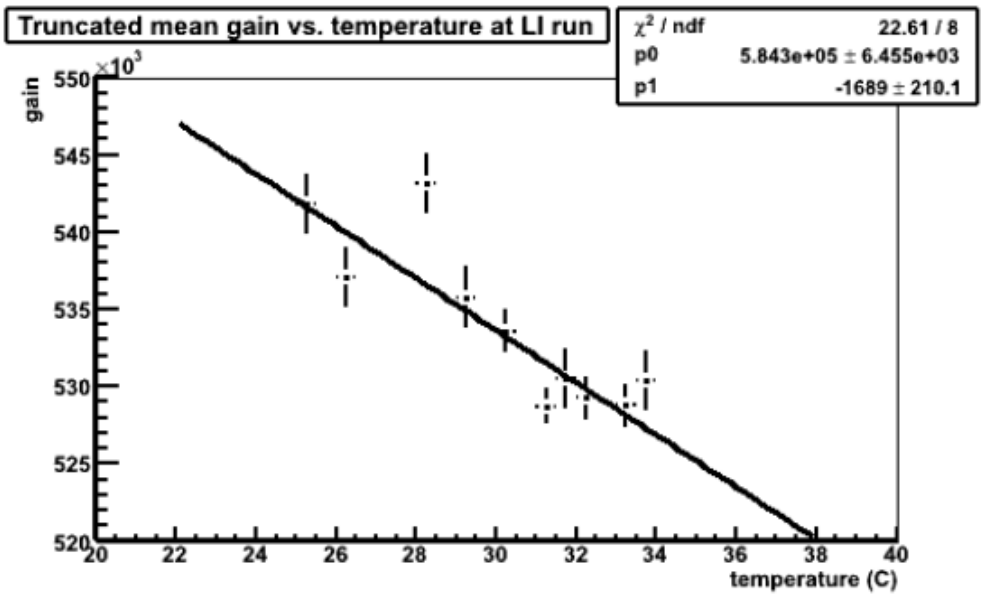

FIGURE 4.8: The effect of temperature changes over LI runs in TE configuration [56].

There is another collaboration that also found a similar effect but with a different PMT. In this case (fig. 4.9), DAMPER (DArk Matter Particle ExploRer) collaboration used the PMT Hamamatsu R4443.

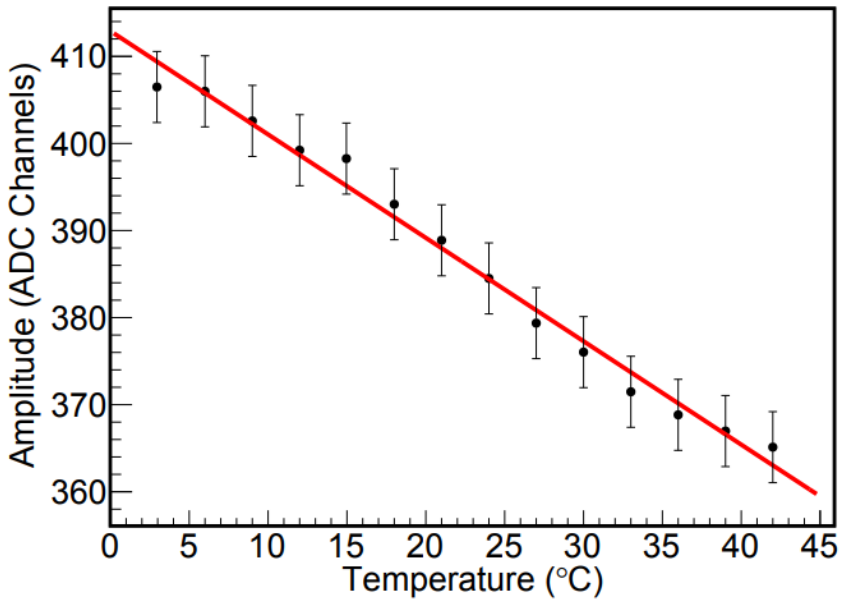

FIGURE 4.9: The effect of temperature found in the DAMPER collaboration [57].

These plots were made in ROOT version 5.34.05, ROOT version 6.10.02 and minerva framework v10r8p12 (Gaudi Framework).

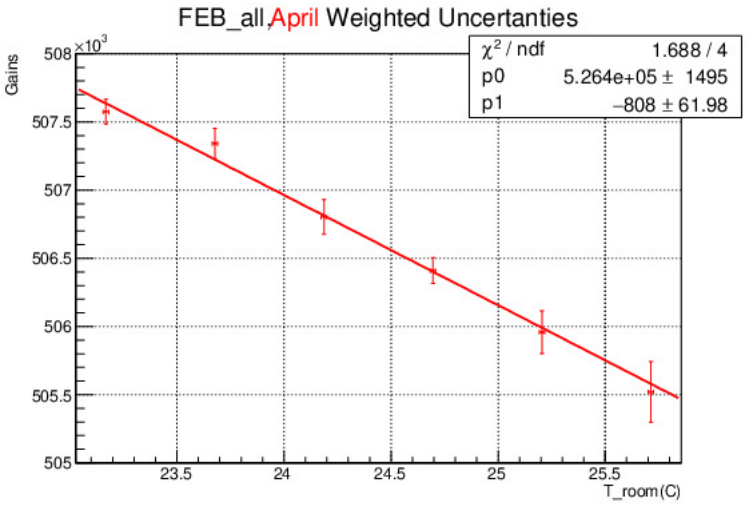

FIGURE 4.10: This plot shows the PMT gain (general tendency) as a function of room temperature in April (EH configuration). All PMT tubes.

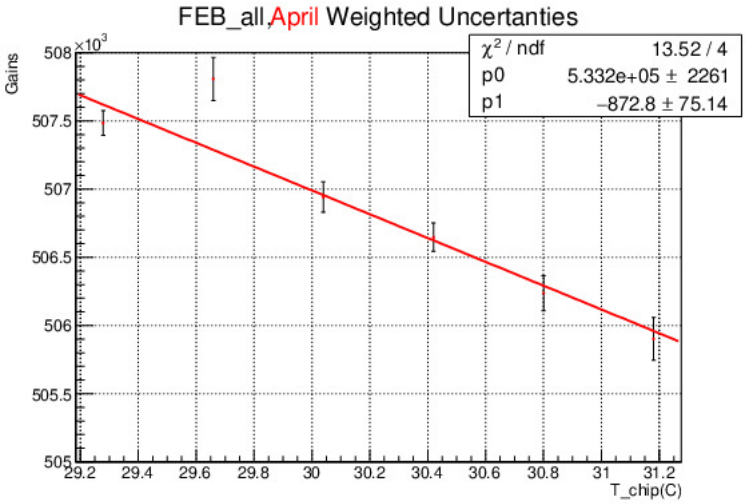

FIGURE 4.11: This plot shows the PMT gain (general tendency) as a function of chip temperature in April (EH configuration). All PMT tubes.

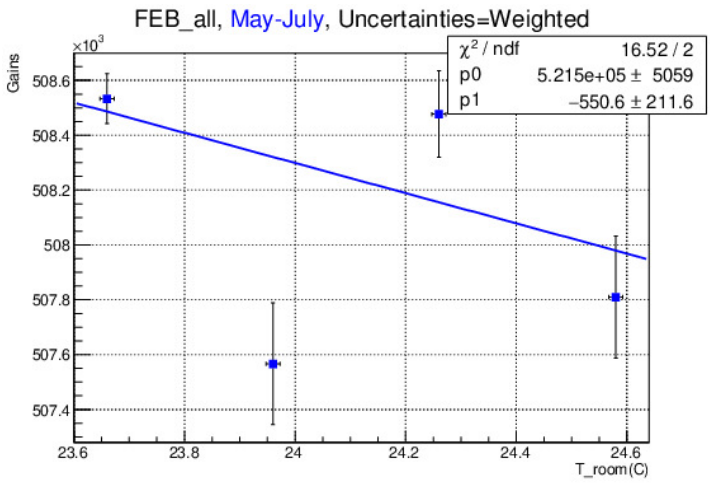

FIGURE 4.12: This plot shows the PMT gain (general tendency) as a function of room temperature in May-July (SuperHcal configuration). All PMT tubes.

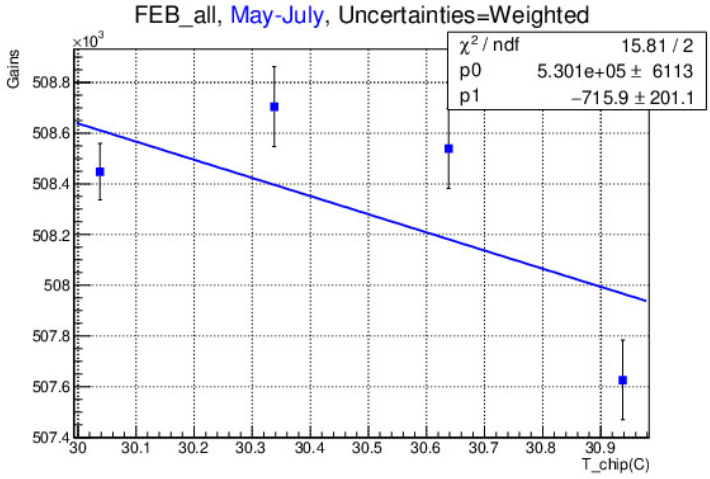

FIGURE 4.13: This plot shows the PMT gain (general tendency) as a function of chip temperature in May-July (SuperHcal configuration). All PMT tubes.

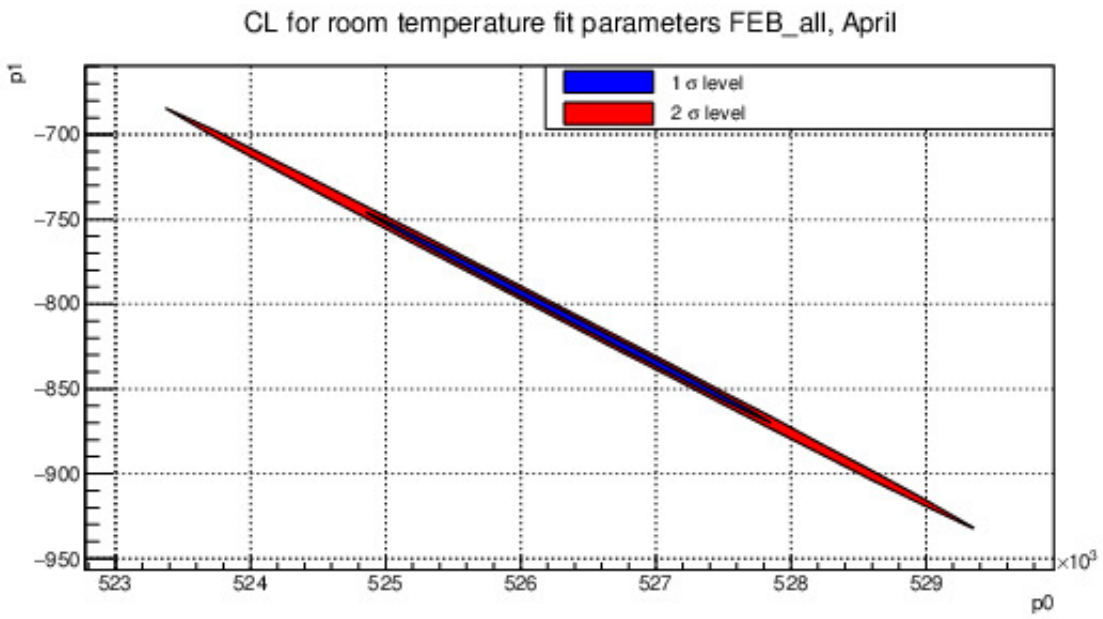

FIGURE 4.14: CL plots for room temperature, April.

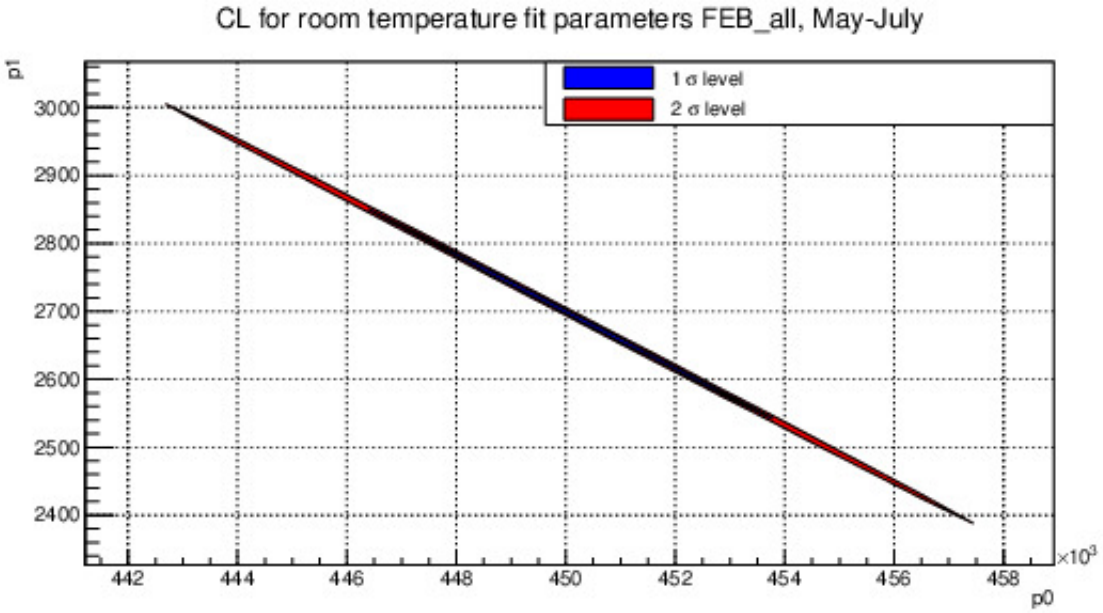

FIGURE 4.15: CL plots for room temperature, May-July.

4.4 Conclusions

- In EH configuration (red plots fig. 4.10 and 4.11) as in SuperHcal configuration (blue plots fig. 4.12 and fig. 4.13) one notices the drop of the gain when the temperature is increased (T_{room} or T_{chip}). Being the SuperHcal configuration a rather new configuration that still needs more calibration and optimization studies. For the EH configuration is practically confirmed that the temperature effect over the PMT gains is a a fact due to the EH configuration has been used for so long with calibration and optimization studies carried out accordingly,[10].

- It was found, according to the chi^2 criterion, that the best fitting-curve for modeling a PMT gain vs temperature plot is a straight line (all plots of Appendix A) for reasons discussed in table 4.1. Fig. 4.14 and fig. 4.15 represent confidence level plots for the fitting-parameters $p0$ and $p1$ of a straight line. For this specific fitting-curve (straight line) one notices that these parameters are content within $1-\sigma$ confidence level.

- T_{chip} is larger to T_{room} 5^oC in average. This happens due to the fact that the internal temperature sensor of the PMT also records electronic heating and noise from the environment. On the other hand T_{room} just records the temperature of the surroundings and a given time measures the same temperature for all PMT while T_{chip} shows a different temperature measurement at all times for each PMT. Despite the difference between T_{room} and T_{chip} one notices that the rate at which both configurations drop their gain is practically the same.

- The results obtained until now suggests that the quantum efficiency of the anode and the supply voltage in each dynode stage are being altered by temperature changes over certain range. In table 1.6 Hamamatsu suggest an optimal ratio of voltages for the dynodes, however this was supposed to work just well without taking into account temperature effects.

- The contributions of T_{room} and T_{chip} are practically the same because one notices the average statistic tendency over a large data-set used.

Appendix A

Gain Plots in Detail

A.1 These plots show the PMT gain as a function of room temperature/chip temperature in April(EH Configuration)

Plots from pag. 50 to 90 are plots in detail of each PMT gain (April, EH configuration) for each case (T_{room} and T_{chip}). Plots from pag. 42 to 49 show all the PMT tubes simultaneously to compare their PMT gains one another. Here are shown only the PMT gain for the first 10 tubes, to visualize the full set of PMT gain vs temperature plots of the 40 tubes, please see (pag. $44 - 141$) : https://drive.google.com/open?id=1IJ41$_{I}geI0FiGaSyTncecs4doDxaXuRp$

A.1.1 Configuration EH (April, room temperature), PMT tubes from 1 to 20

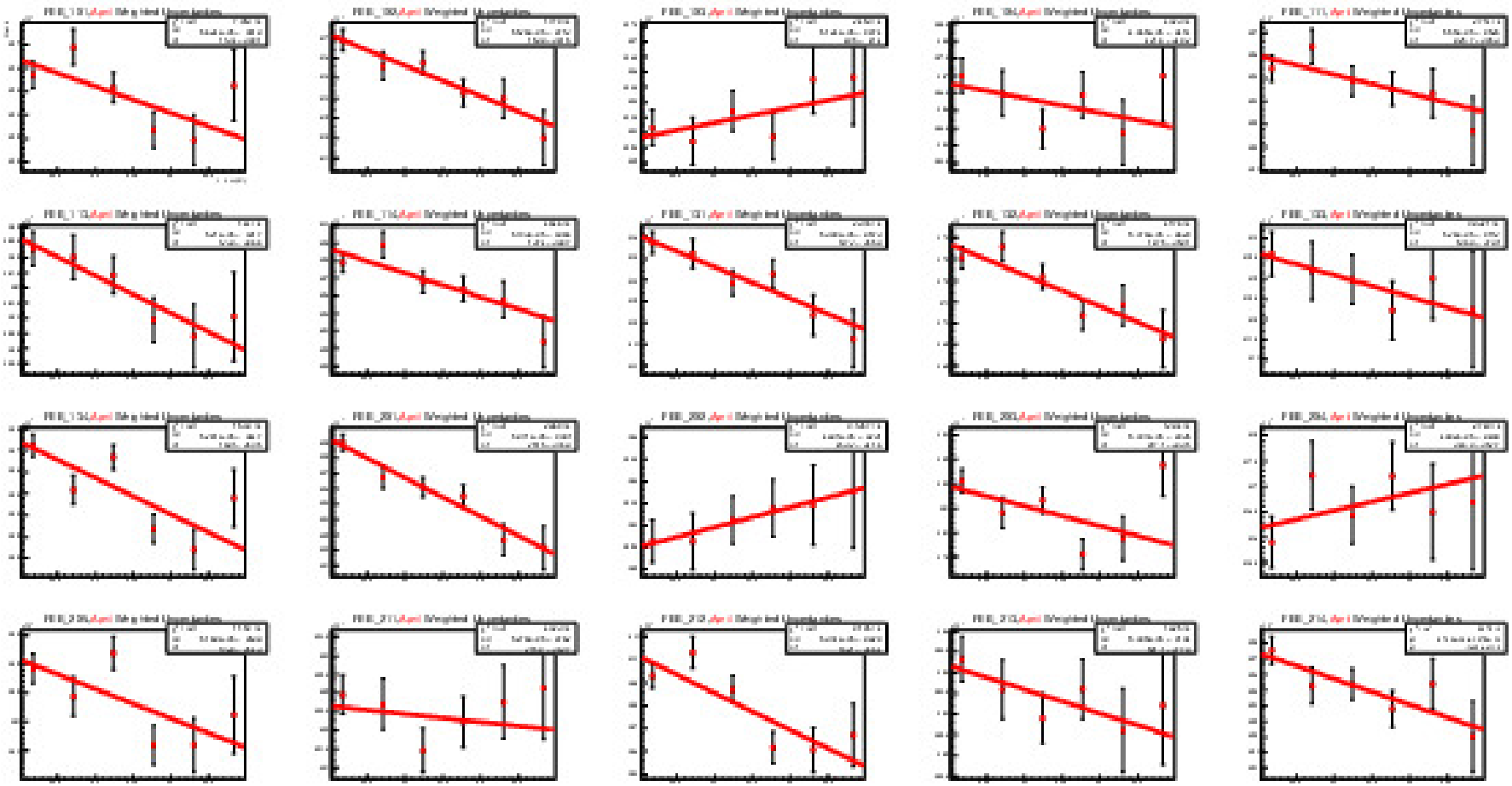

FIGURE A.1: These set of plots show the PMT gain as a function of room temperature in April (EH configuration). PMT tubes from 1 to 20.

A.1.2 Configuration EH (April, room temperature), PMT tubes from 1 to 20 and y axis normalized

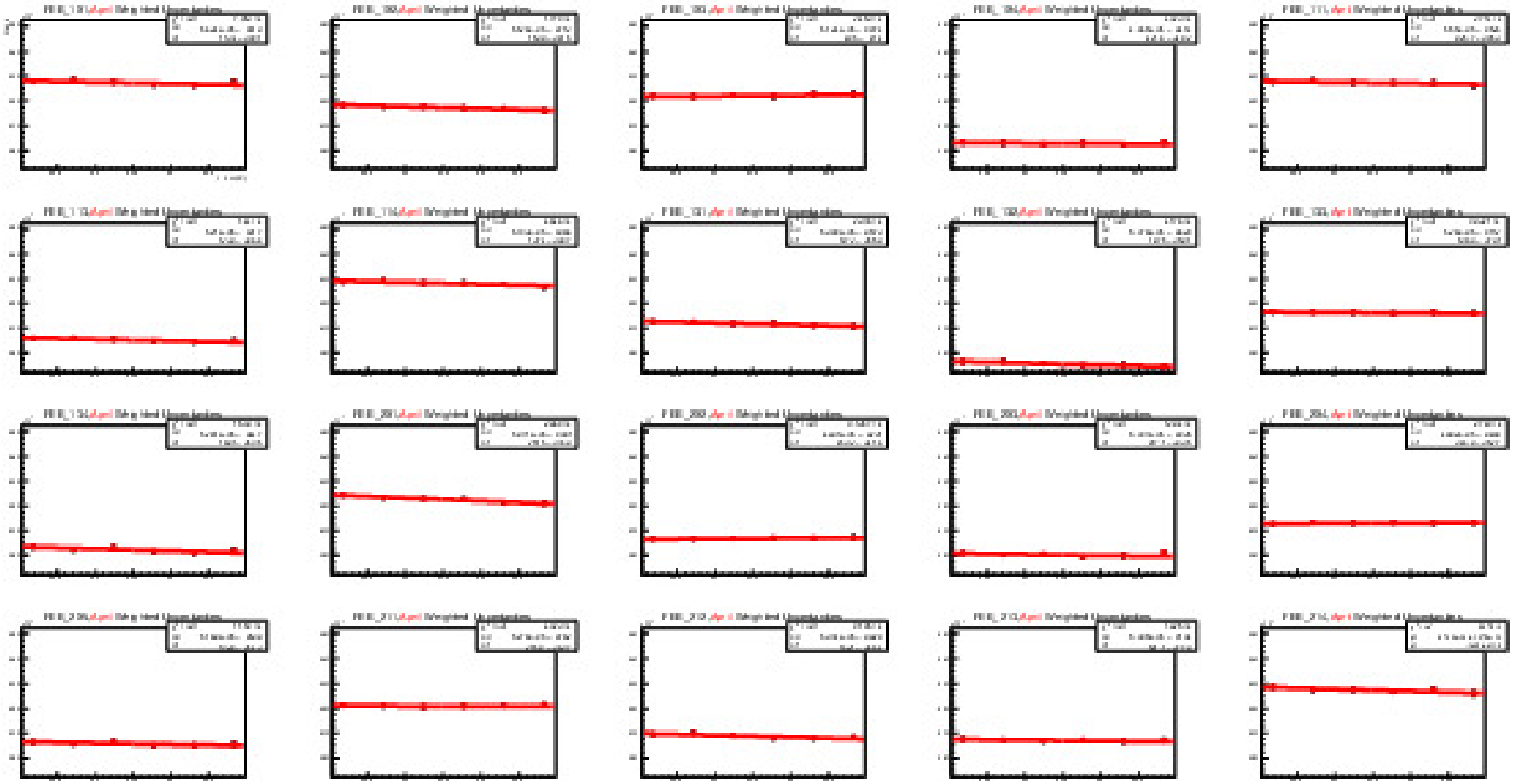

FIGURE A.2: These set of plots (normalized) show the PMT gain as a function of room temperature in April (EH configuration). PMT tubes from 1 to 20.

A.1.3 Configuration EH (April, room temperature), PMT tubes from 21 to 40

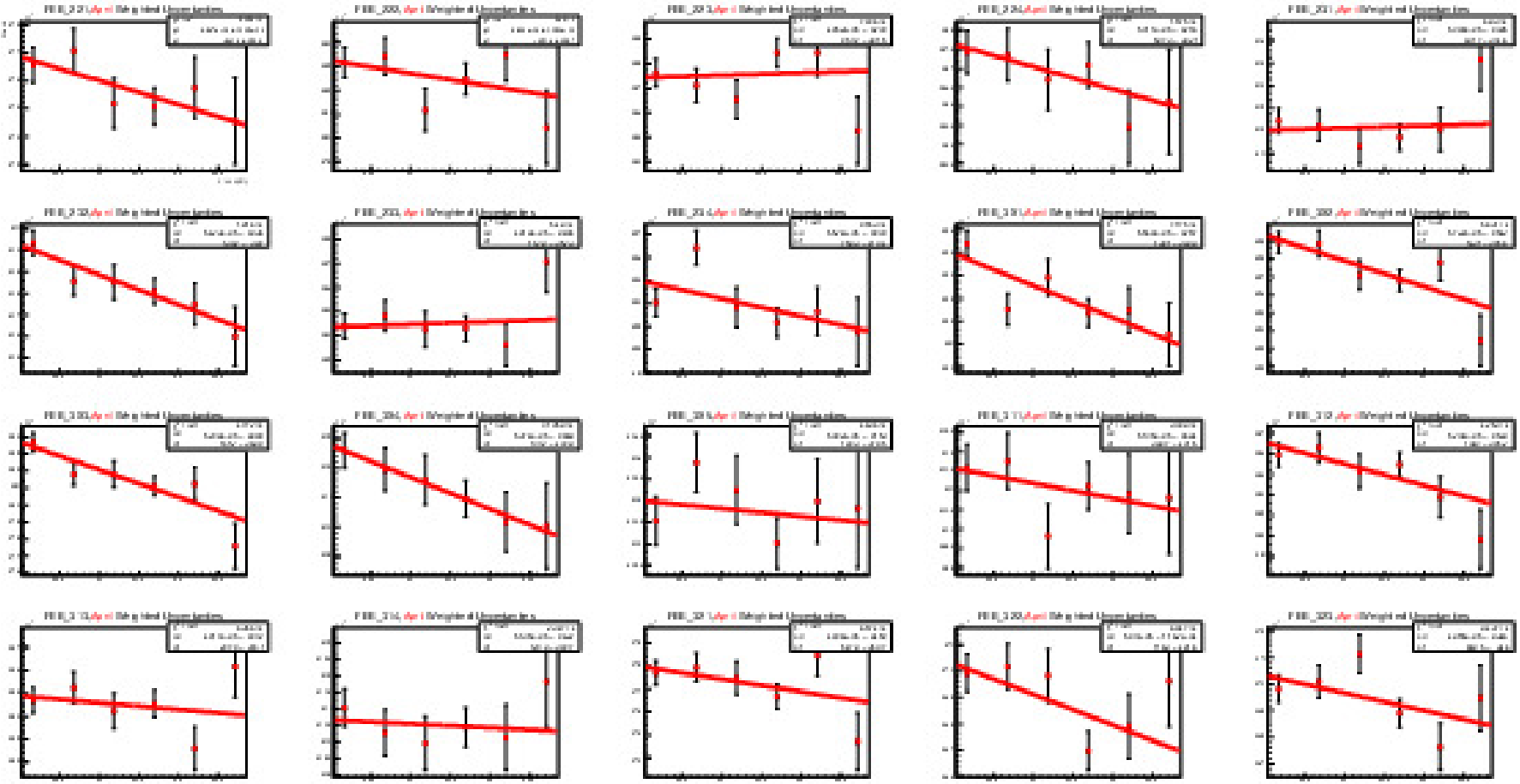

FIGURE A.3: These set of plots show the PMT gain as a function of room temperature in April (EH configuration). PMT tubes from 21 to 40.

A.1.4 Configuration EH (April,room temperature), PMT tubes from 21 to 40 and y axis normalized

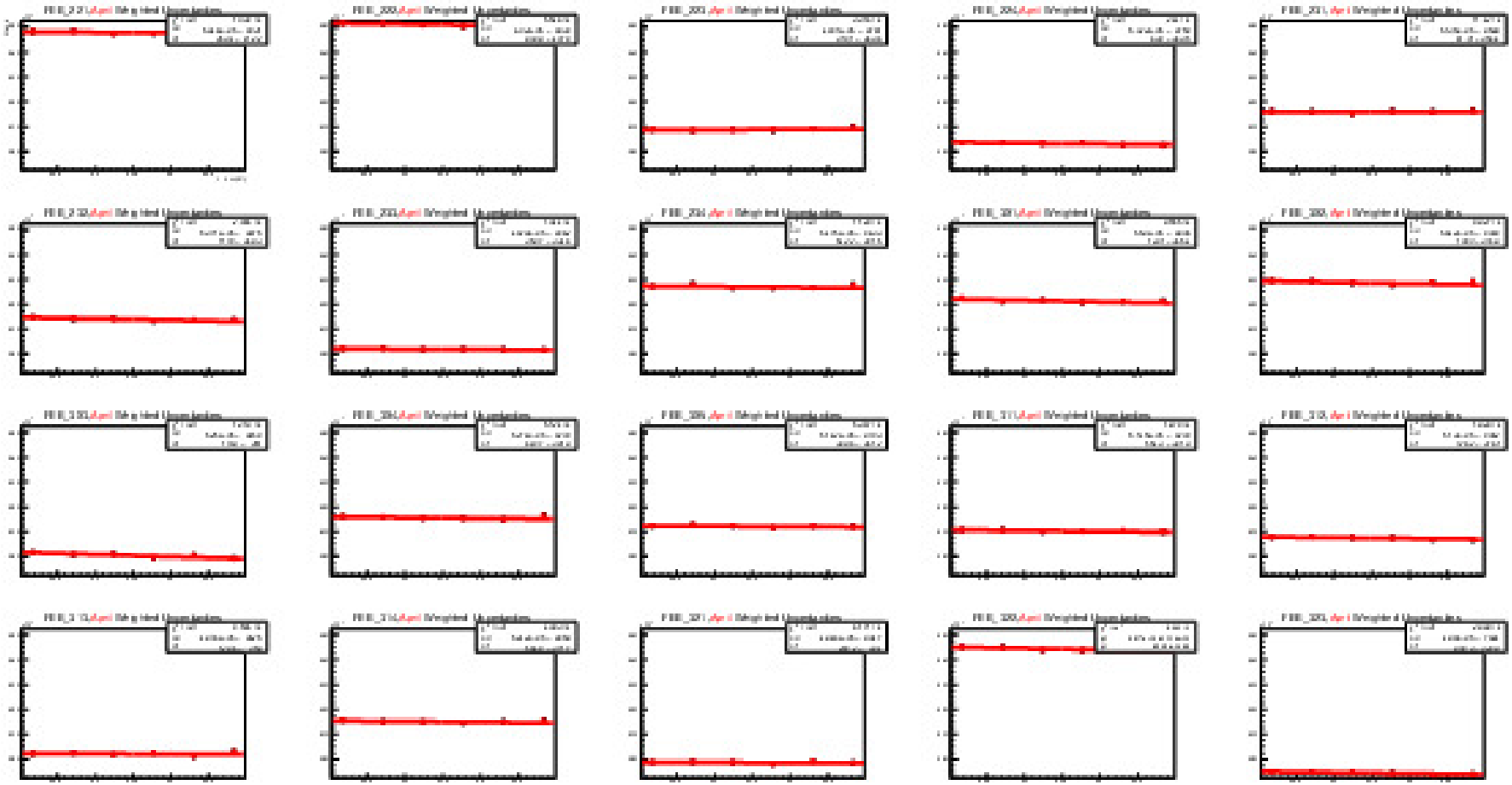

FIGURE A.4: These set of plots (normalized) show the PMT gain as a function of room temperature in April (EH configuration). PMT tubes from 21 to 40.

A.1.5 Configuration EH (April, chip temperature), PMT tubes from 1 to 20

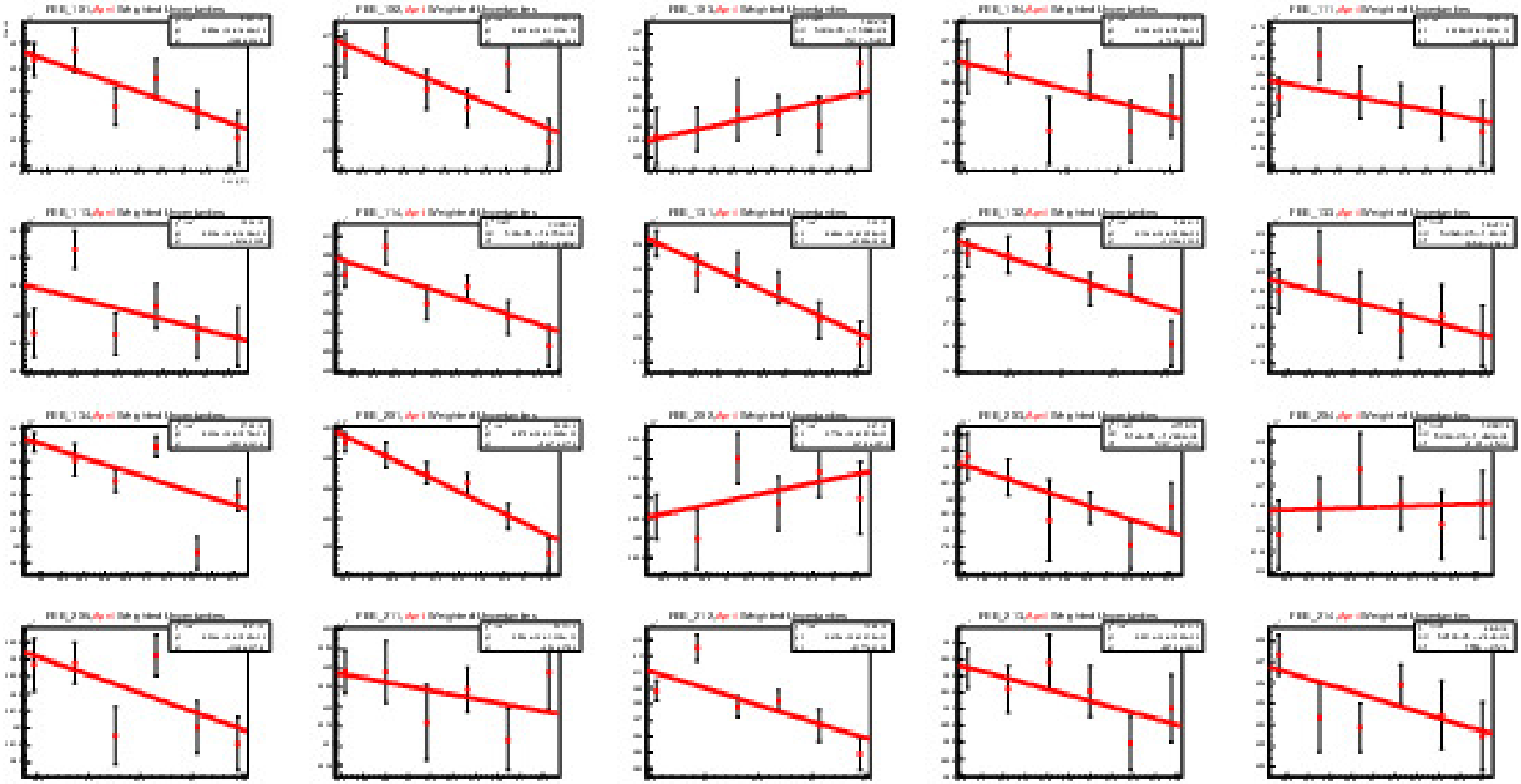

FIGURE A.5: These set of plots show the PMT gain as a function of chip temperature in April (EH configuration). PMT tubes from 1 to 20.

A.1.6 Configuration EH (April, chip temperature), PMT tubes from 1 to 20 and y axis normalized

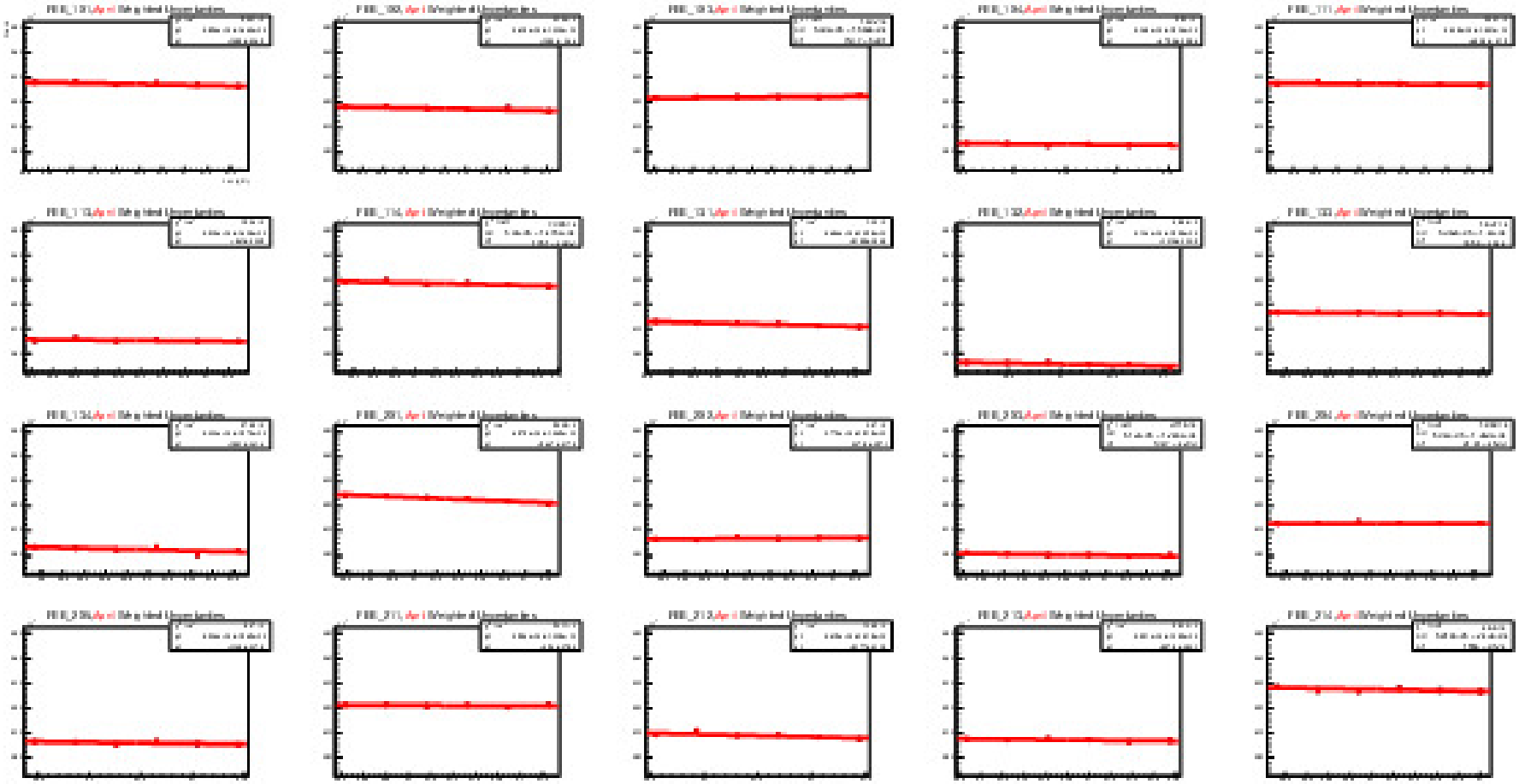

FIGURE A.6: These set of plots (normalized) show the PMT gain as a function of chip temperature in April (EH configuration). PMT tubes from 1 to 20.

A.1.7 Configuration EH (April, chip temperature), PMT tubes from 21 to 40

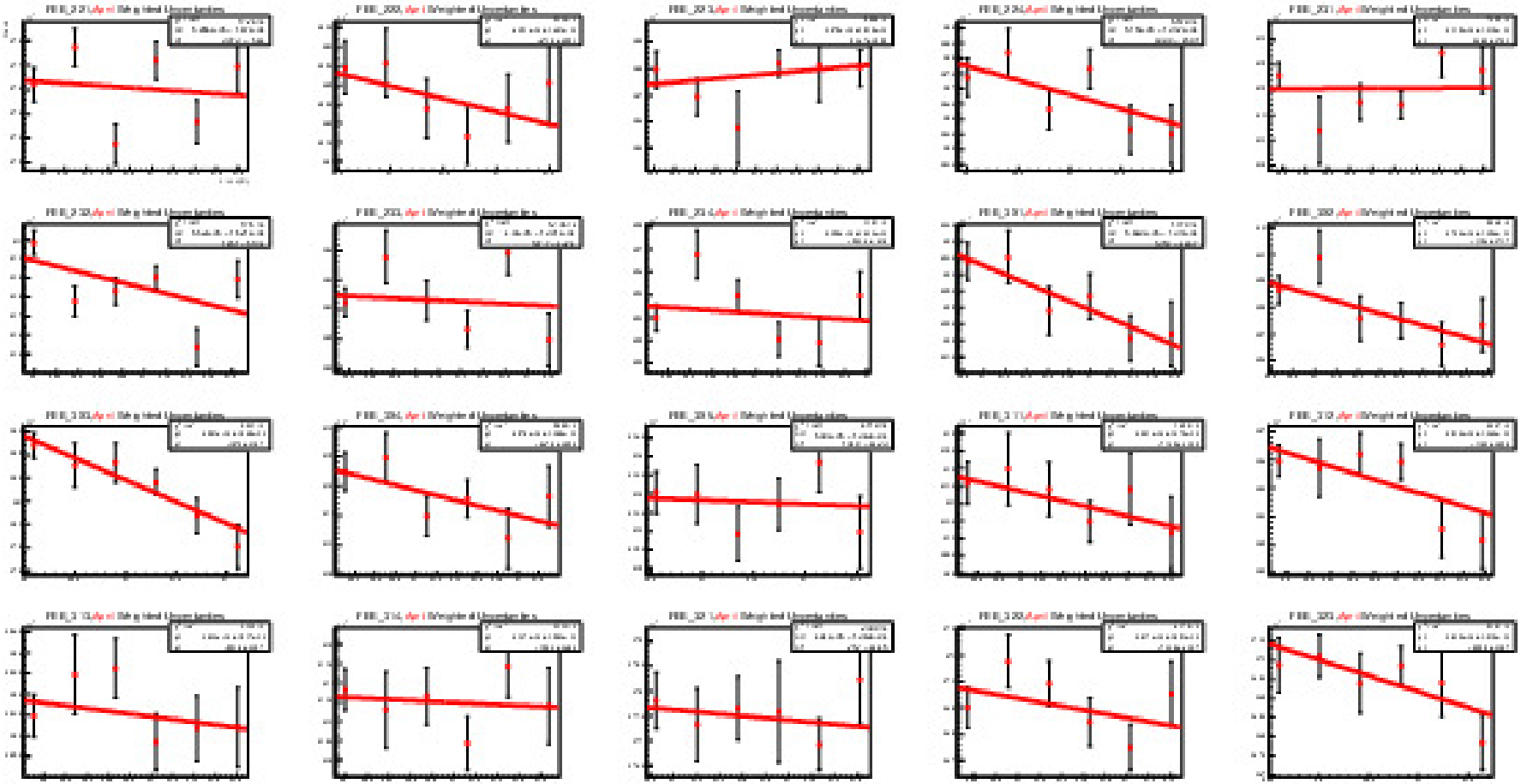

FIGURE A.7: These set of plots show the PMT gain as a function of chip temperature in April (EH configuration). PMT tubes from 21 to 40.

A.1.8 Configuration EH (April, chip temperature), PMT tubes from 21 to 40 and y axis normalized

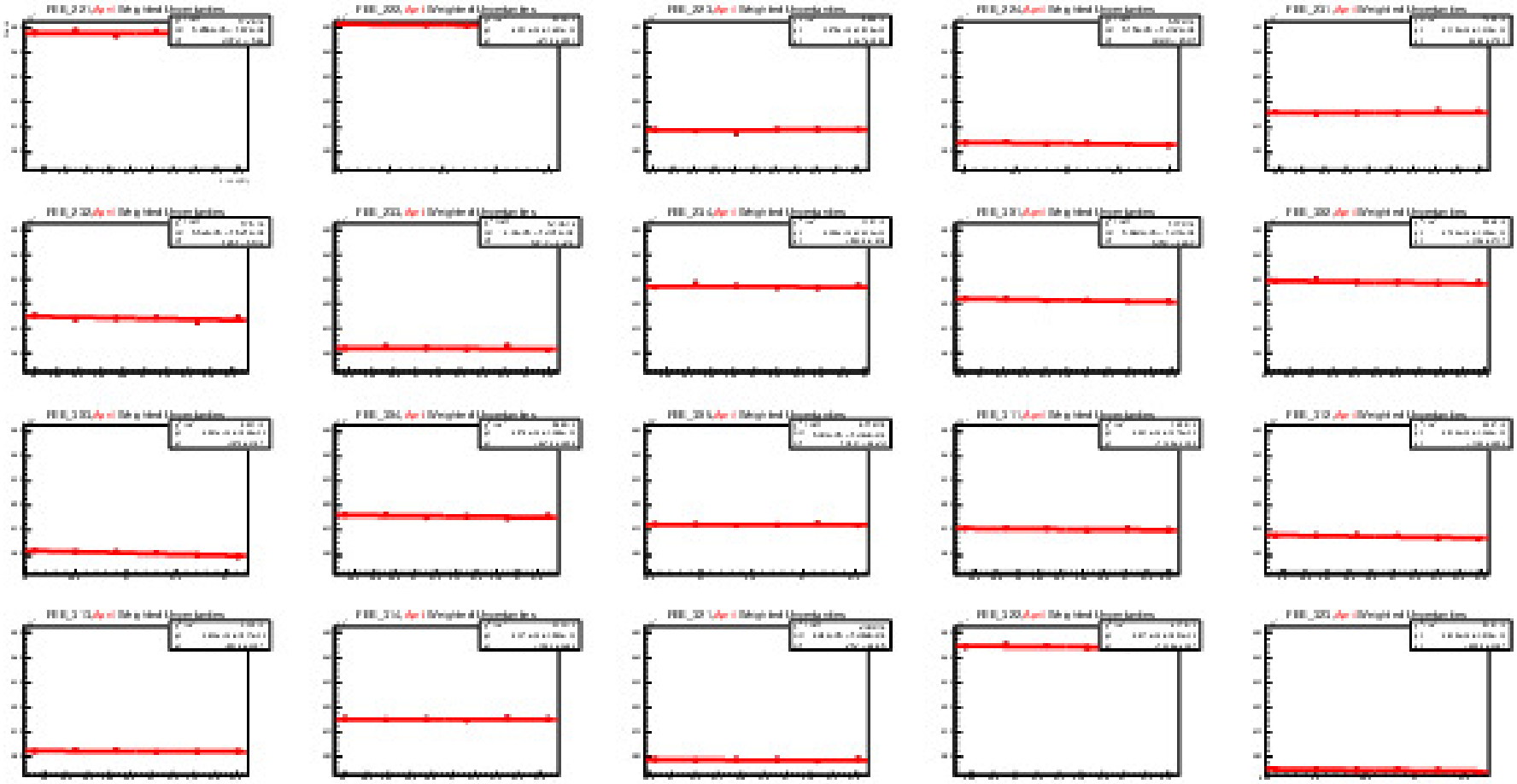

FIGURE A.8: These set of plots (normalized) show the PMT gain as a function of chip temperature in April (EH configuration). PMT tubes from 21 to 40.

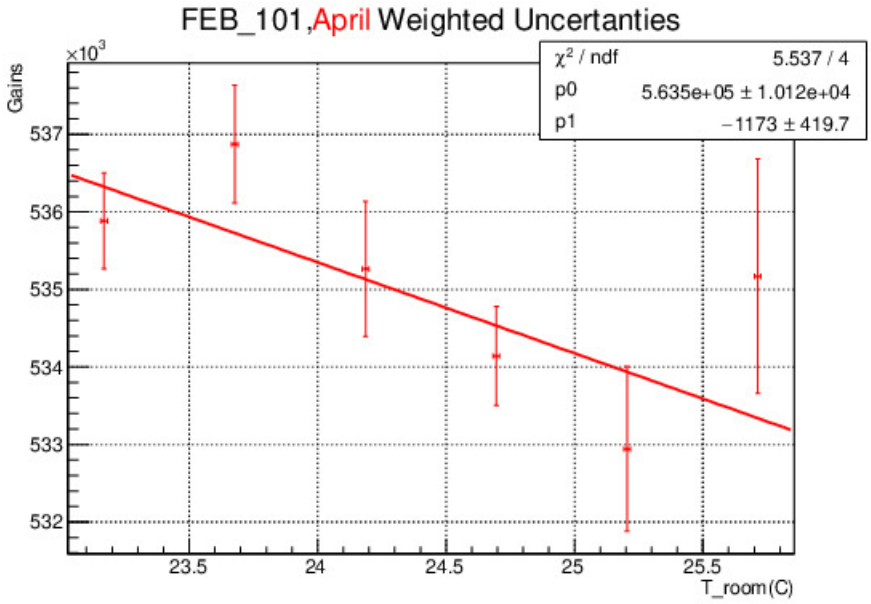

FIGURE A.9: PMT gain (EH configuration) vs T_{room}.

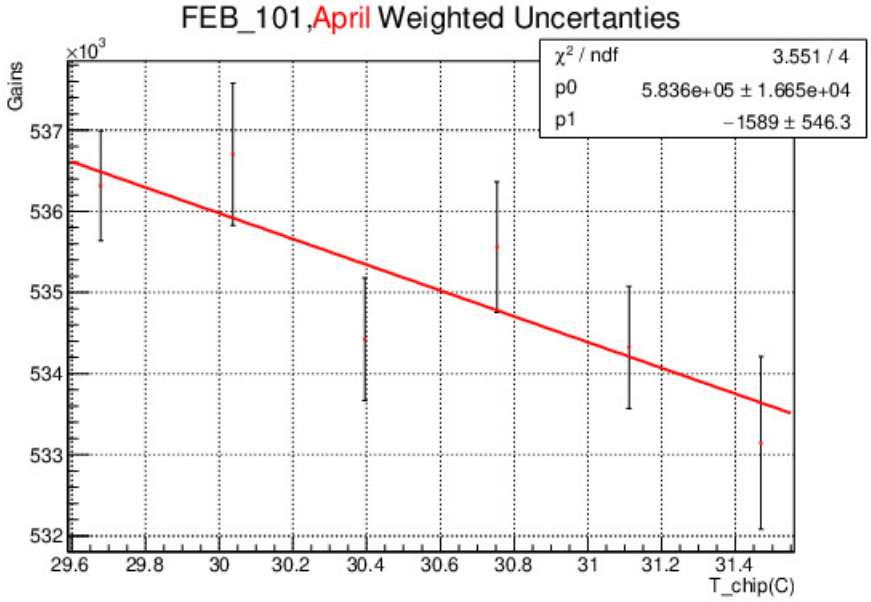

FIGURE A.10: PMT gain (EH configuration) vs T_{chip}.

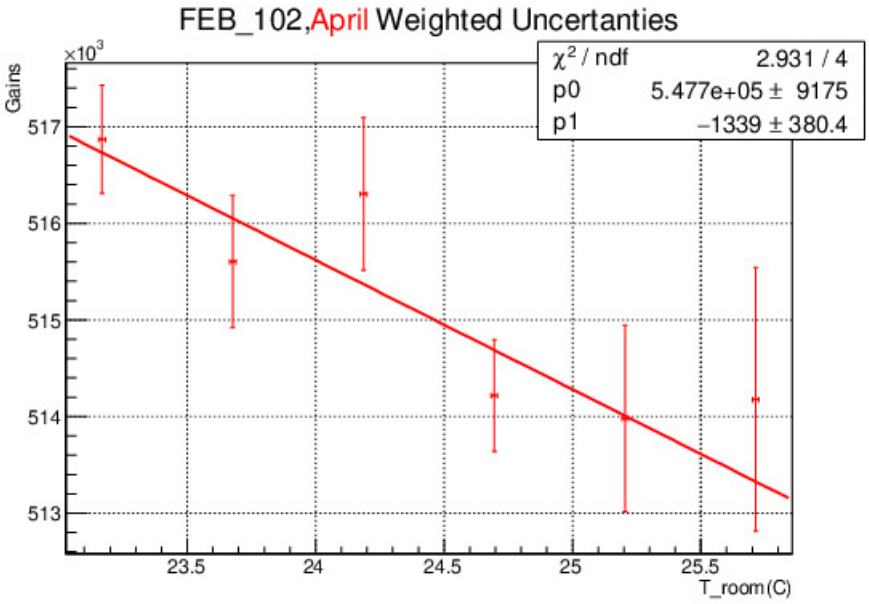

FIGURE A.11: PMT gain (EH configuration) vs T_{room}.

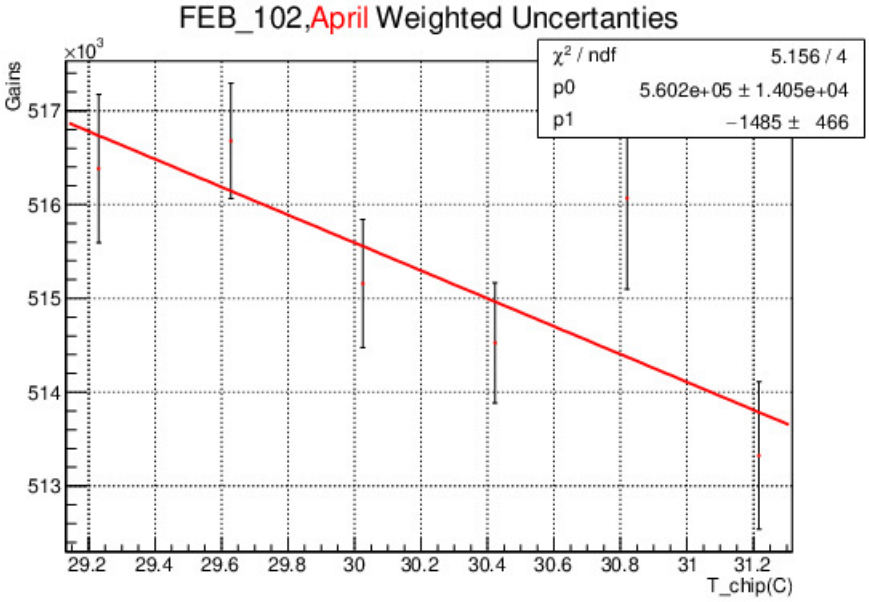

FIGURE A.12: PMT gain (EH configuration) vs T_{chip}.

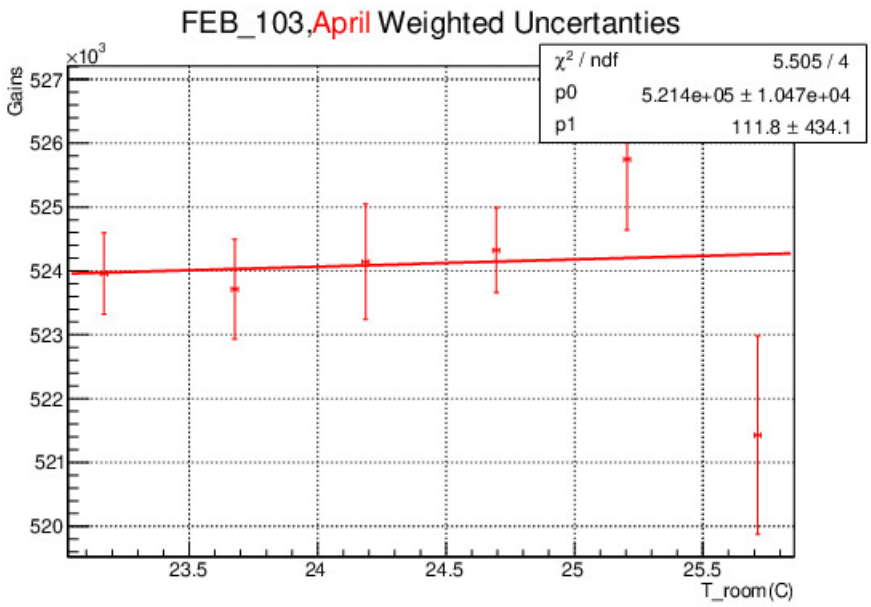

FIGURE A.13: PMT gain (EH configuration) vs T_{room}.

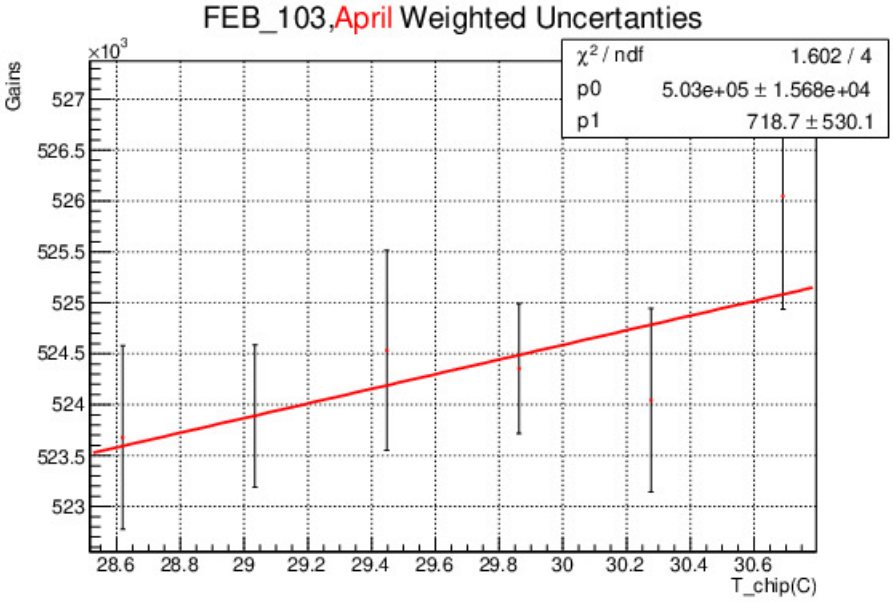

FIGURE A.14: PMT gain (EH configuration) vs T_{chip}.

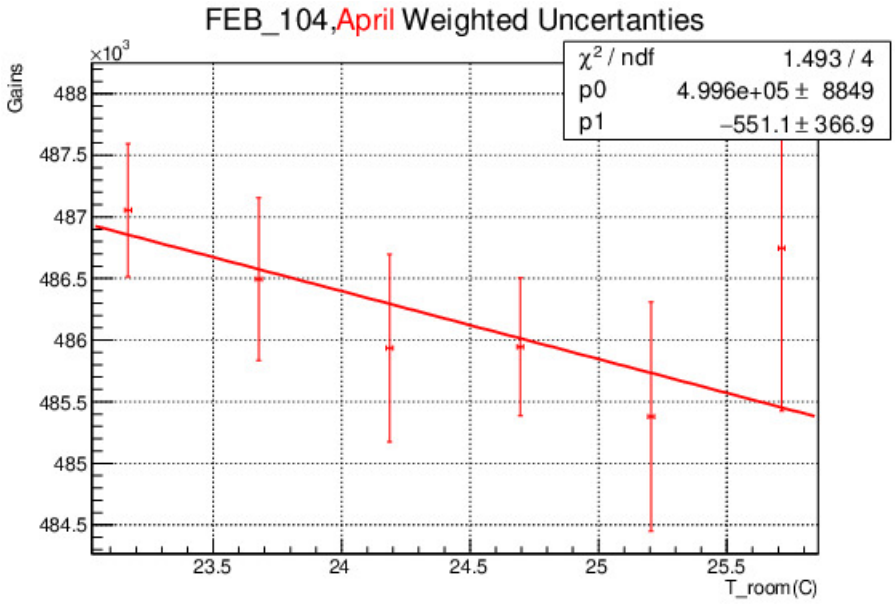

FIGURE A.15: PMT gain (EH configuration) vs T_{room}.

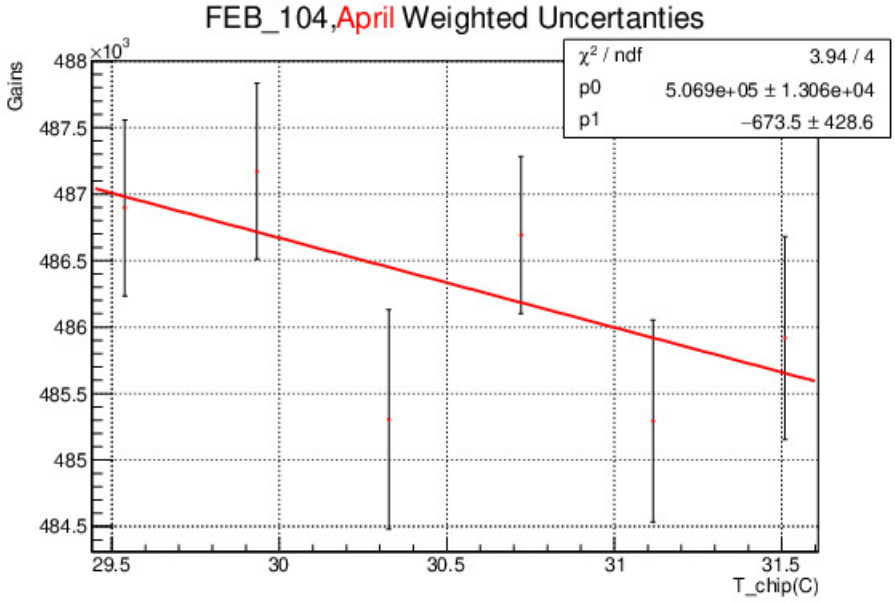

FIGURE A.16: PMT gain (EH configuration) vs T_{chip}.

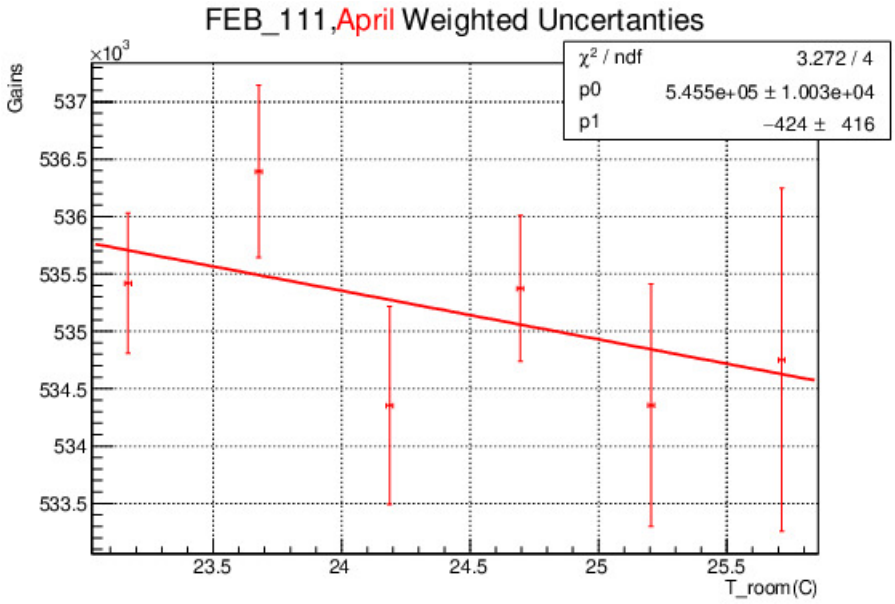

FIGURE A.17: PMT gain (EH configuration) vs T_{room}.

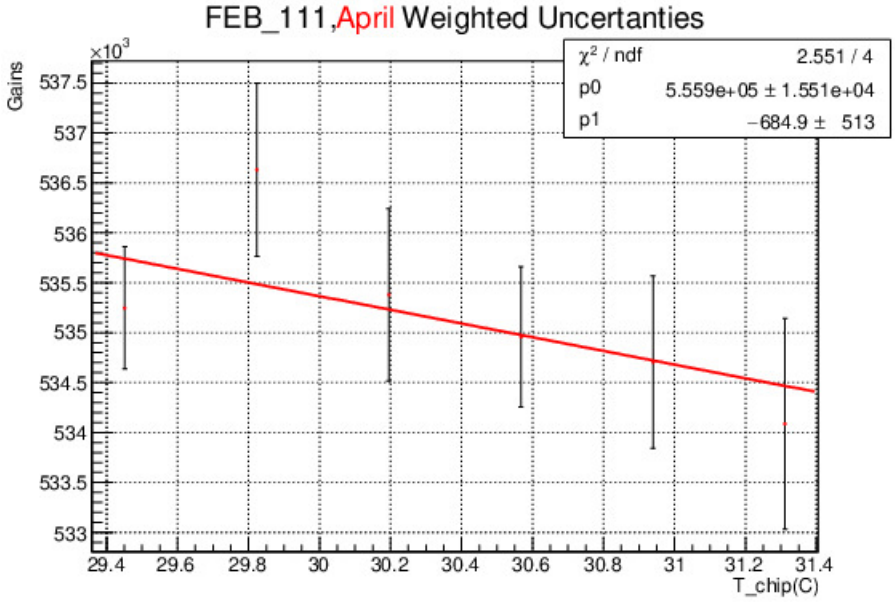

FIGURE A.18: PMT gain (EH configuration) vs T_{chip}.

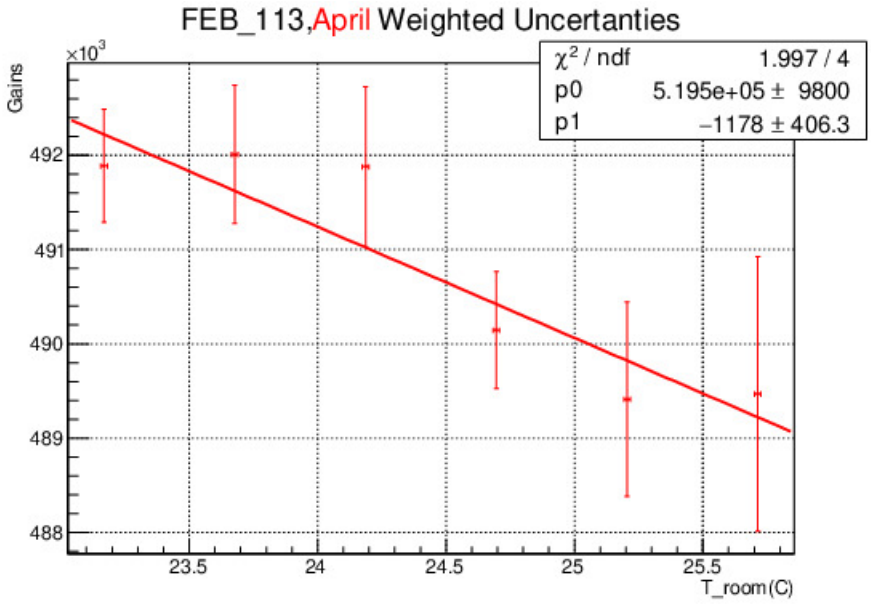

FIGURE A.19: PMT gain (EH configuration) vs T_{room}.

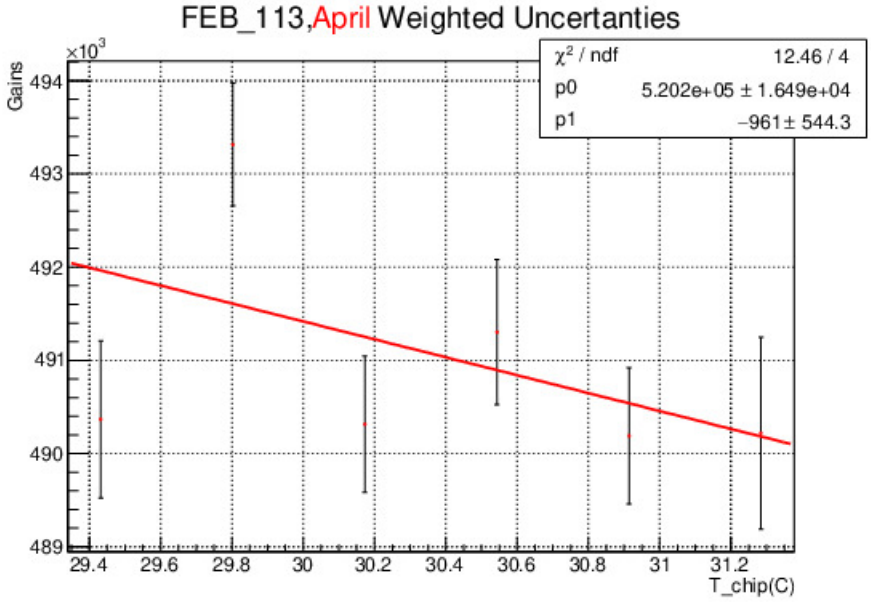

FIGURE A.20: PMT gain (EH configuration) vs T_{chip}.

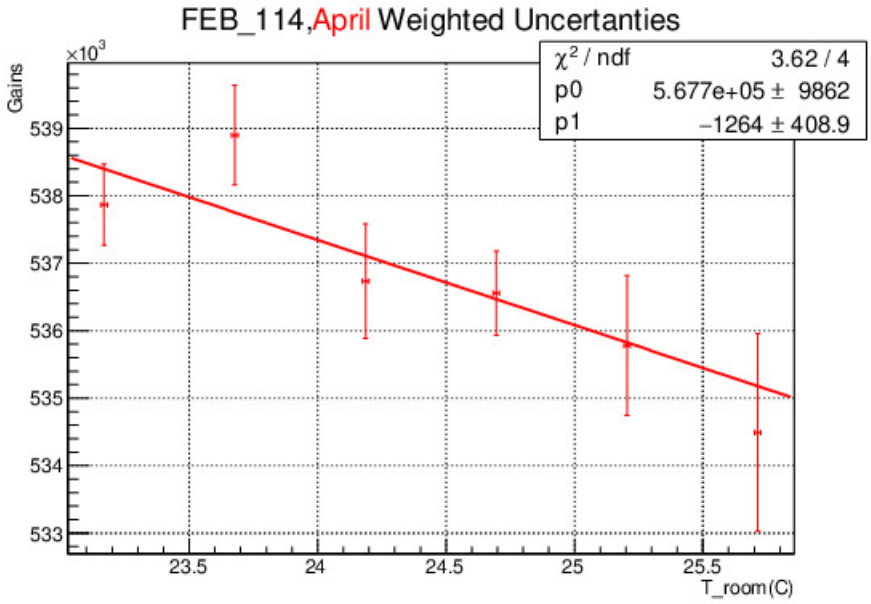

FIGURE A.21: PMT gain (EH configuration) vs T_{room}.

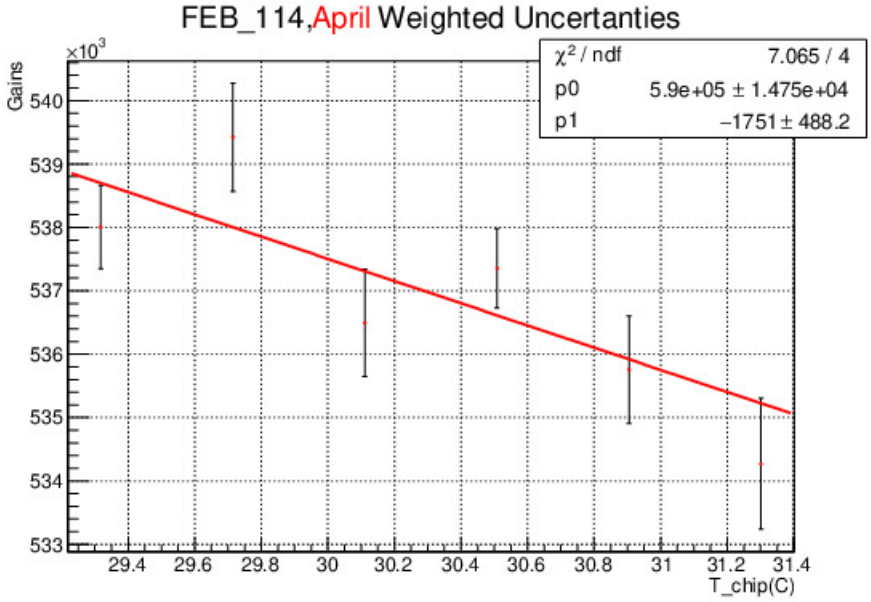

FIGURE A.22: PMT gain (EH configuration) vs T_{chip}.

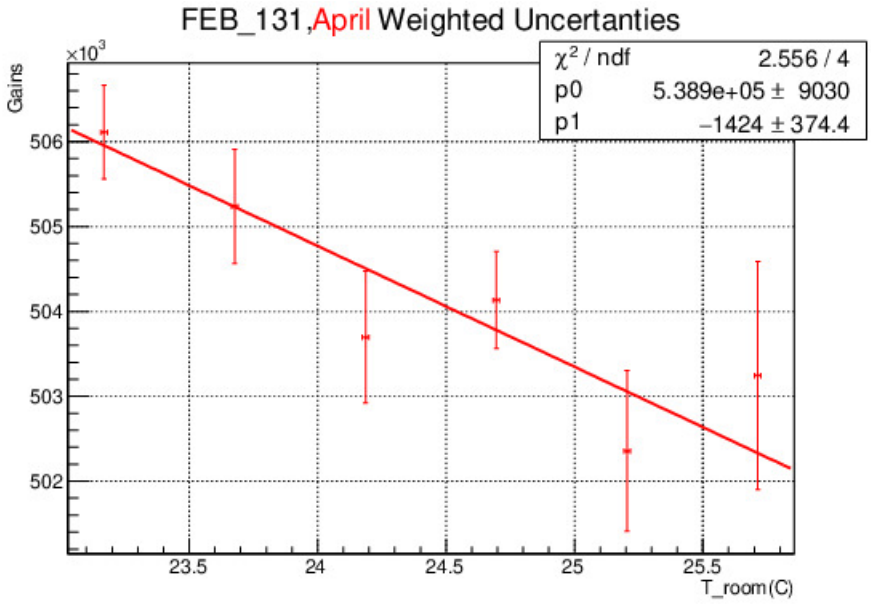

FIGURE A.23: PMT gain (EH configuration) vs T_{room}.

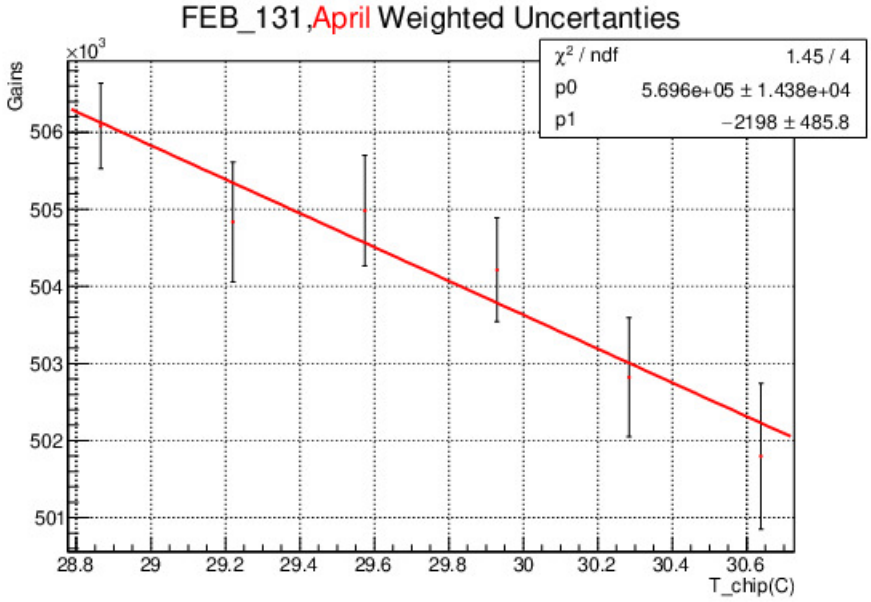

FIGURE A.24: PMT gain (EH configuration) vs T_{chip}.

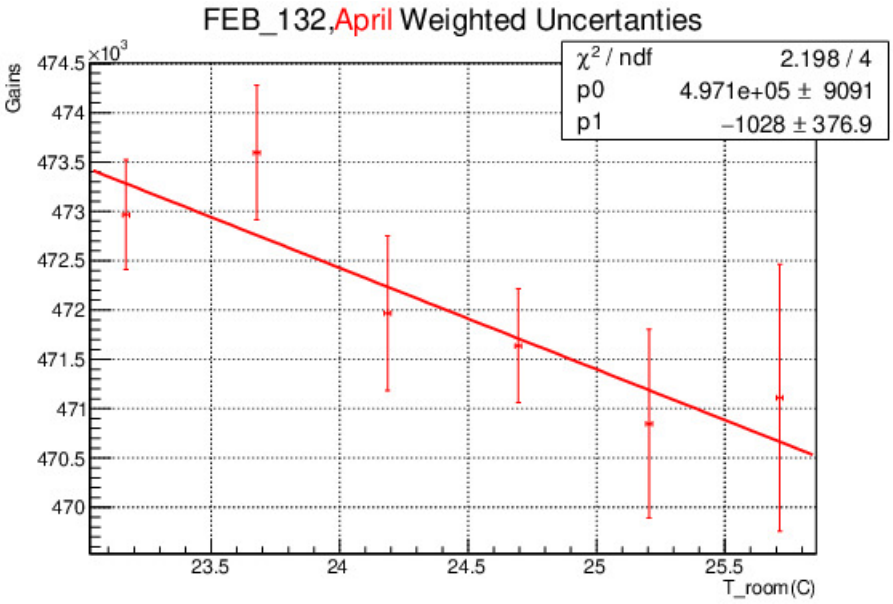

FIGURE A.25: PMT gain (EH configuration) vs T_{room}.

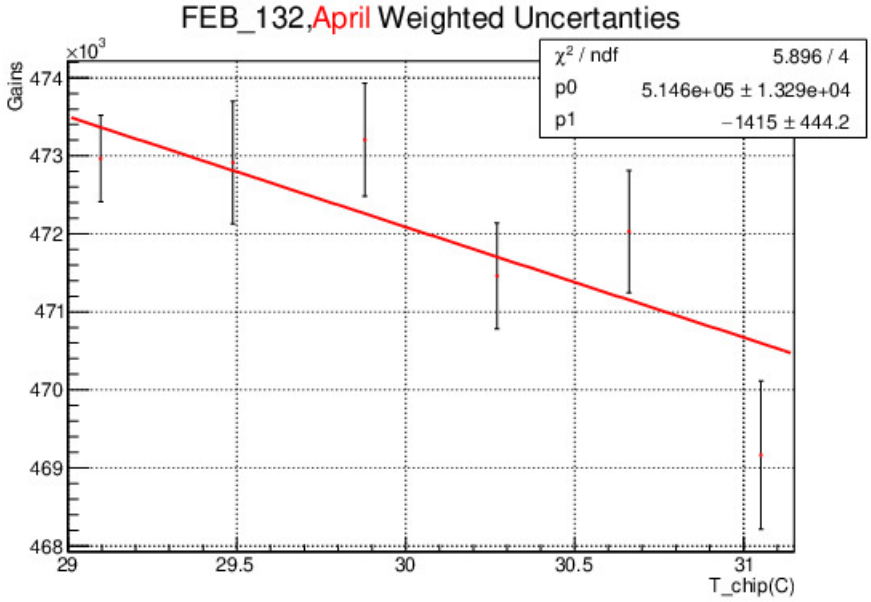

FIGURE A.26: PMT gain (EH configuration) vs T_{chip}.

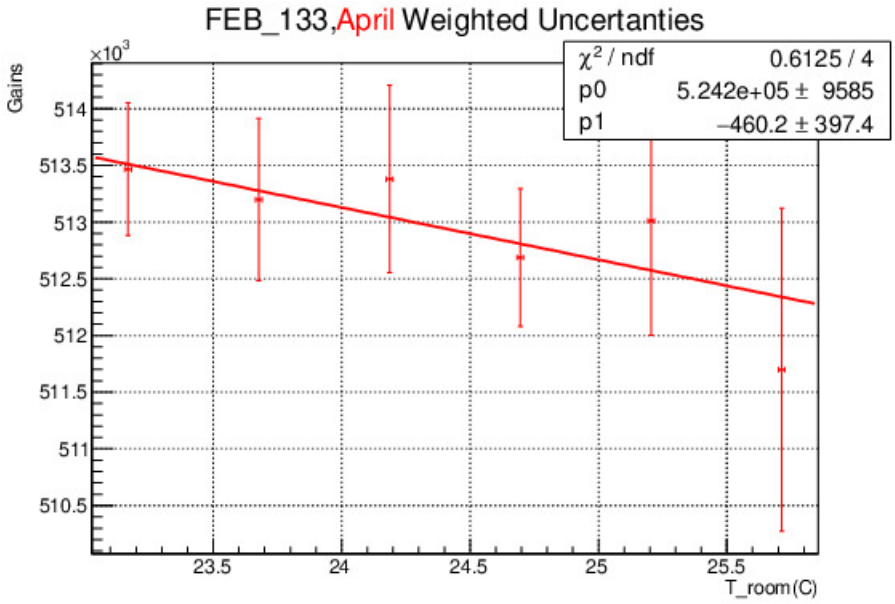

FIGURE A.27: PMT gain (EH configuration) vs T_{room}.

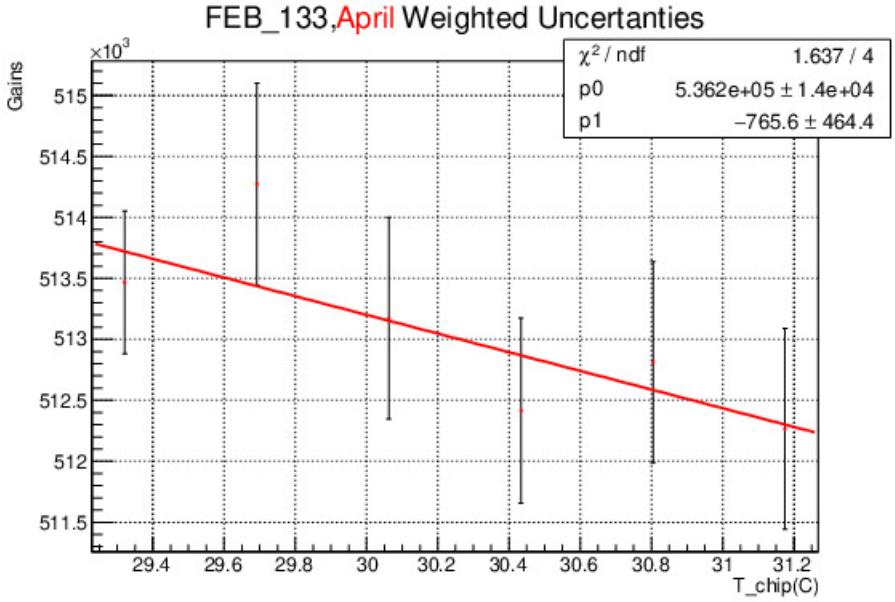

FIGURE A.28: PMT gain (EH configuration) vs T_{chip}.

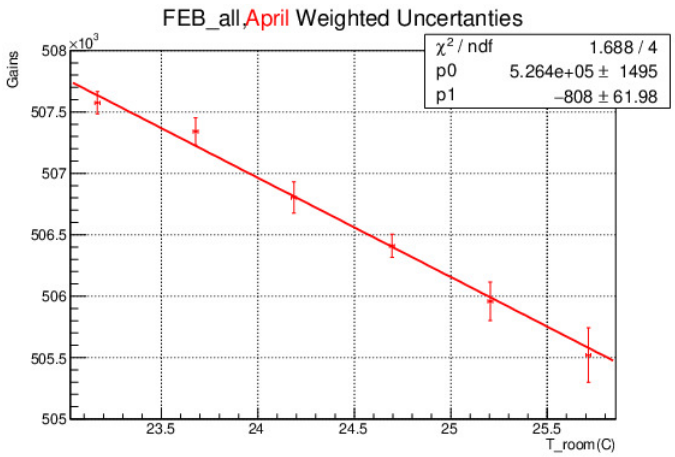

FIGURE A.29: This plot shows the PMT gain (general tendency) as a function of room temperature in April (EH configuration). All PMT tubes.

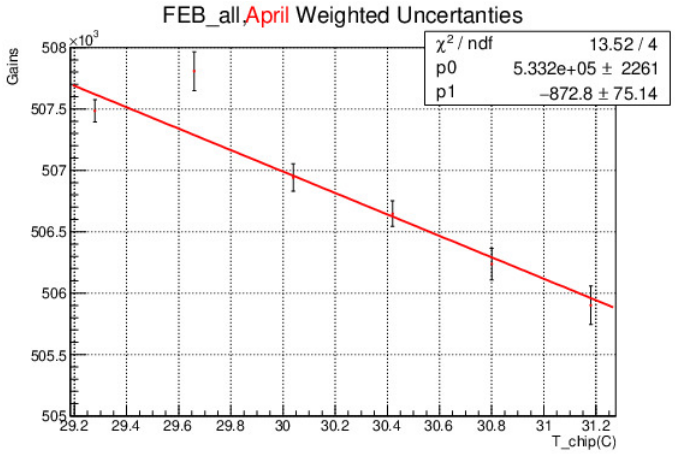

FIGURE A.30: This plot shows the PMT gain (general tendency) as a function of chip temperature in April (EH configuration). All PMT tubes.

A.2 These plots show the PMT gain as a function of room temperature/chip temperature in May-June(SuperHcal Configuration)

Plots from pag. 100 to 139 are plots in detail of each PMT gain (May-July, SuperHcal configuration) for each case (T_{room} and T_{chip}). Plots from pag. 92 to 99 show all the PMT tubes simultaneously to compare their PMT gains one another.

A.2.1 Configuration SuperHcal(May-July, room temperature), PMT tubes from 1 to 20

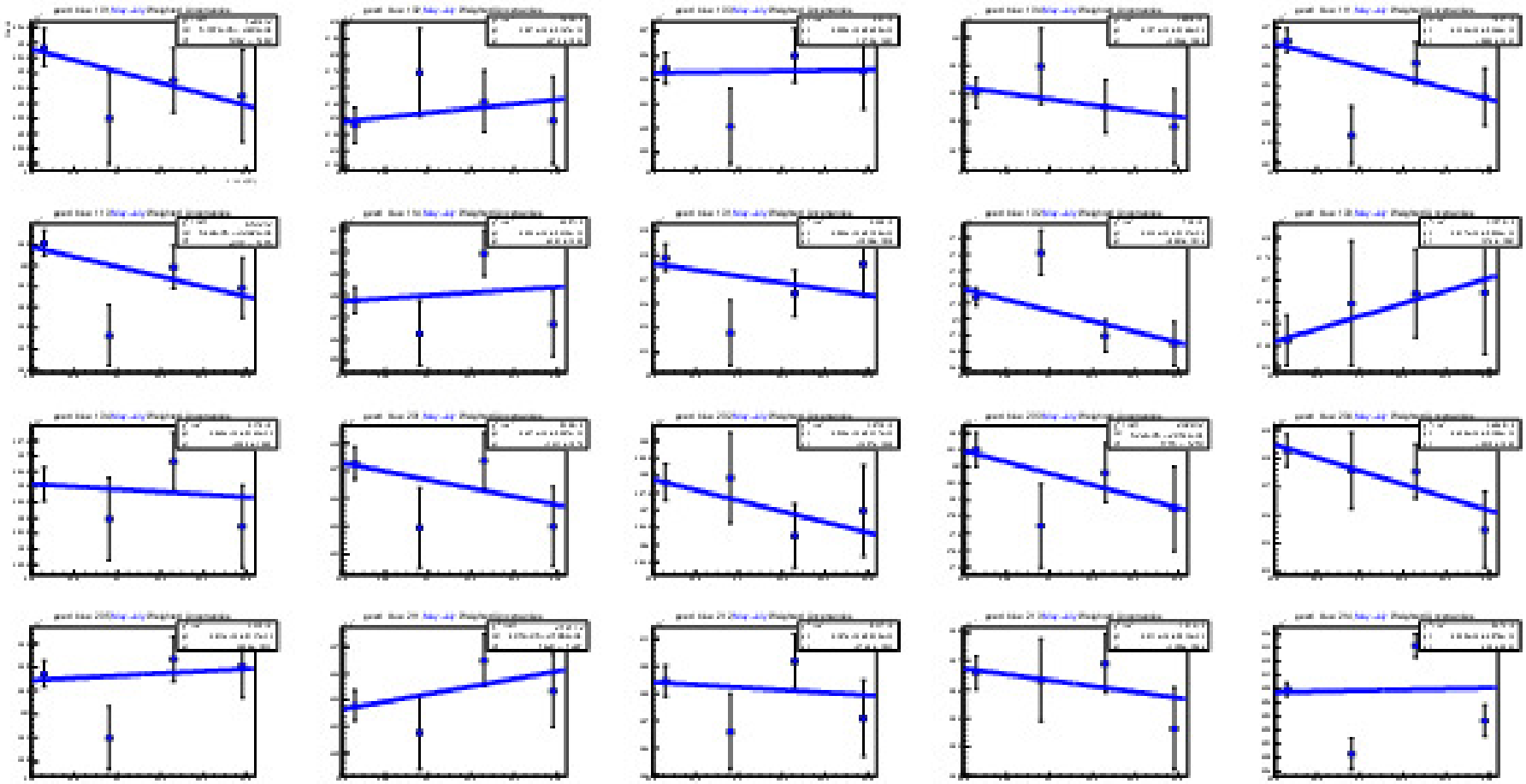

FIGURE A.31: These set of plots show the PMT gain as a function of room temperature in May-July (SuperHcal configuration). PMT tubes from 1 to 20.

A.2.2 Configuration SuperHcal(May-July, room temperature), PMT tubes from 1 to 20 and y axis normalized

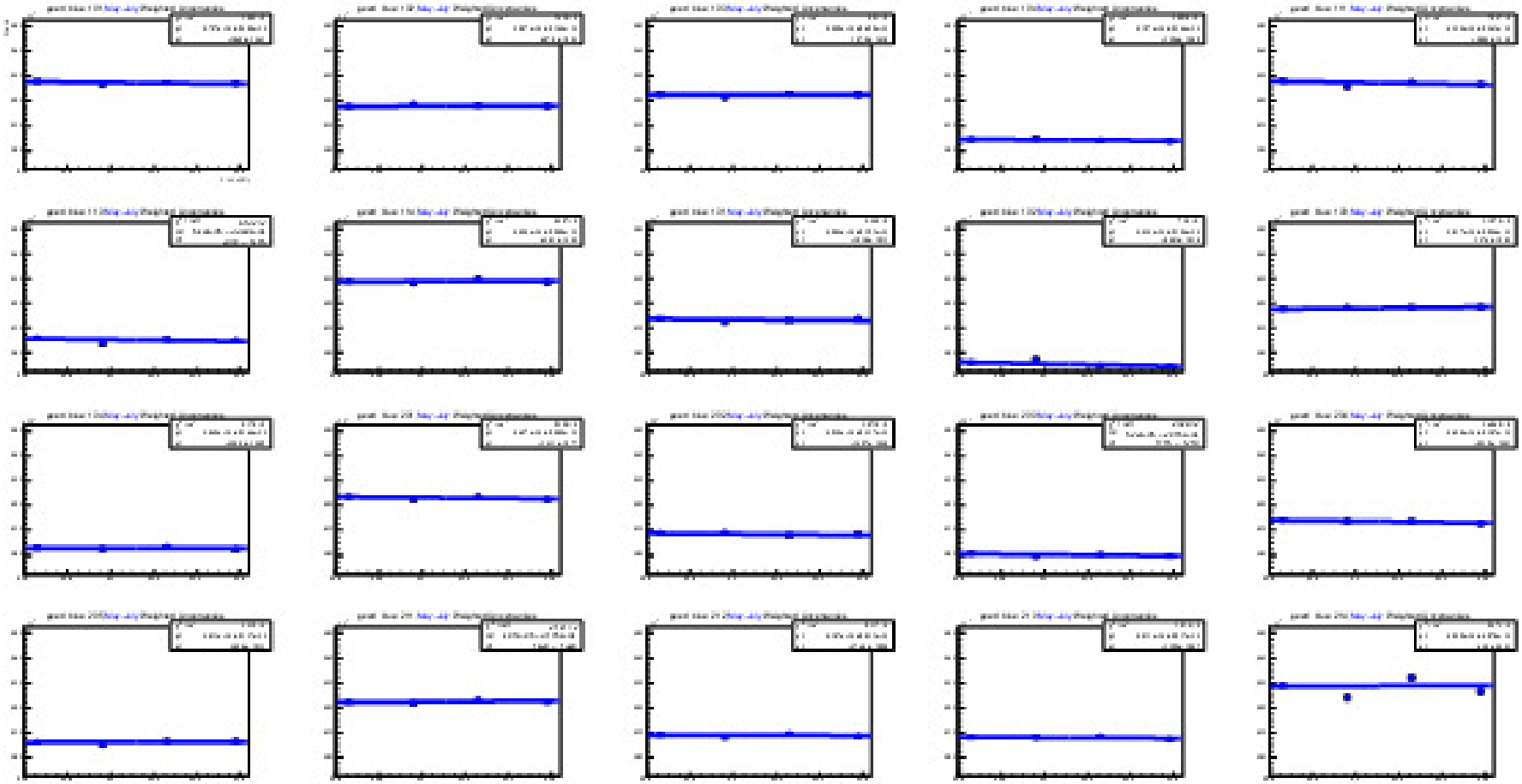

FIGURE A.32: These set of plots (normalized) show the PMT gain as a function of room temperature in May-July (SuperHcal configuration). PMT tubes from 1 to 20.

A.2.3 Configuration SuperHcal(May-July, room temperature), PMT tubes from 21 to 40

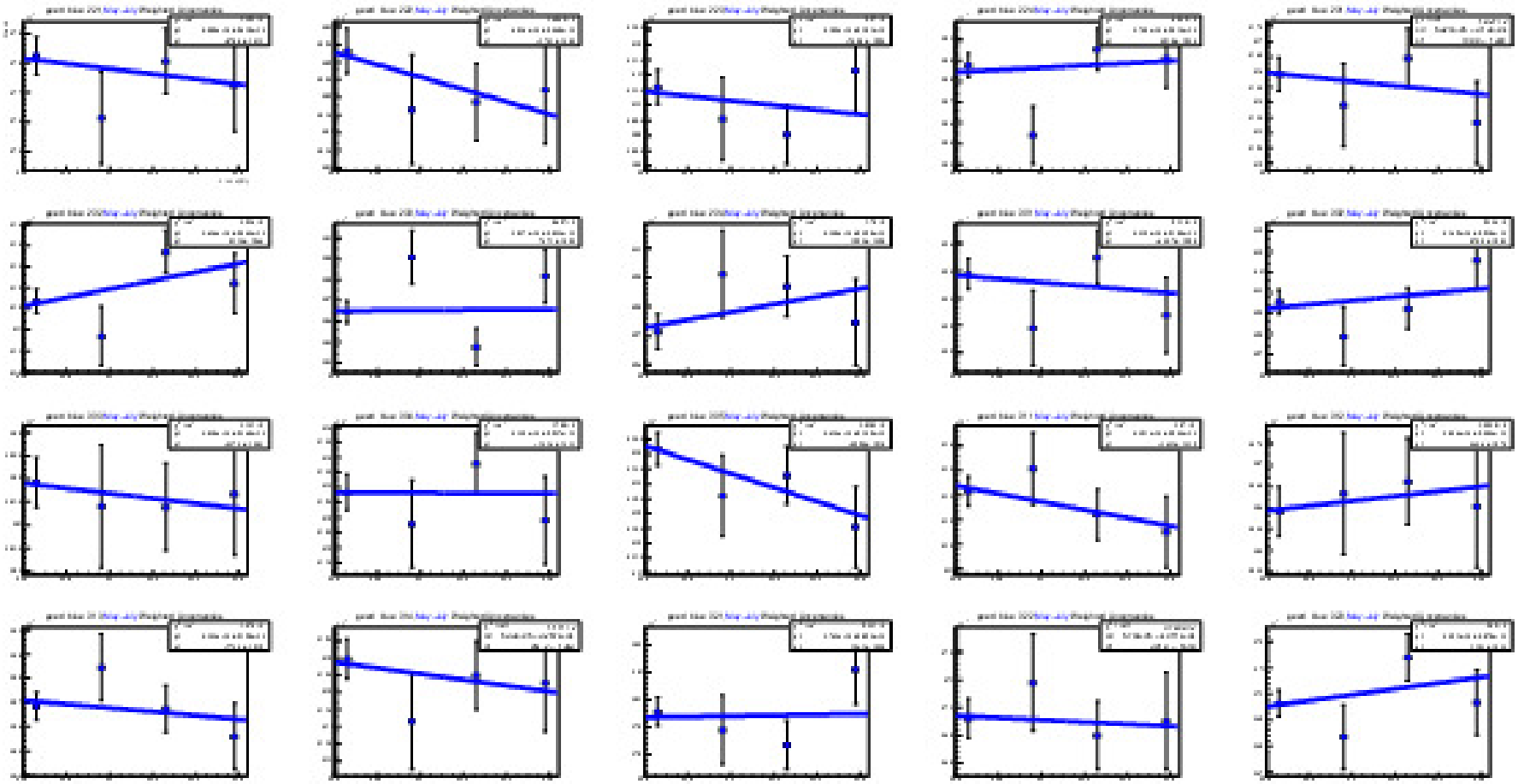

FIGURE A.33: These set of plots show the PMT gain as a function of room temperature in May-July (SuperHcal configuration). PMT tubes from 21 to 40.

A.2.4 Configuration SuperHcal(May-July, room temperature), PMT tubes from 21 to 40 and y axis normalized

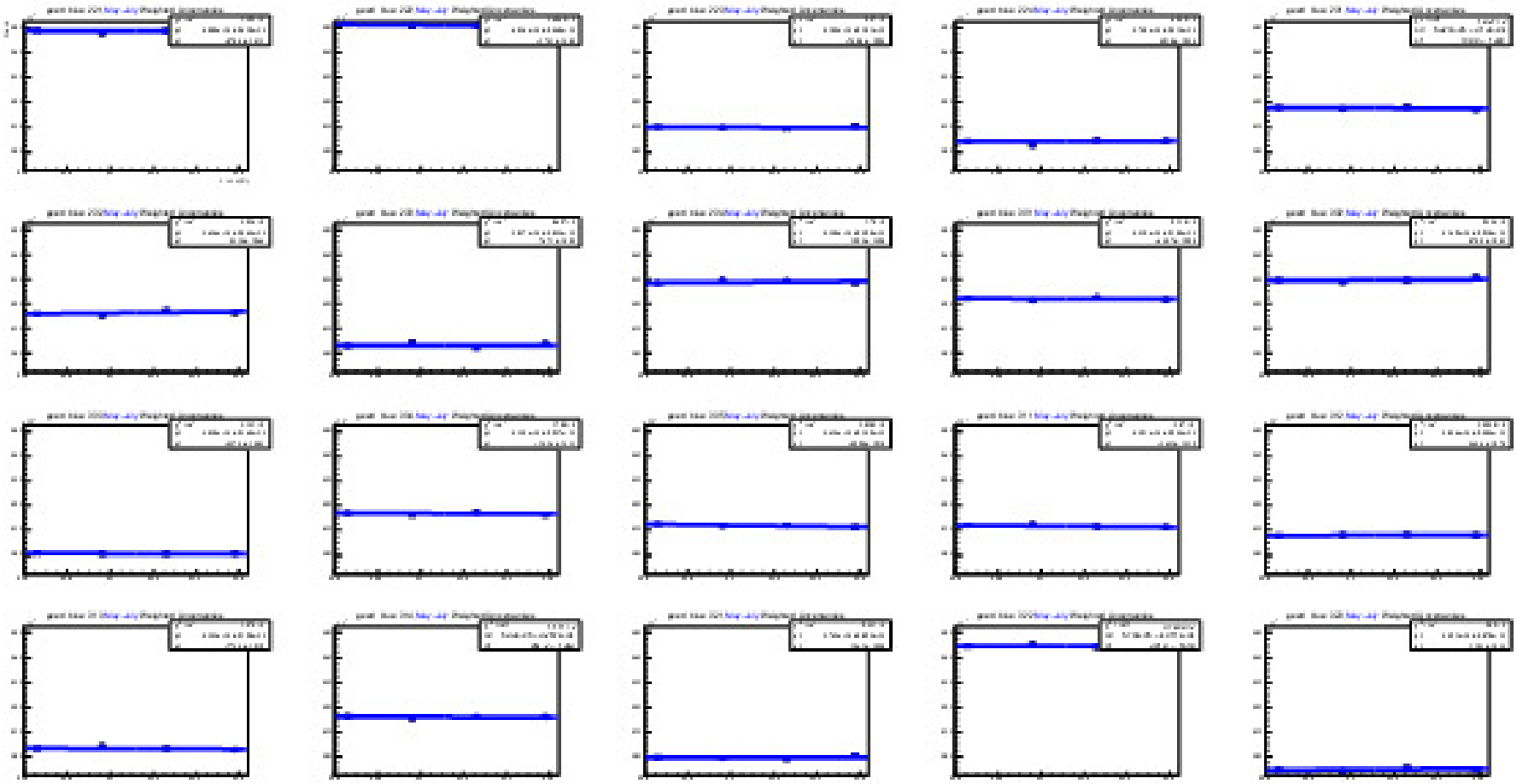

FIGURE A.34: These set of plots (normalized) show the PMT gain as a function of room temperature in May-July (SuperHcal configuration). PMT tubes from 21 to 40.

A.2.5 Configuration SuperHcal(May-July, chip temperature), PMT tubes from 1 to 20

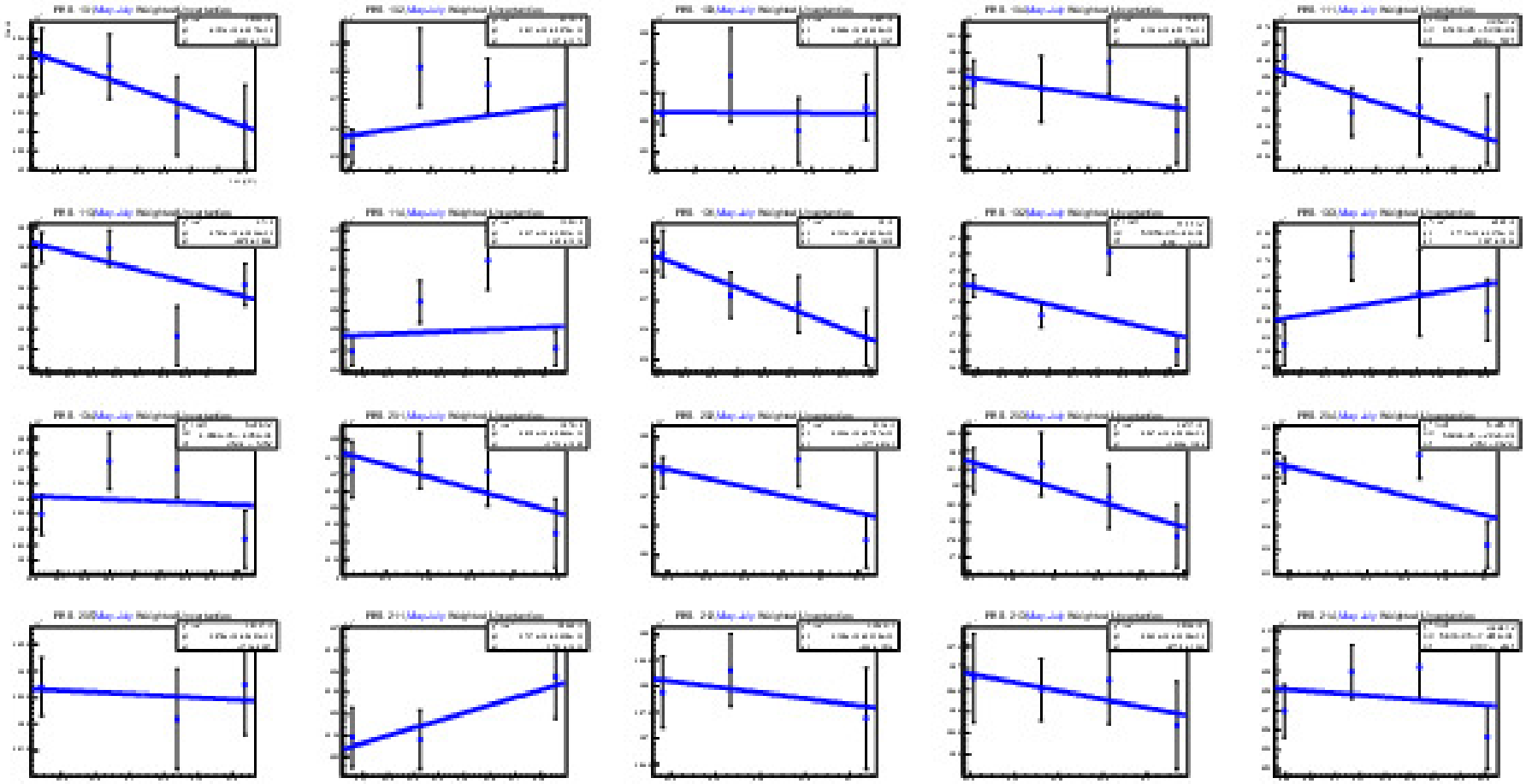

FIGURE A.35: These set of plots show the PMT gain as a function of chip temperature in May-July (SuperHcal configuration). PMT tubes from 1 to 20.

A.2.6 Configuration SuperHcal(May-July, chip temperature), PMT tubes from 1 to 20 and y axis normalized

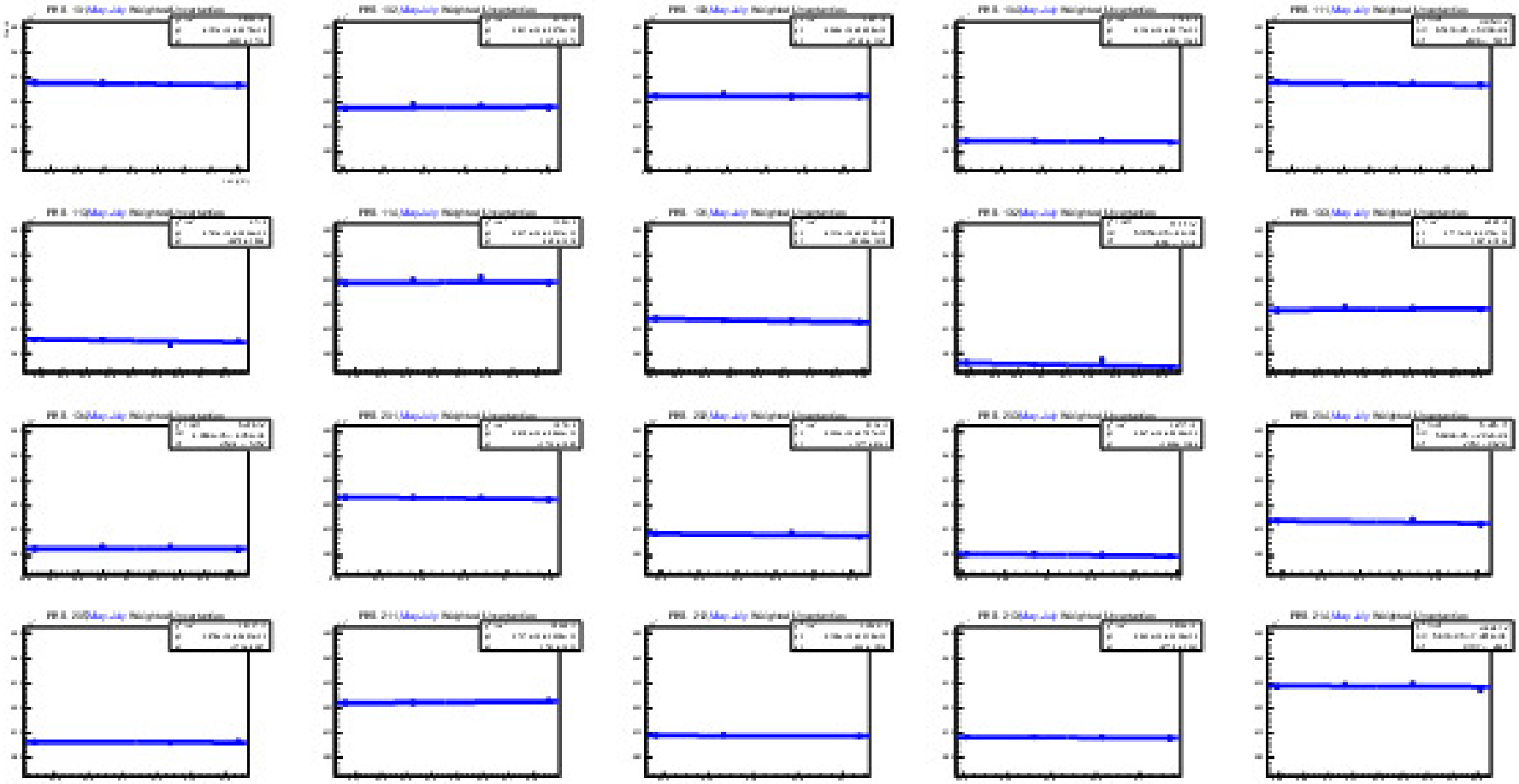

FIGURE A.36: These set of plots (normalized) show the PMT gain as a function of chip temperature in May-July (SuperHcal configuration). PMT tubes from 1 to 20.

A.2.7 Configuration SuperHcal(May-July, chip temperature), PMT tubes from 21 to 40

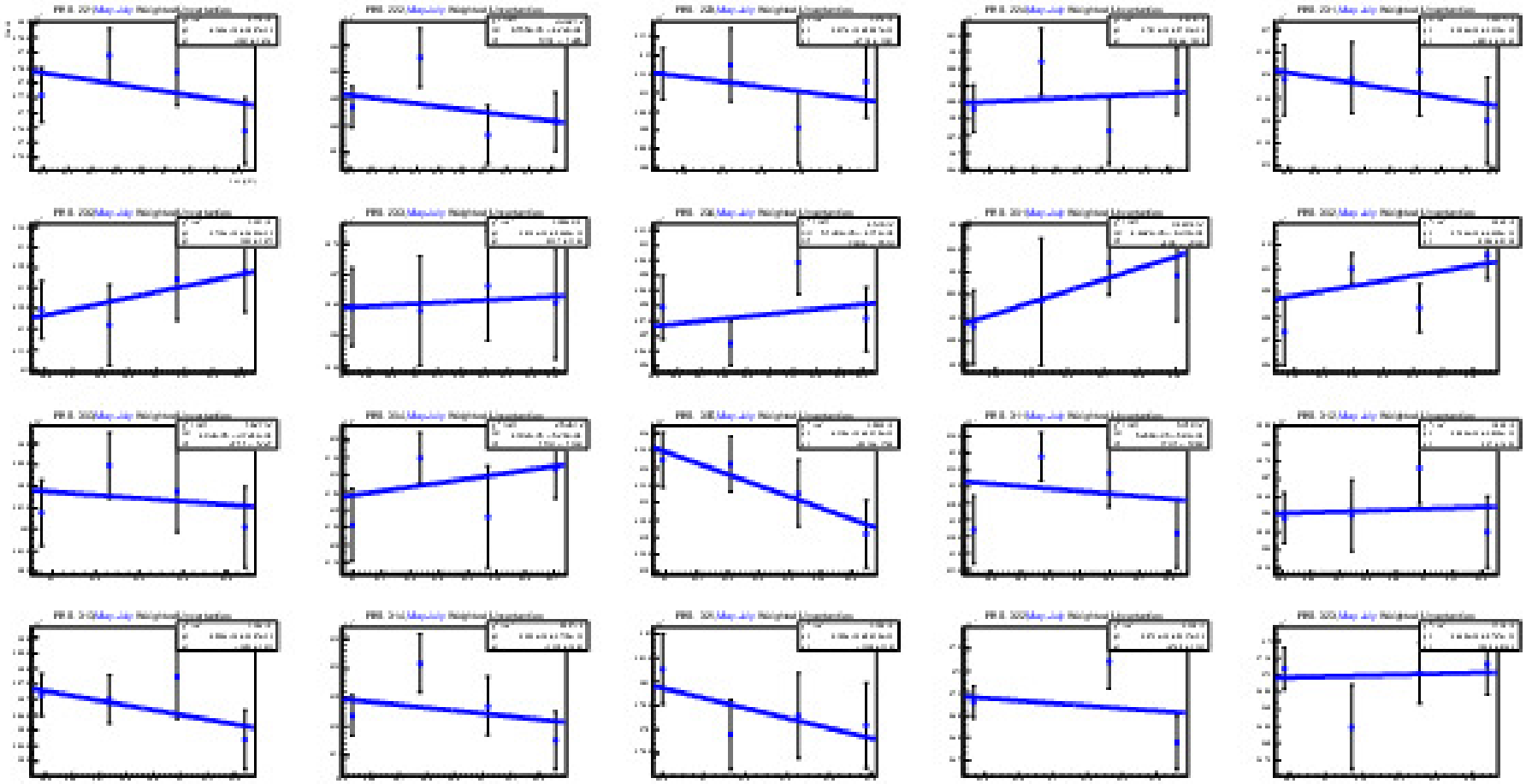

FIGURE A.37: These set of plots show the PMT gain as a function of chip temperature in May-July (SuperHcal configuration). PMT tubes from 21 to 40.

A.2.8 Configuration SuperHcal(May-July, chip temperature), PMT tubes from 21 to 40 and y axis normalized

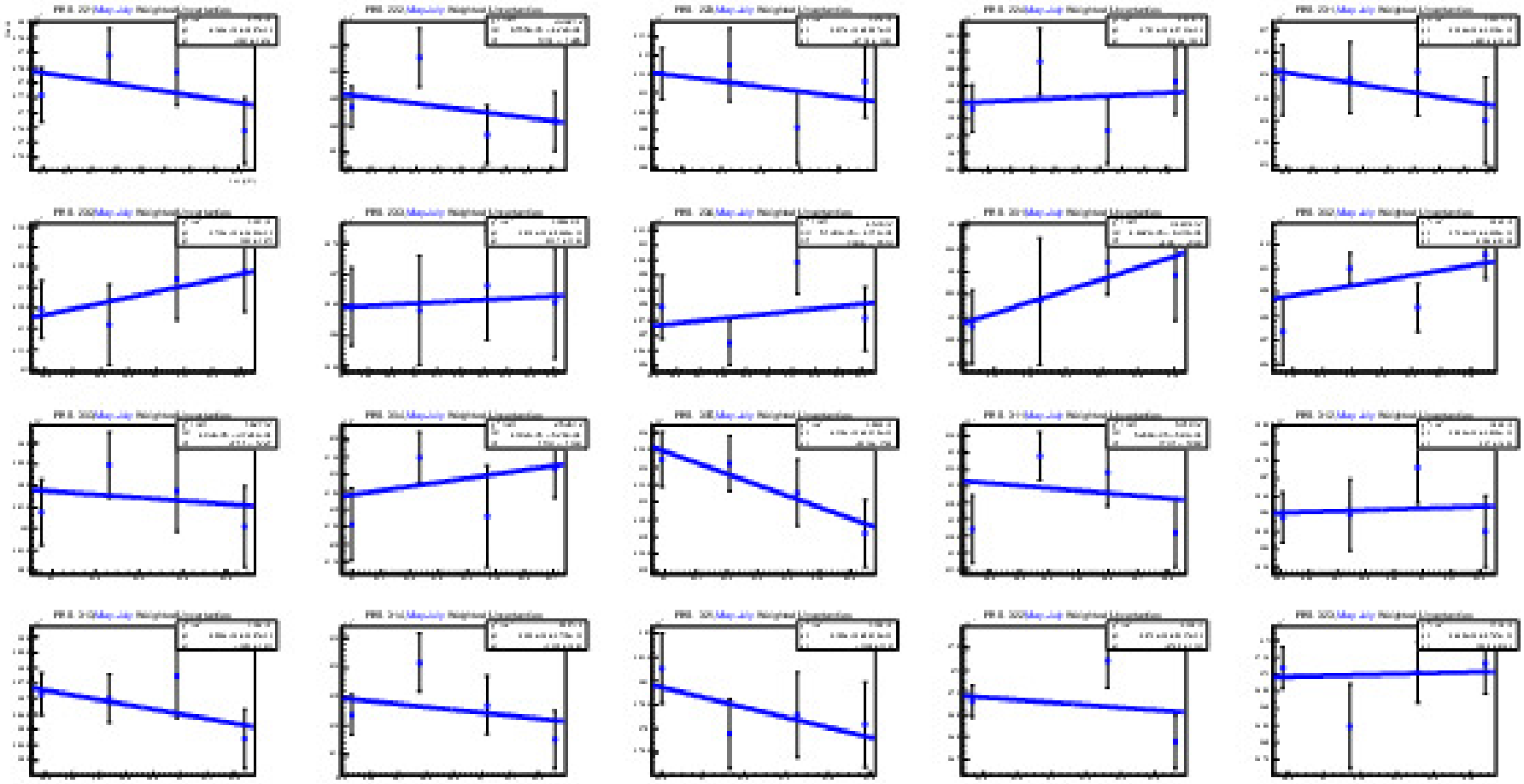

FIGURE A.38: These set of plots (normalized) show the PMT gain as a function of chip temperature in May-July (SuperHcal configuration). PMT tubes from 21 to 40.

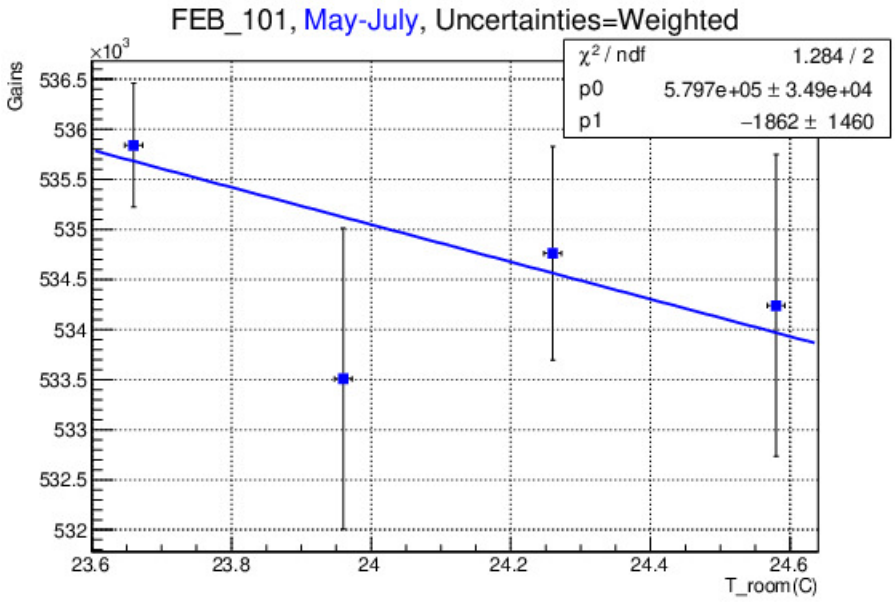

FIGURE A.39: PMT gain (SuperHcal configuration) vs T_{room}.

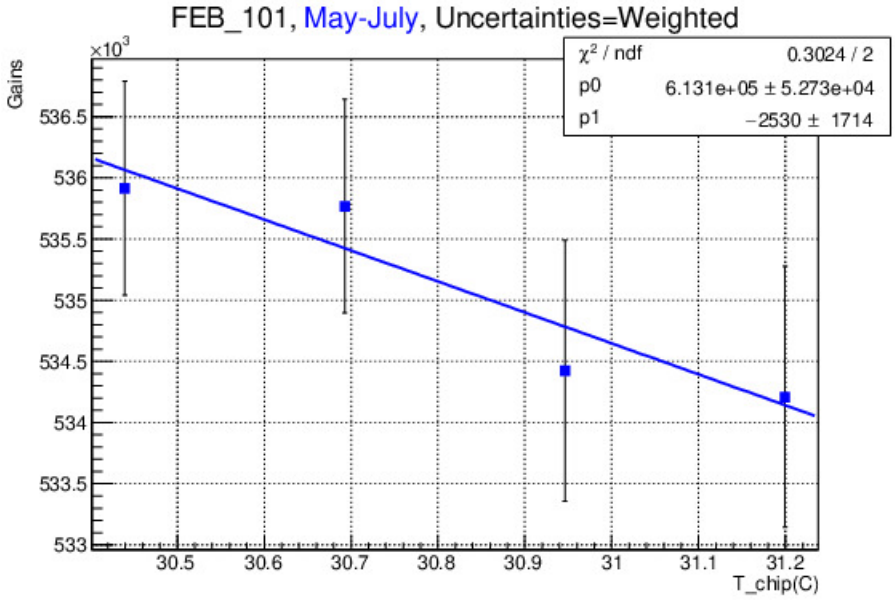

FIGURE A.40: PMT gain (SuperHcal configuration) vs T_{chip}.

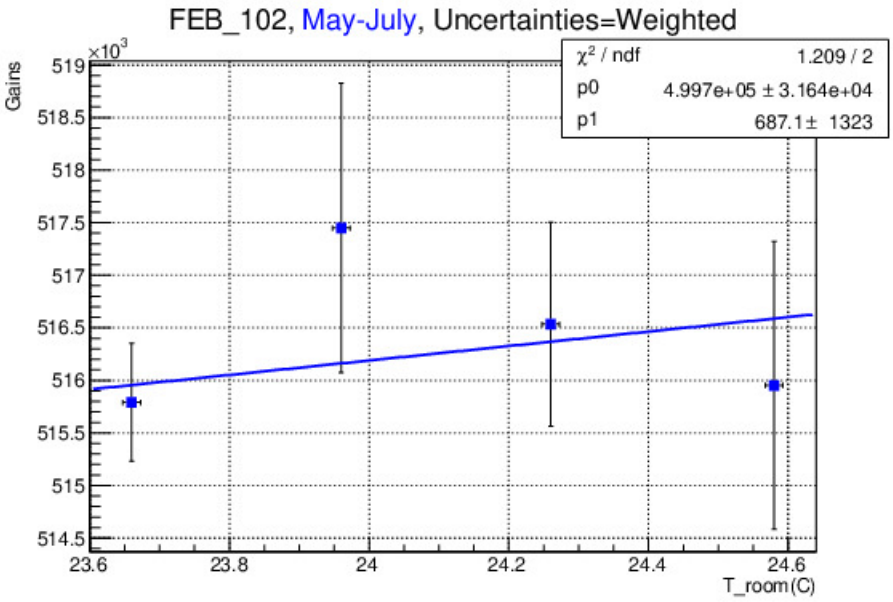

FIGURE A.41: PMT gain (SuperHcal configuration) vs T_{room}.

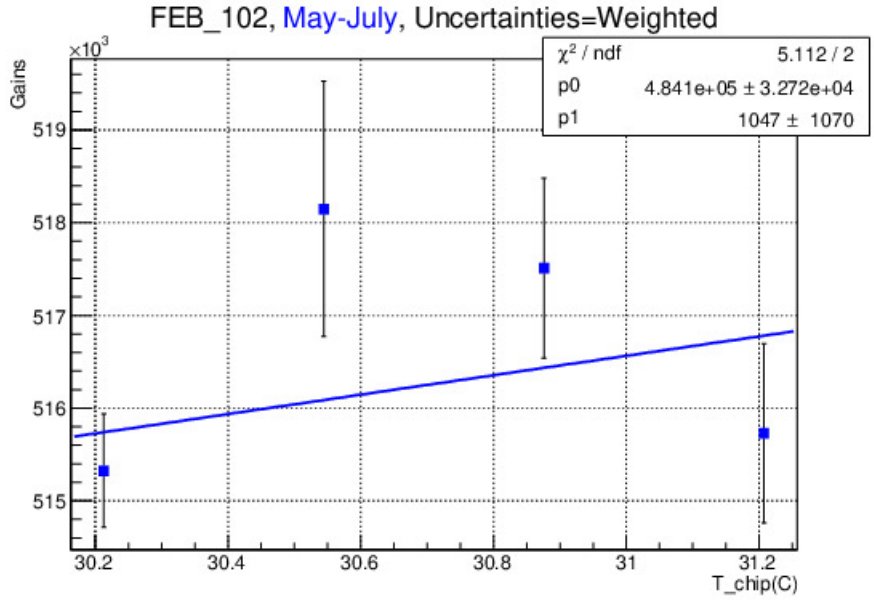

FIGURE A.42: PMT gain (SuperHcal configuration) vs T_{chip}.

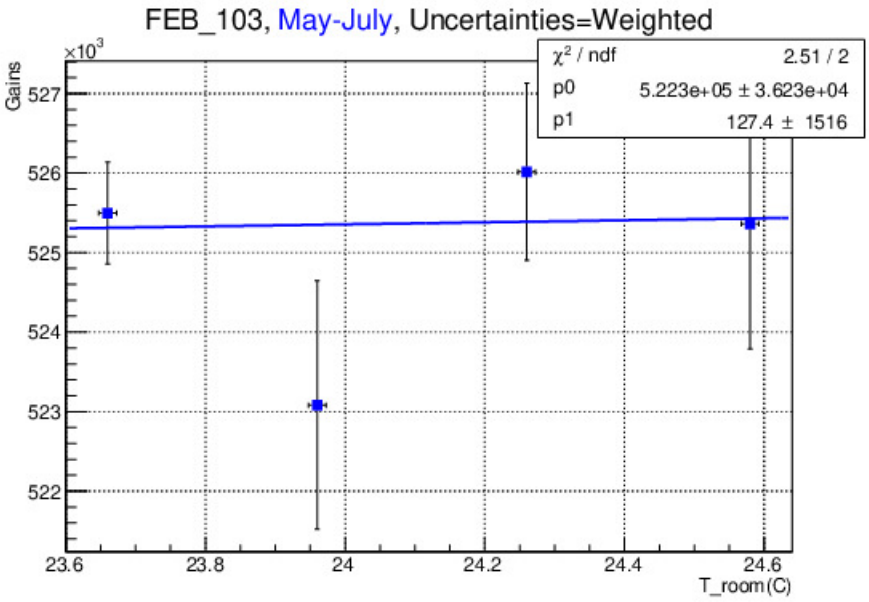

FIGURE A.43: PMT gain (SuperHcal configuration) vs T_{room}.

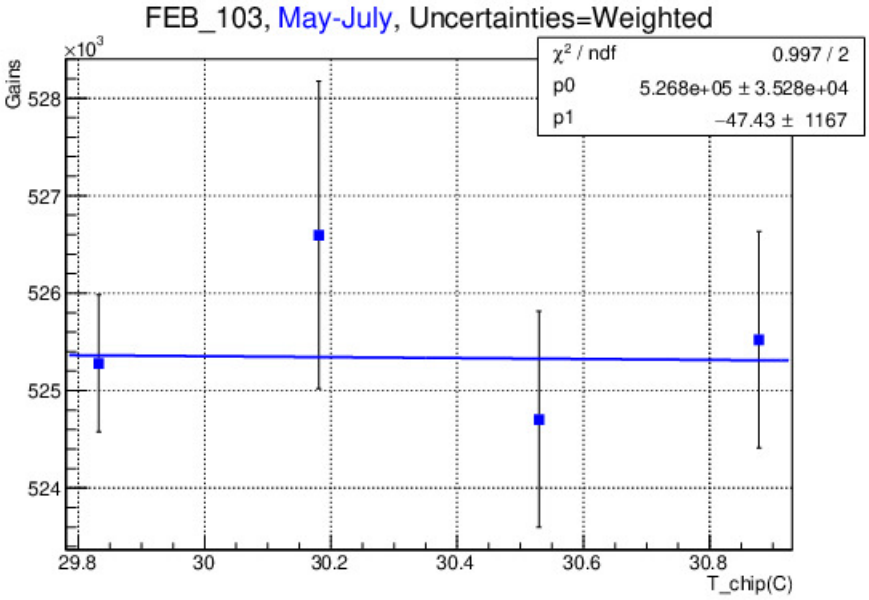

FIGURE A.44: PMT gain (SuperHcal configuration) vs T_{chip}.

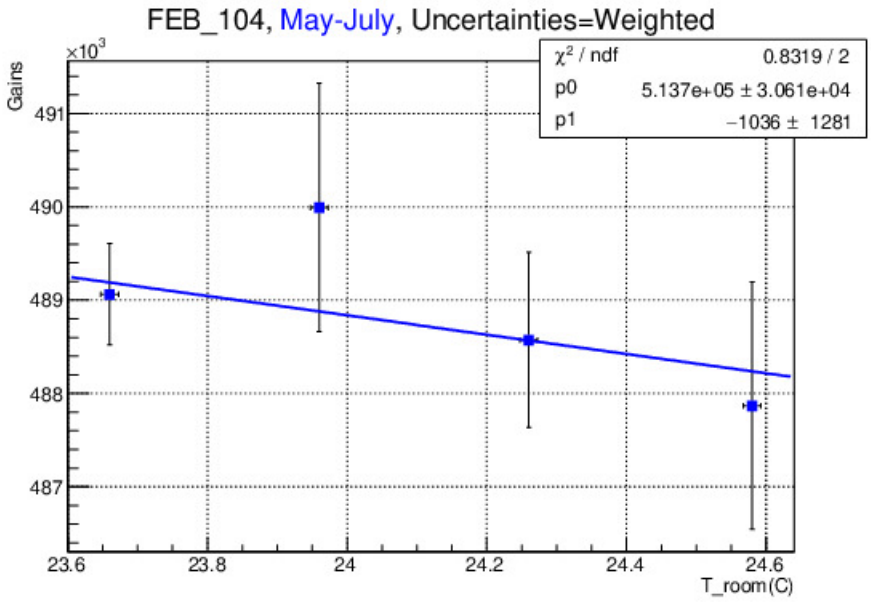

FIGURE A.45: PMT gain (SuperHcal configuration) vs T_{room}.

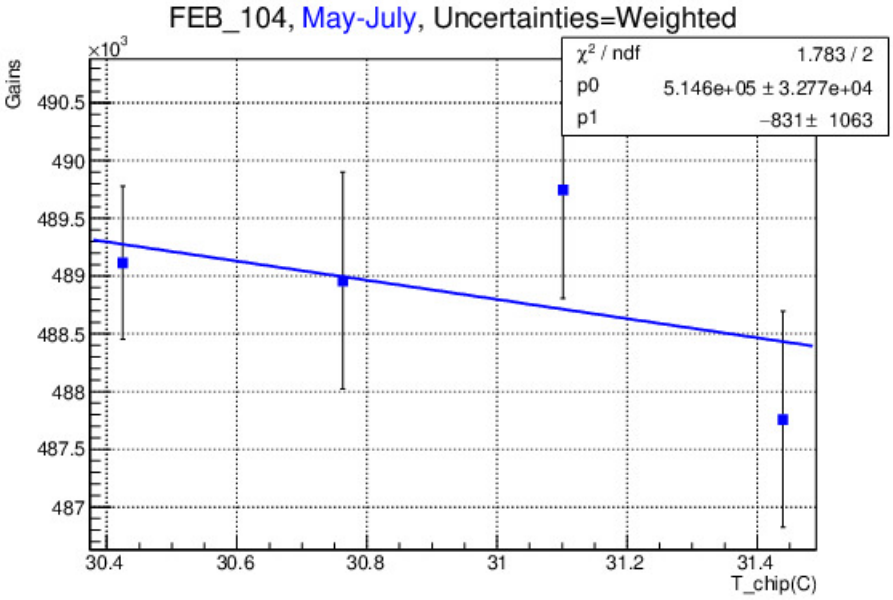

FIGURE A.46: PMT gain (SuperHcal configuration) vs T_{chip}.

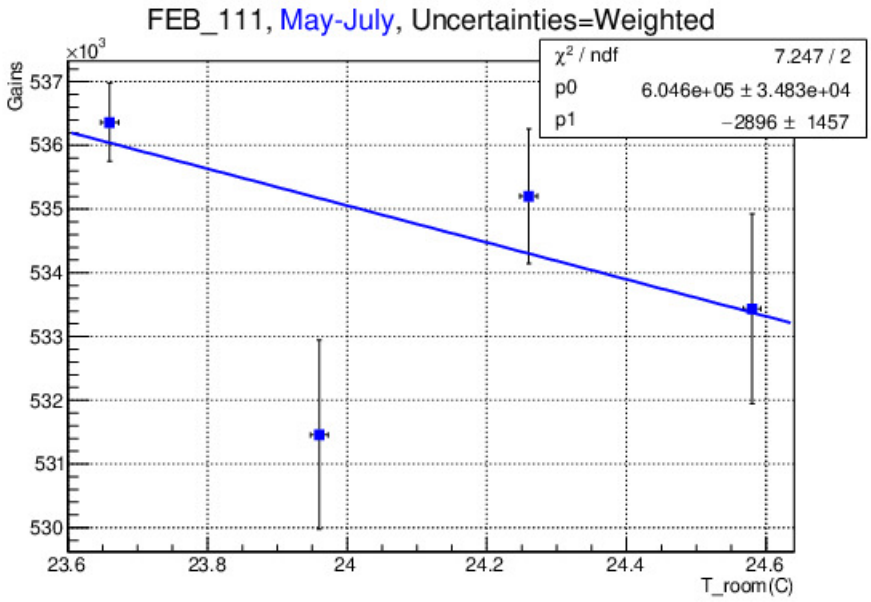

FIGURE A.47: PMT gain (SuperHcal configuration) vs T_{room}.

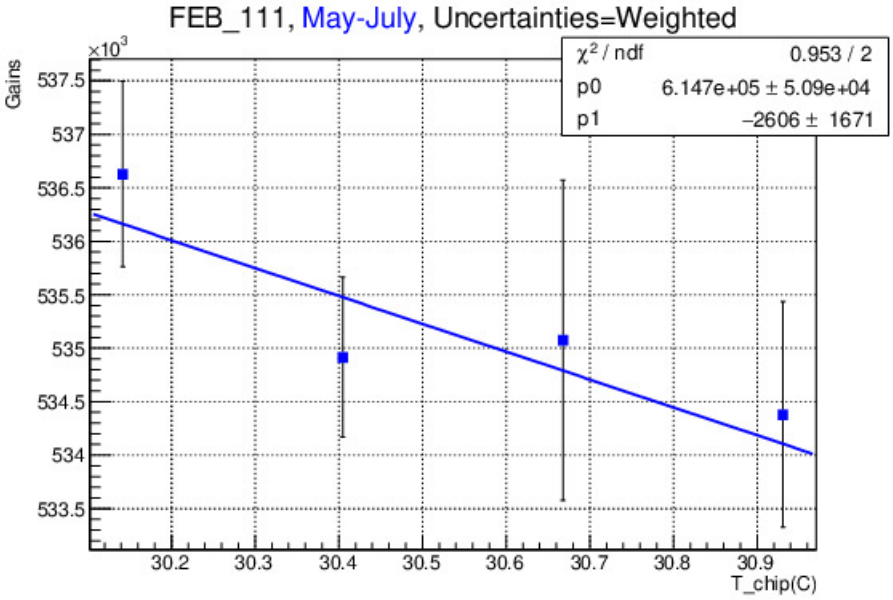

FIGURE A.48: PMT gain (SuperHcal configuration) vs T_{chip}.

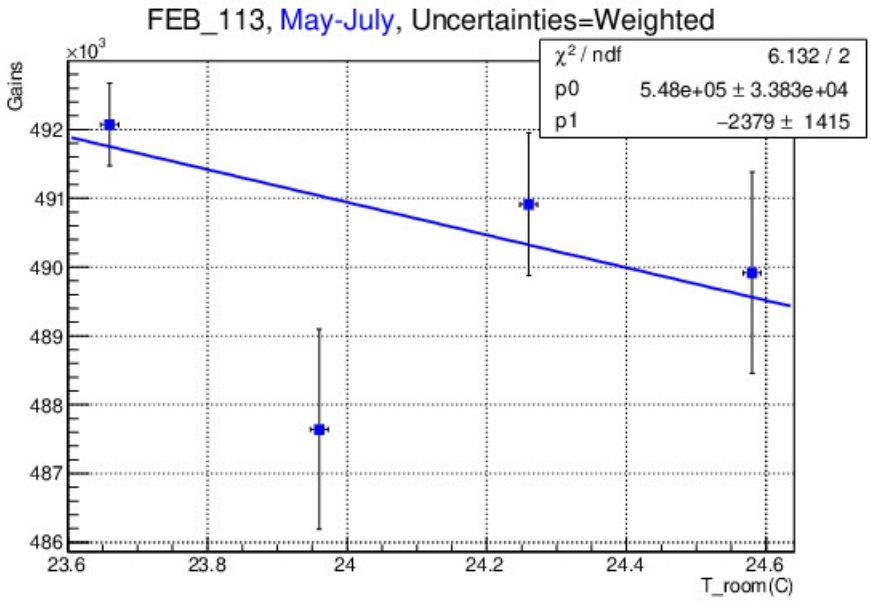

FIGURE A.49: PMT gain (SuperHcal configuration) vs T_{room}.

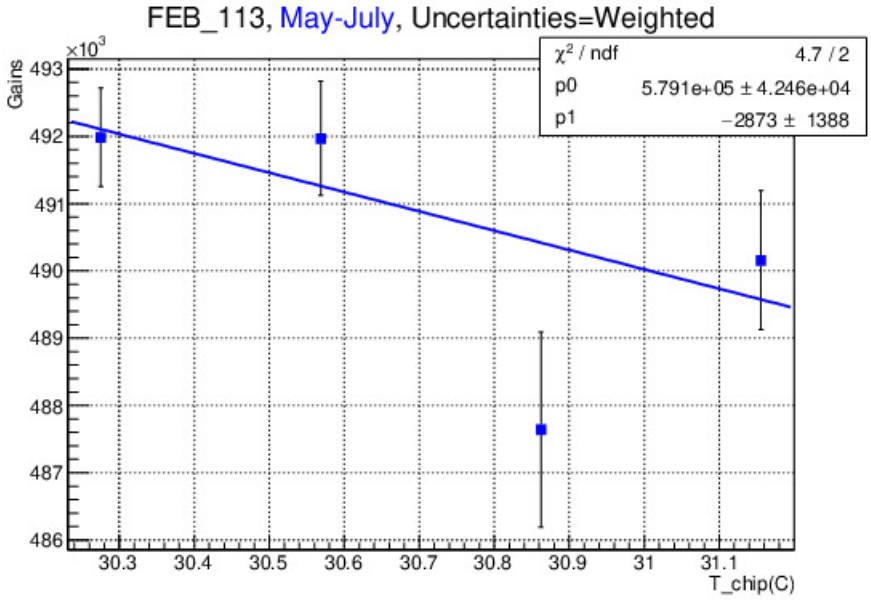

FIGURE A.50: PMT gain (SuperHcal configuration) vs T_{chip}.

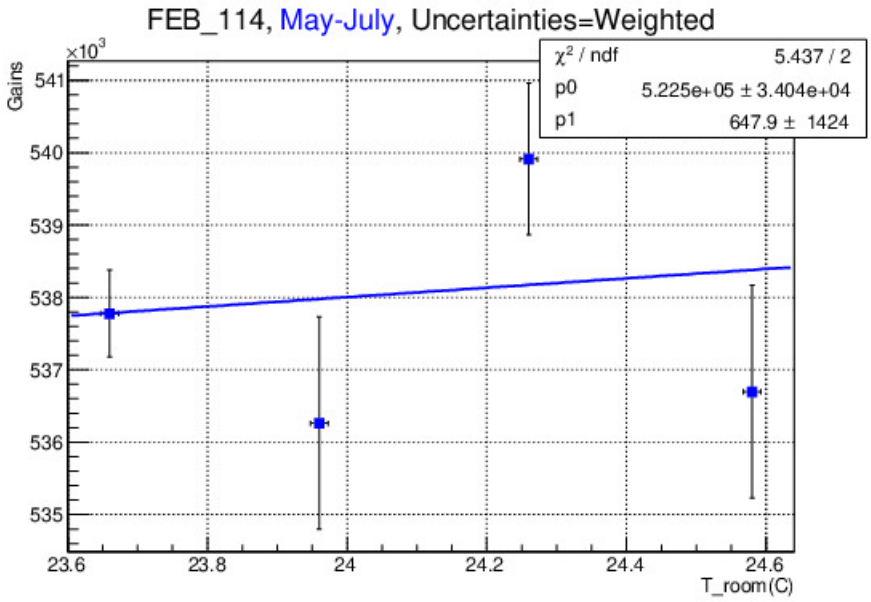

FIGURE A.51: PMT gain (SuperHcal configuration) vs T_{room}.

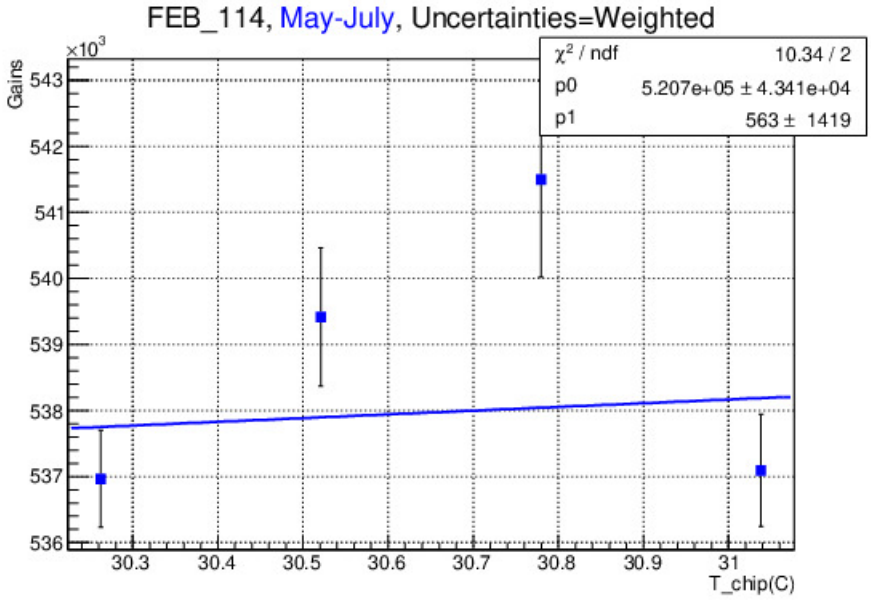

FIGURE A.52: PMT gain (SuperHcal configuration) vs T_{chip}.

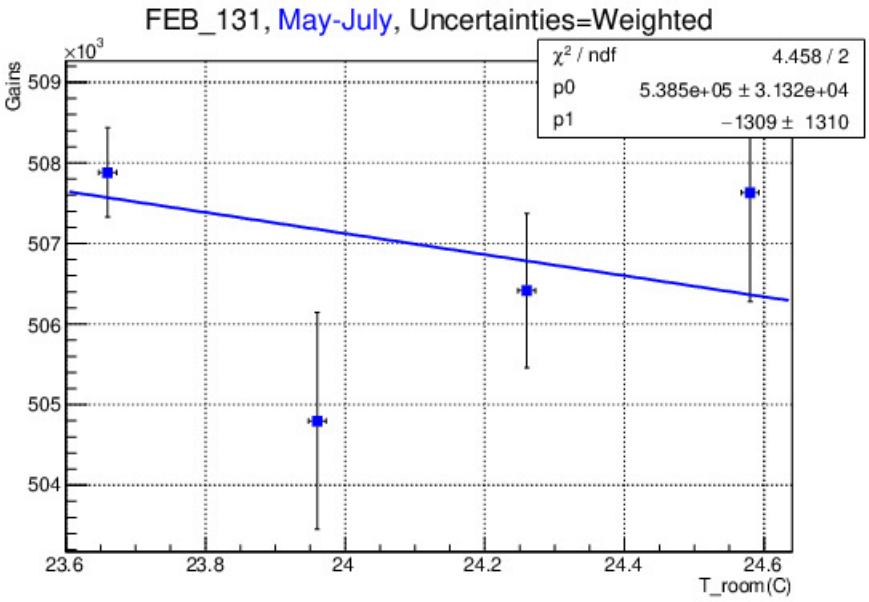

FIGURE A.53: PMT gain (SuperHcal configuration) vs T_{room}.

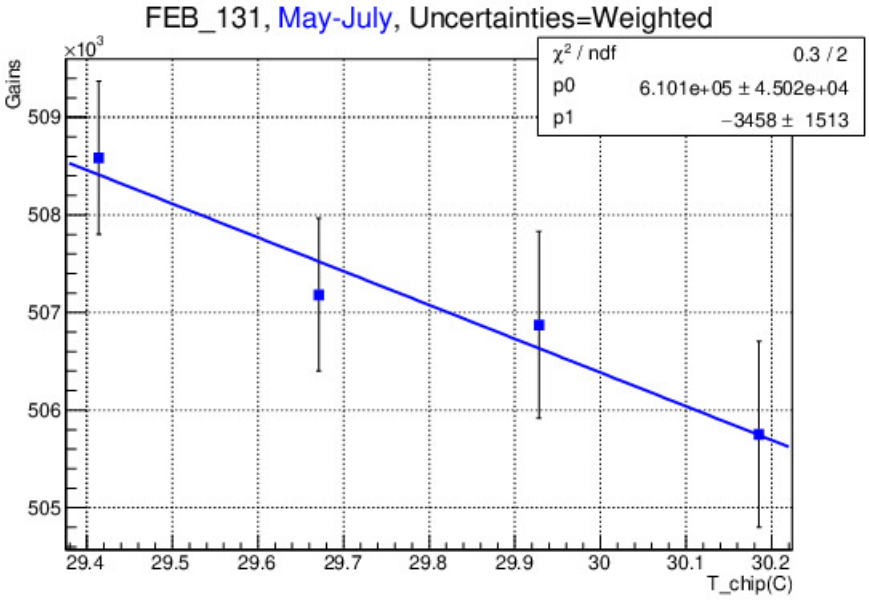

FIGURE A.54: PMT gain (SuperHcal configuration) vs T_{chip}.

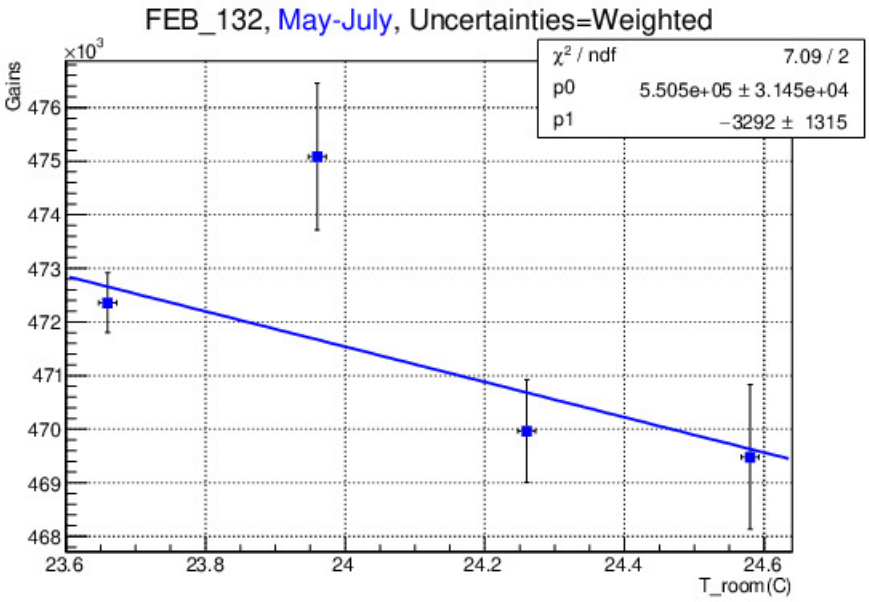

FIGURE A.55: PMT gain (SuperHcal configuration) vs T_{room}.

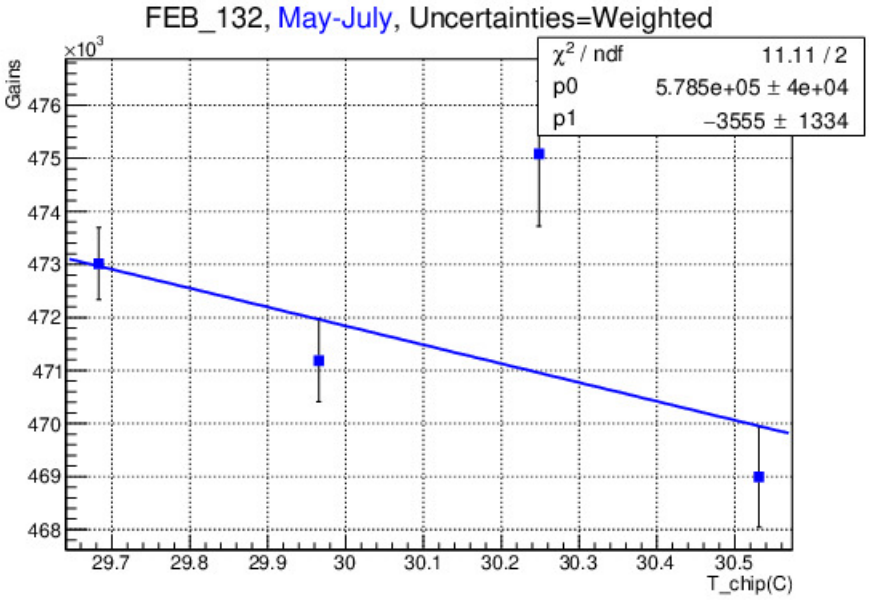

FIGURE A.56: PMT gain (SuperHcal configuration) vs T_{chip}.

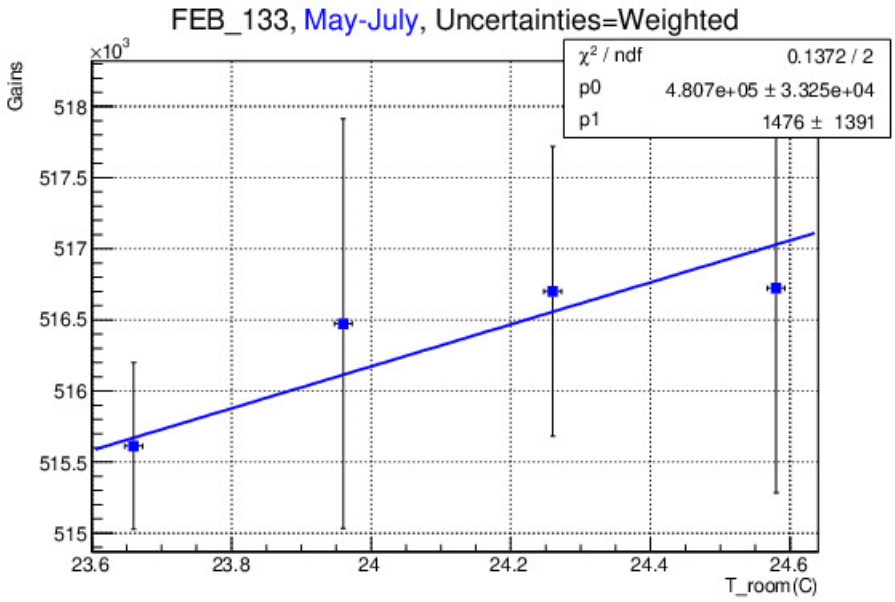

FIGURE A.57: PMT gain (SuperHcal configuration) vs T_{room}.

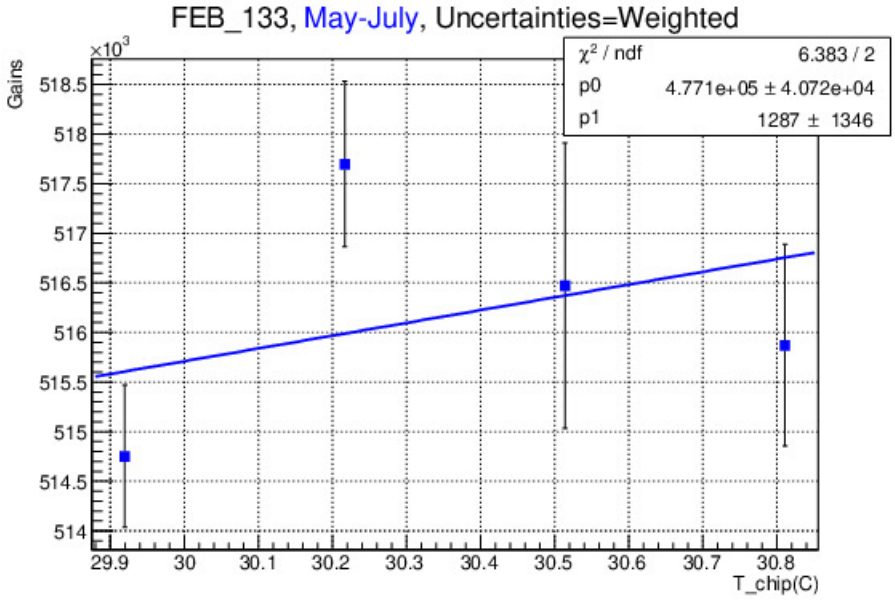

FIGURE A.58: PMT gain (SuperHcal configuration) vs T_{chip}.

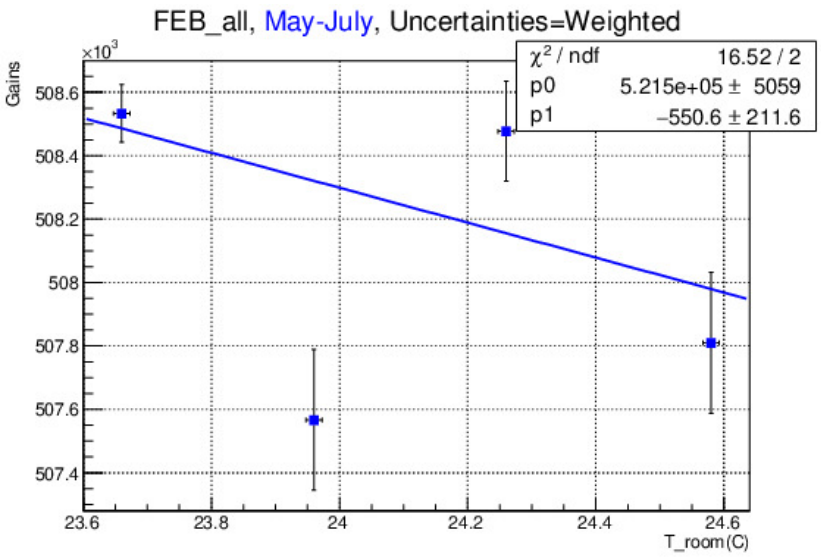

FIGURE A.59: This plot shows the PMT gain (general tendency) as a function of T_{room} in May-July (SuperHcal configuration). All PMT tubes.

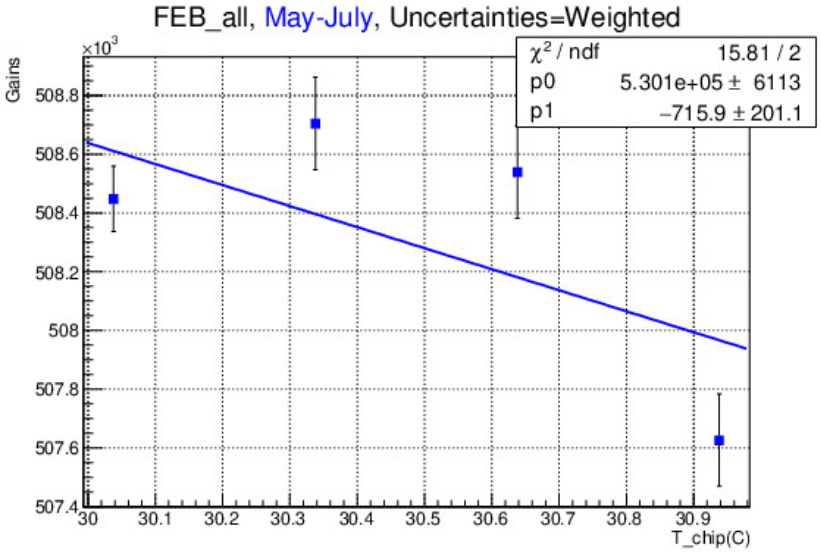

FIGURE A.60: This plot shows the PMT gain (general tendency) as a function of T_{chip} in May-July (SuperHcal configuration). All PMT tubes.

Appendix B

Chip Temperature for each FEB

Temperature recorded from April 6, 2015 17 : 23 : 20 to July 1, 2015 12 : 55 : 24

Here are shown the T_{chip} for the first 10 tubes only, to visualize the full T_{chip} set of histograms for the 40 PMT tubes, please see (pag. $143 - 183$):
https://drive.google.com/open?id=1IJ41$_{I}geI0FiGaSyTncecs4doDxaXuRp$

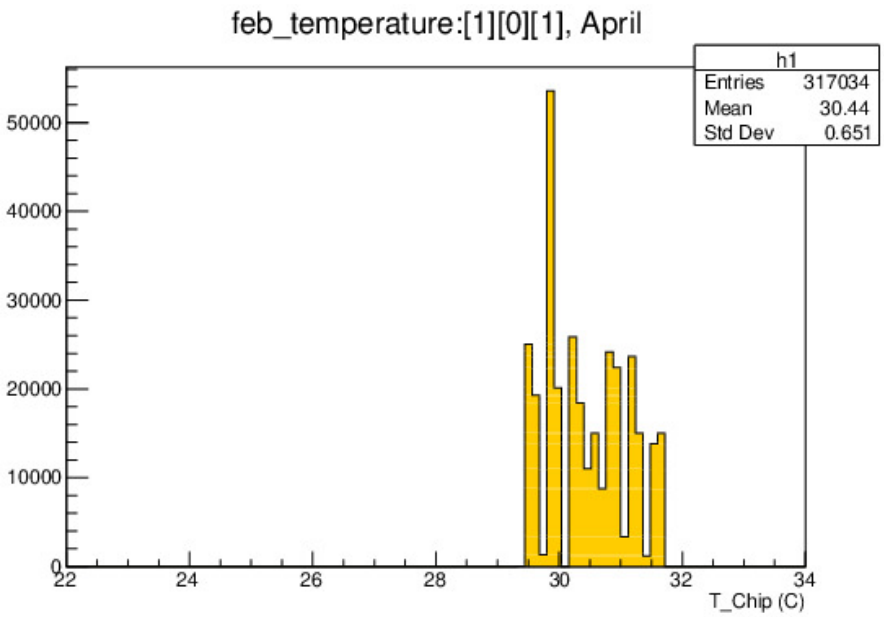

FIGURE B.1: Chip Temperature FEB 101, April

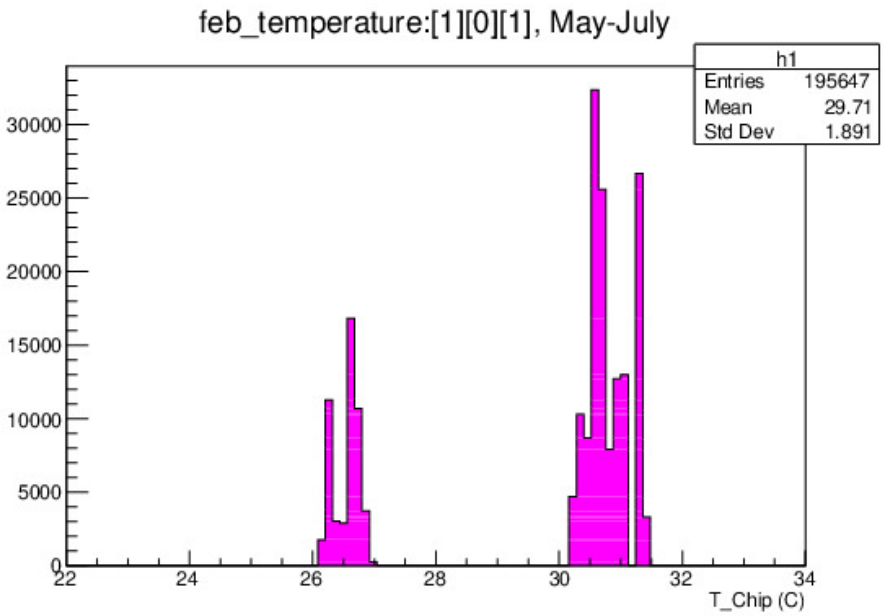

FIGURE B.2: Chip Temperature FEB 101, May-July

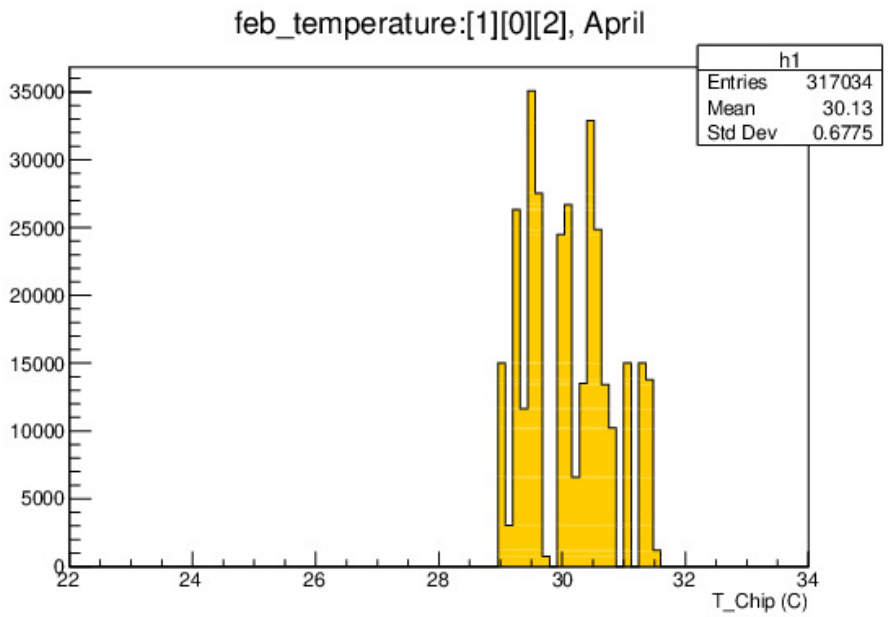

FIGURE B.3: Chip Temperature FEB 102, April

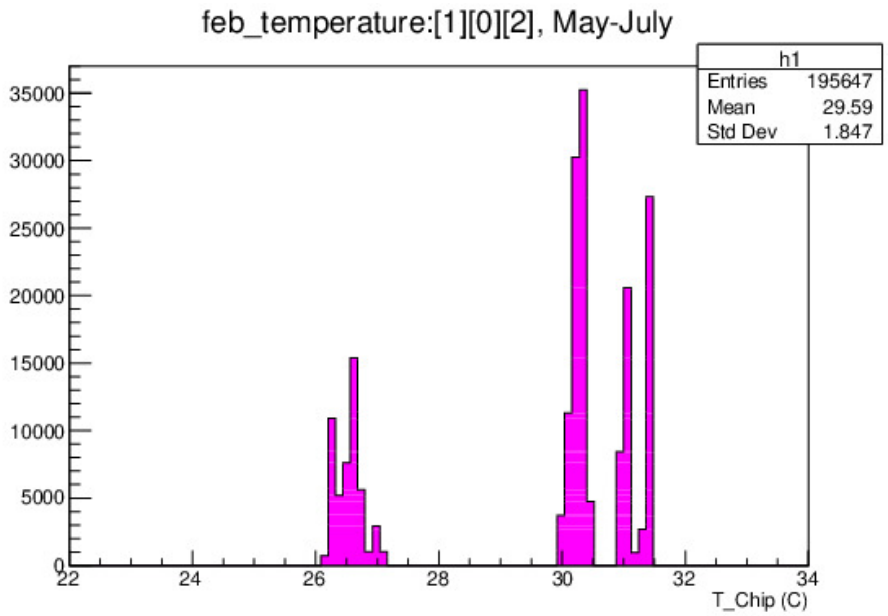

FIGURE B.4: Chip Temperature FEB 102, May-July

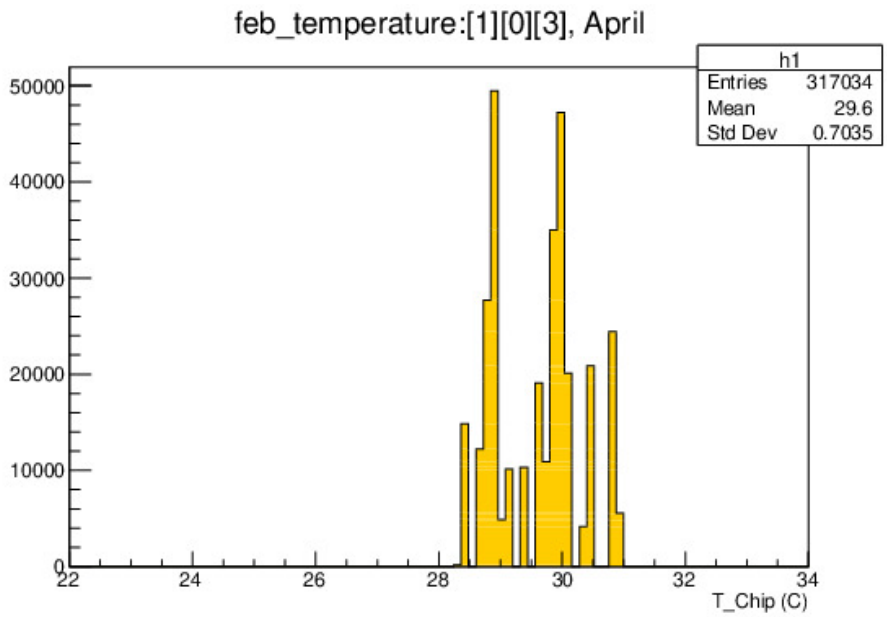

FIGURE B.5: Chip Temperature FEB 103, April

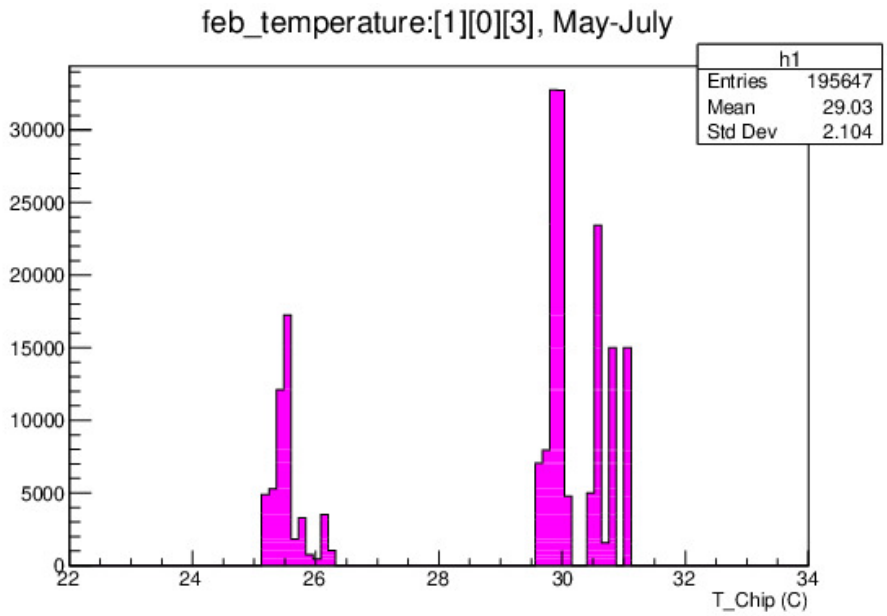

FIGURE B.6: Chip Temperature FEB 103, May-July

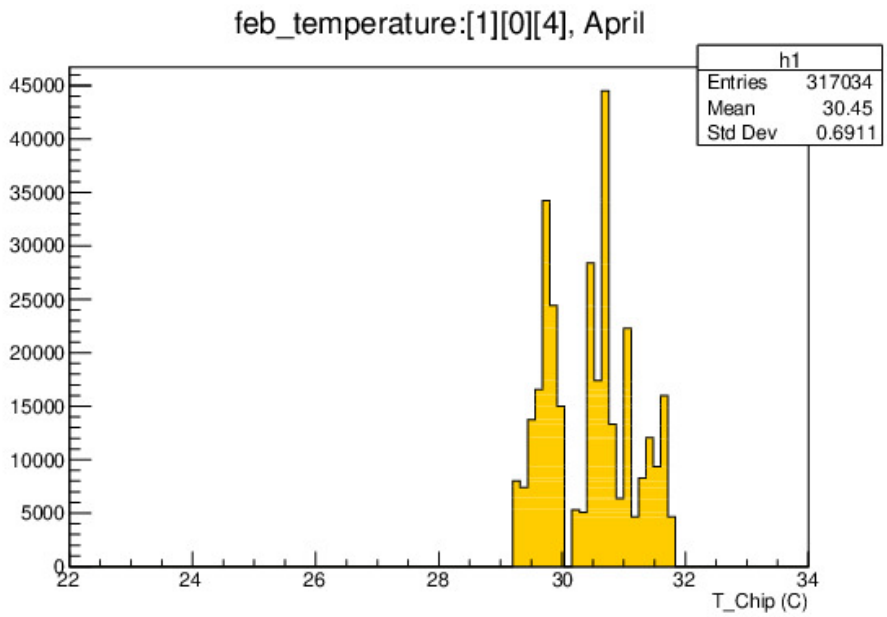

FIGURE B.7: Chip Temperature FEB 104, April

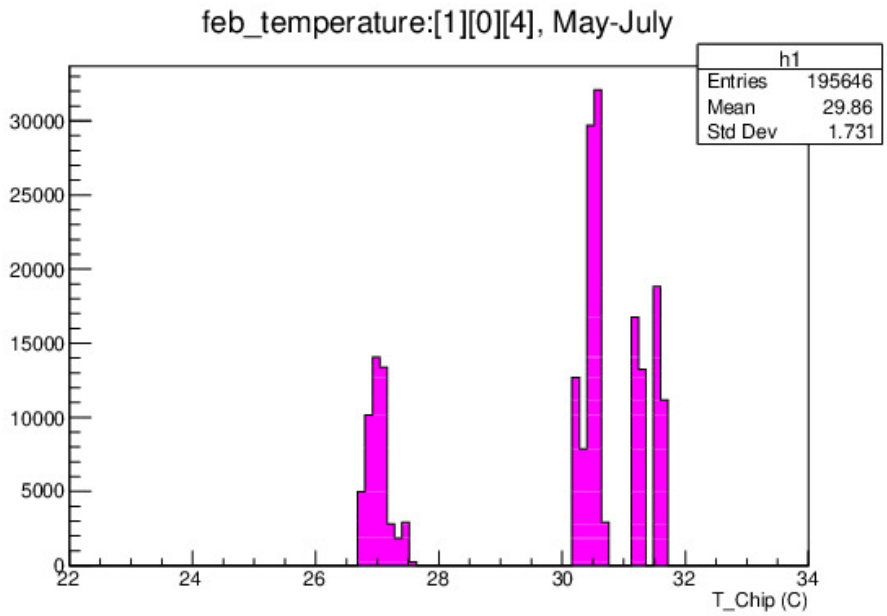

FIGURE B.8: Chip Temperature FEB 104, May-July

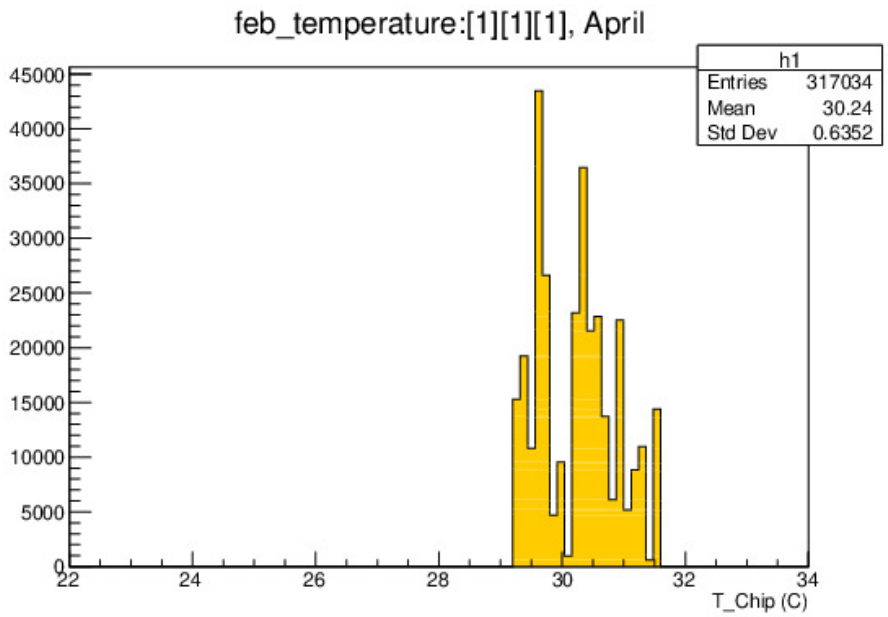

FIGURE B.9: Chip Temperature FEB 111, April

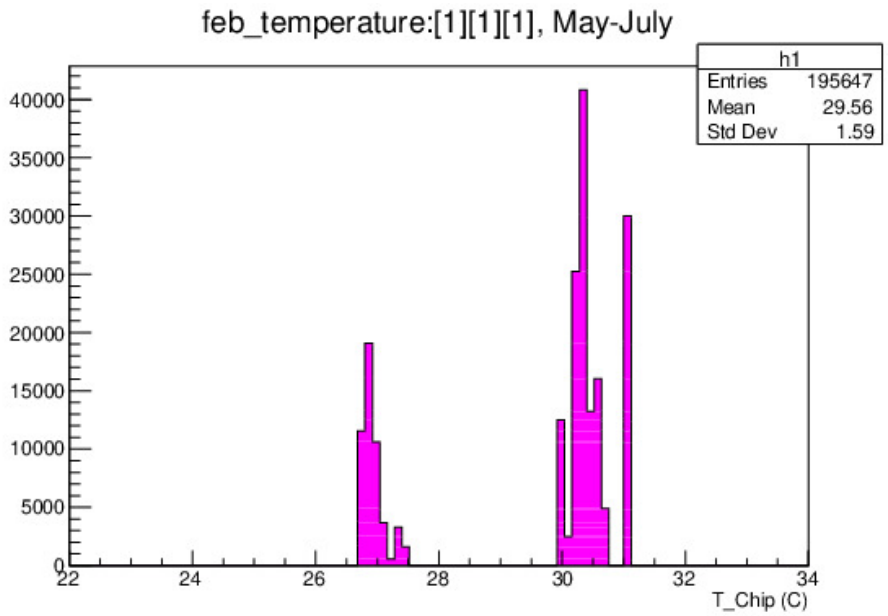

FIGURE B.10: Chip Temperature FEB 111, May-July

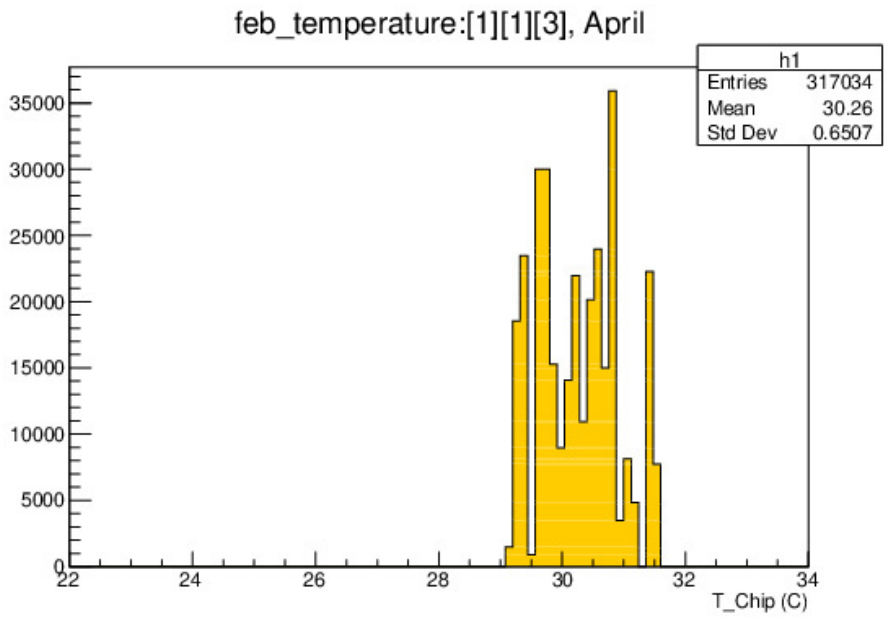

FIGURE B.11: Chip Temperature FEB 113, April

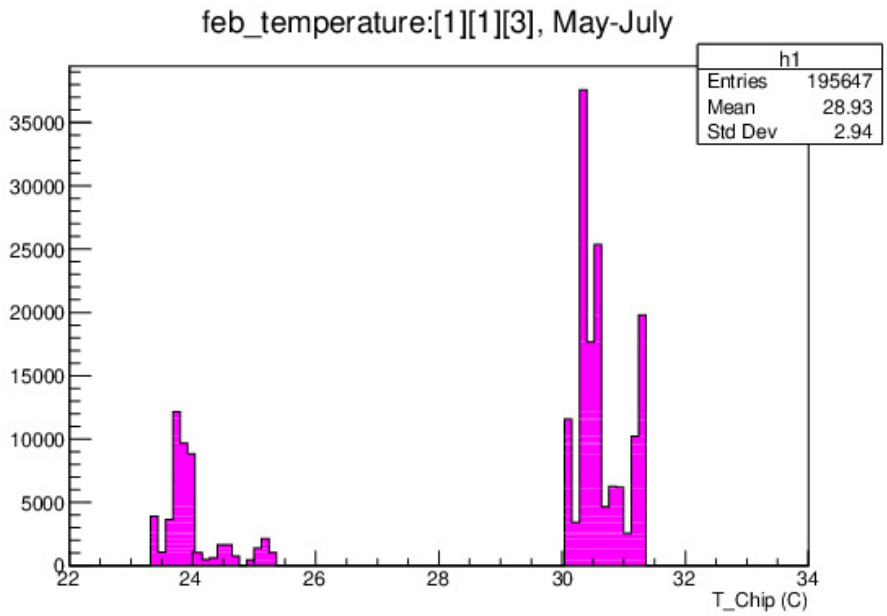

FIGURE B.12: Chip Temperature FEB 113, May-July

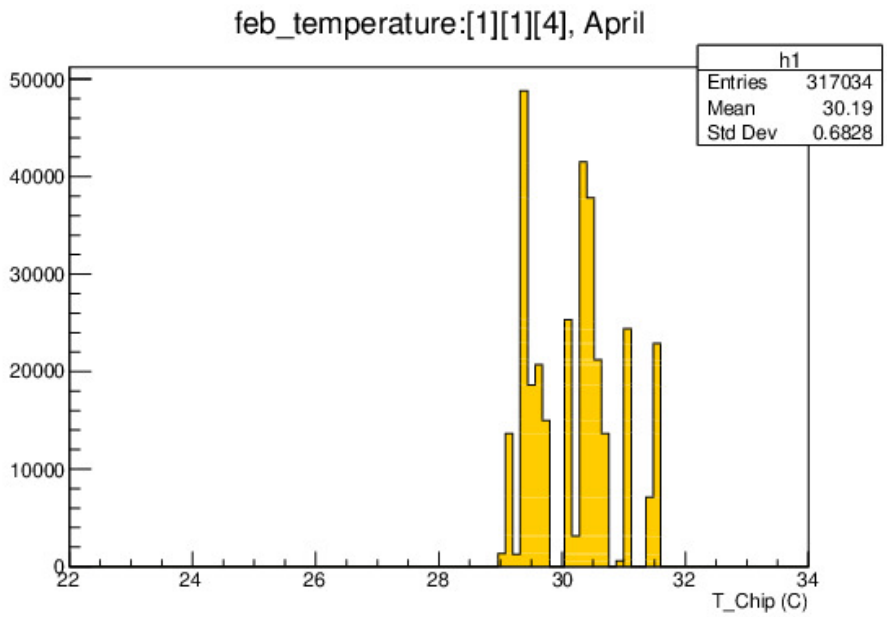

FIGURE B.13: Chip Temperature FEB 114, April

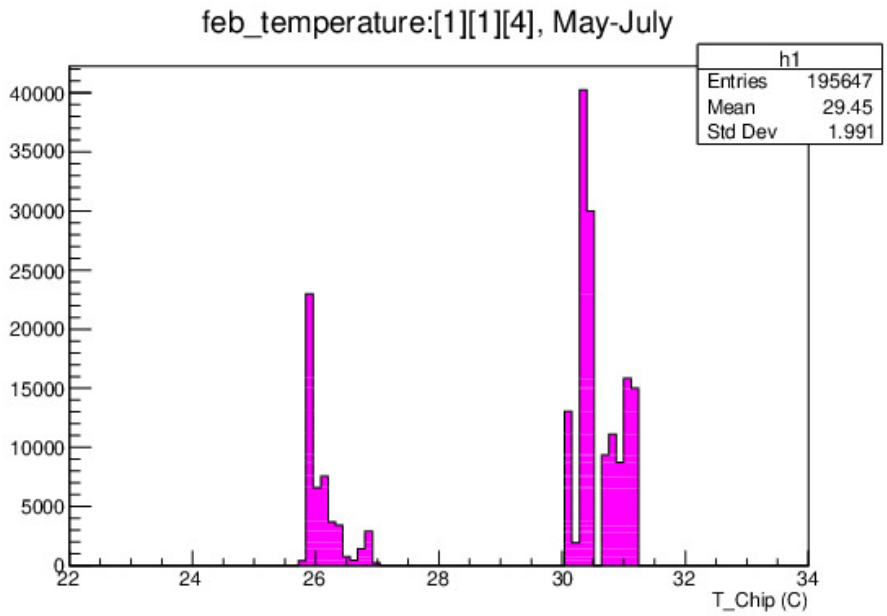

FIGURE B.14: Chip Temperature FEB 114, May-July

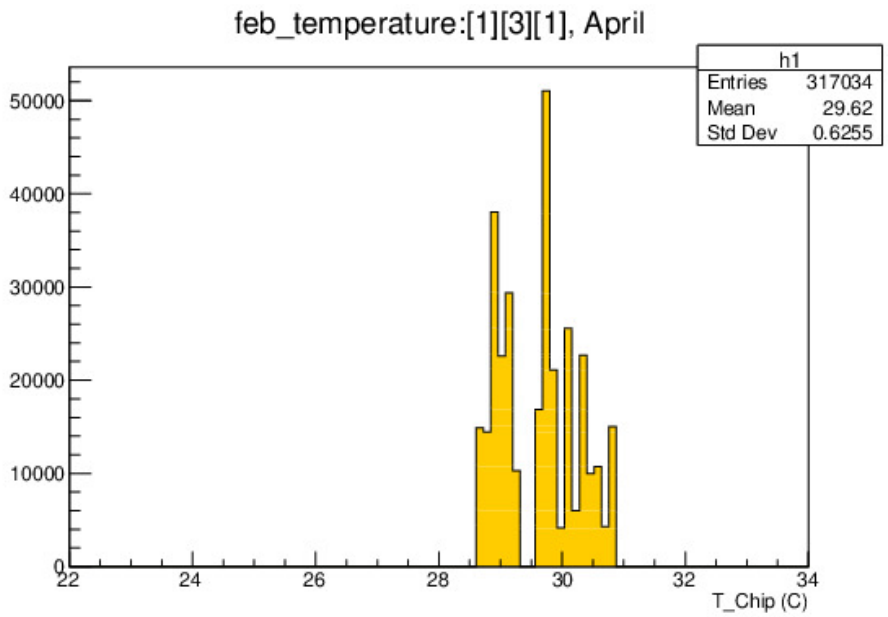

FIGURE B.15: Chip Temperature FEB 131, April

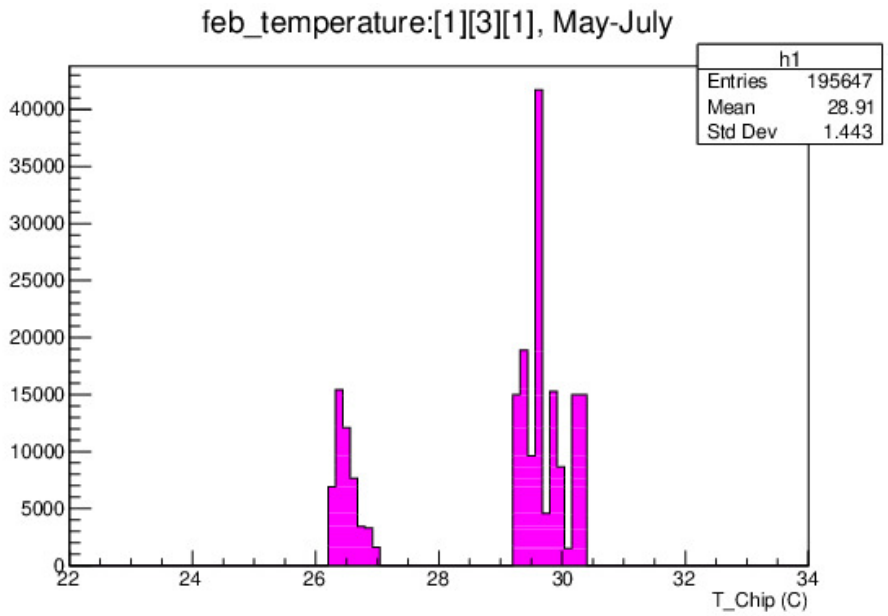

FIGURE B.16: Chip Temperature FEB 131, May-July

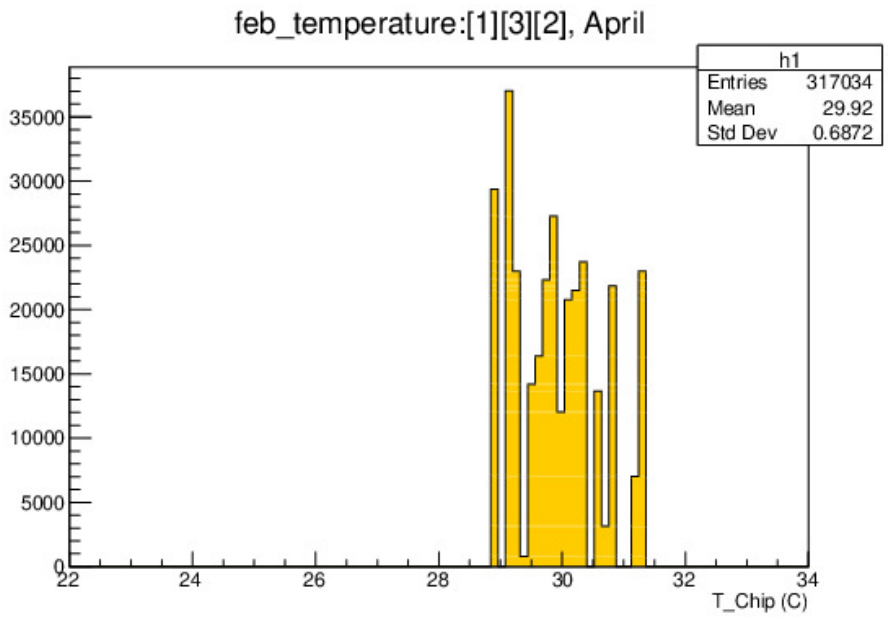

FIGURE B.17: Chip Temperature FEB 132, April

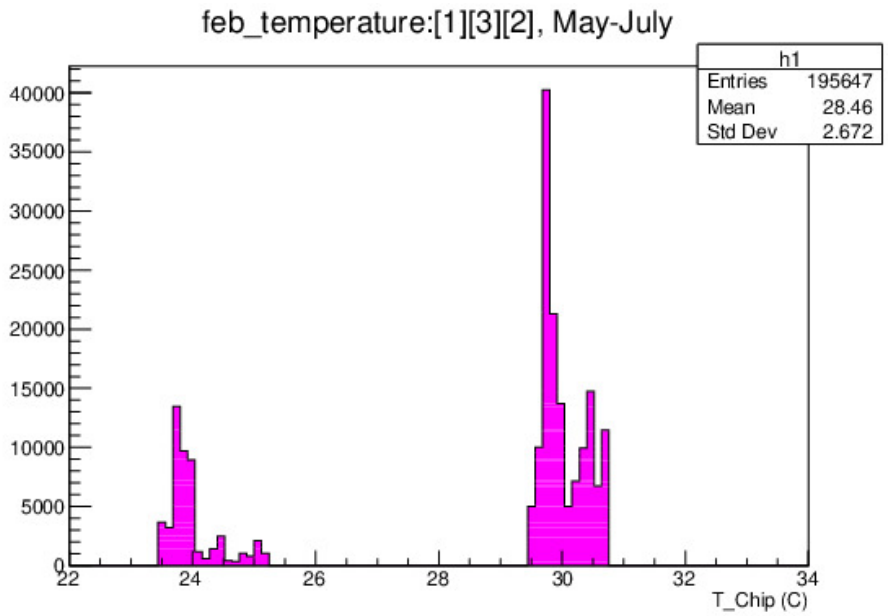

FIGURE B.18: Chip Temperature FEB 132, May-July

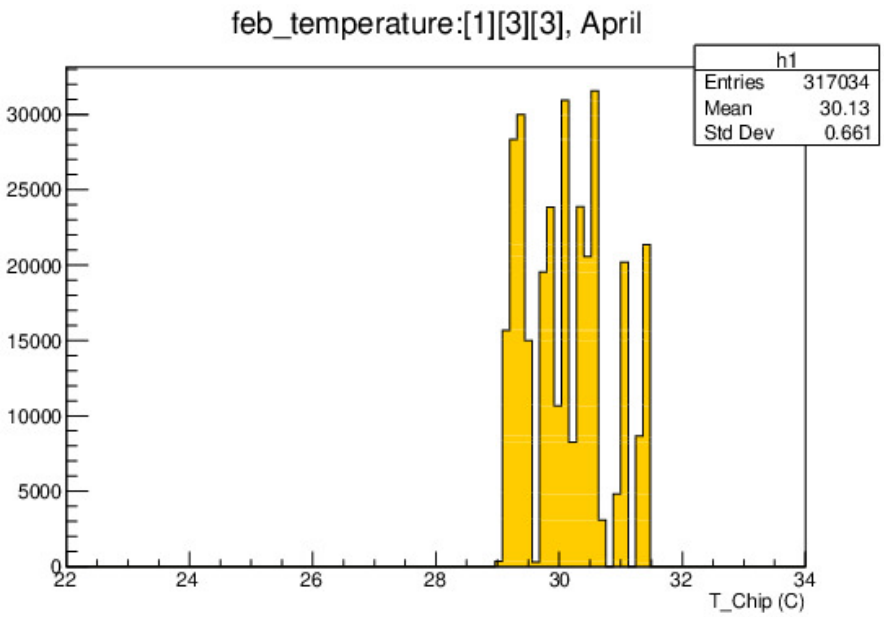

FIGURE B.19: Chip Temperature FEB 133, April

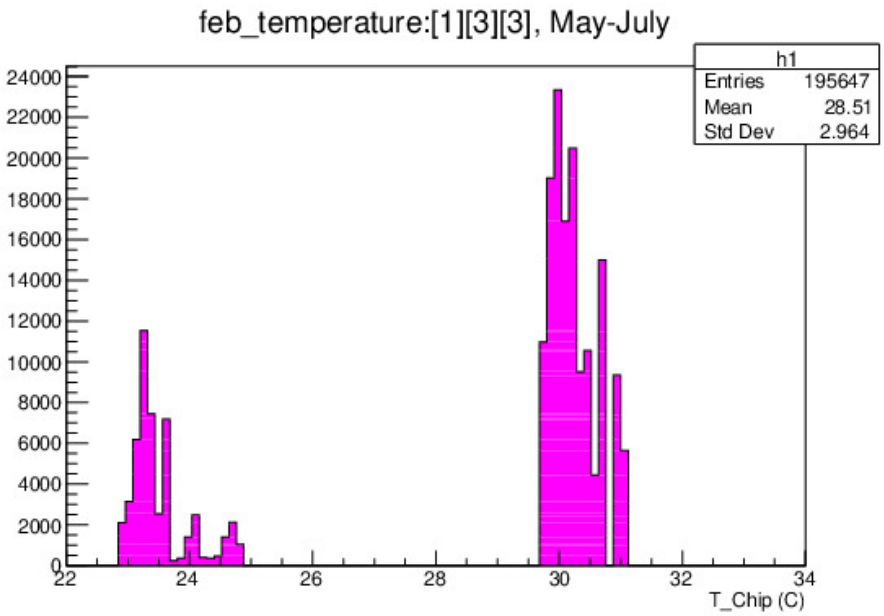

FIGURE B.20: Chip Temperature FEB 133, May-July

FEB	T_{chip} (April)	T_{chip} (May-July)
[1][0][1]	30.44	29.71
[1][0][2]	30.13	29.59
[1][0][3]	29.60	29.03
[1][0][4]	30.45	29.86
[1][1][1]	30.24	29.56
[1][1][3]	30.26	28.93
[1][1][4]	30.19	29.45
[1][3][1]	29.62	28.91
[1][3][2]	29.92	28.46
[1][3][3]	30.13	28.51
[1][3][4]	29.75	28.83
[2][0][1]	30.20	29.56
[2][0][2]	30.18	29.60
[2][0][3]	29.58	28.76
[2][0][4]	30.01	29.47
[2][0][5]	30.37	29.99
[2][1][1]	30.23	29.28
[2][1][2]	30.35	28.84
[2][1][3]	30.65	28.91
[2][1][4]	29.92	28.72
[2][2][1]	30.72	29.85
[2][2][2]	30.40	29.57
[2][2][3]	30.15	29.26
[2][2][4]	29.88	29.22
[2][3][1]	29.95	28.78
[2][3][2]	29.79	28.45
[2][3][3]	30.08	28.35
[2][3][4]	29.83	28.24
[3][0][1]	30.64	29.61
[3][0][2]	30.45	29.58
[3][0][3]	30.00	29.22
[3][0][4]	30.15	29.33
[3][0][5]	30.37	29.21
[3][1][1]	29.33	28.22
[3][1][2]	29.68	28.34
[3][1][3]	29.69	27.86
[3][1][4]	29.75	28.12
[3][2][1]	30.64	30.11
[3][2][2]	30.36	29.96
[3][2][3]	29.57	28.97
mean value	30.10	29.12

TABLE B.1: Summary table of T_{chip} temperatures for April and May-July. Is summarizes the mean values of the histograms from pages 141 to 180.

Appendix C

Gain and Gain Uncertainties in MINERVνA Test Beam Experiment

In Chapter 4, the following formulas were introduced: 4.1 and 4.2. Precisely here, in this section, it will be shown the recipe how to proceed to prove such expressions.
The main assumption that one makes is that the number of photo-electrons per event, the secondary electrons produced by each primary electron at each step of the dynode chain are well-described by Poisson-like Distributions [10].

C.0.1 The Electron Probability Distribution

In the following lines, an expression that tells the probability of the number of electrons at a given dynode is derived. Let's say that the number of photo-electrons in the cathode is λ_1, the probability of getting k_1 photo-electrons arriving at the first dynode, is [11]:

$$P(k_1) = e^{-\lambda_1} \frac{\lambda_1^{k_1}}{k_1!} \tag{C.1}$$

The probability of finding k_2 electrons after the first dynode can be computed by the following:

$$P(k_2) = \sum_{k_1=0}^{\infty} P(k_1).P(k_2|k_1) \tag{C.2}$$

Every single of the k_1 electrons gets a Poisson–distributed probability response from the dynode with an average gain of λ_s (from the first dynode). This turn out in a total Poisson Distribution with mean $\lambda_2 \cdot k_1$:

$$P(k_2|k_1) = e^{-\lambda_2 k_1} \frac{(\lambda_2 k_1)^{k_2}}{k_2!} \tag{C.3}$$

Doing some manipulations one gets [11]:

$$P(k_2) = e^{-\lambda_1} \frac{\lambda_2^{k_2}}{k_2!} \sum_{k_1=0}^{\infty} \frac{(\lambda_1 e^{-\lambda_2})^{k_1}}{k_1!} k_1^{k_2} \tag{C.4}$$

Generalizing for n-1 dynodes [11]:

$$P(k_n) = e^{-\lambda_n}\frac{\lambda_n^{k_n}}{k_n!} \sum_{k_1=0}^{\infty}\sum_{k_2=0}^{\infty}\cdots\sum_{k_{n-1}=0}^{\infty} \frac{(\lambda_1 e^{-\lambda_2})^{k_1}}{k_1!}\frac{(\lambda_2 e^{-\lambda_3}k_1)^{k_2}}{k_2!} \frac{(\lambda_3 e^{-\lambda_4}k_2)^{k_3}}{k_3!}\cdots \frac{(\lambda_{n-1}e^{-\lambda_n}k_{n-2})^{k_{n-1}}}{k_{n-1}!}k_{n-1}^{k_n} \tag{C.5}$$

Doing some Algebra, one gets the variance σ_N^2 of P(k_n), being σ_P^2 the pedestal standard deviation [10]:

$$\sigma_N^2 = \sigma_P^2 + \lambda g^2 e^2 + \lambda g^2 e^2 w^2 \tag{C.6}$$

where the product of the dynode gains, $\prod_{n=1}^{N} g_n = g$ is defined as the gain g of the pixel (in particular, the PMT used in this thesis has 64 channels or pixels), and w^2 is defined as [10]:

$$w^2 = \sum_{j=1}^{N}(\prod_{i=1}^{j}\frac{1}{g_i}) \tag{C.7}$$

Being the actual definition of gain as [10]:

$$g = \frac{\overline{Q}}{\lambda e} \tag{C.8}$$

Solving equations C.6 and C.8 for g, one gets the formula showed in Chapter 4 and [10]:

$$g = \frac{\sigma_N^2 - \sigma_P^2}{\overline{Q}(1+w^2)} \tag{C.9}$$

Equation C.9 is not enough to compute each individual pixel gain because inserting w, introduces N unknown parameters g_n. The number of unknown parameters drops dramatically to one by stating a model where each dynode gain is proportional to a power of V_n, this is the potential difference that accelerates each photo-electron hitting the n-th dynode [10]:

$$g_n \propto V_n^{\alpha} \tag{C.10}$$

The parameter α typically has values between 0.7 and 0.8 and can be gauged by getting LI data while changing the PMT high voltage. On the other hand, MINERνA considers α = 0.75 for each pixel, which results in less than 1% systematic error on the gain measurement. The high voltage applied to

each MINERνA PMT is divided amongst the dynodes according to the optimal ratios recommended by Hamamatsu (see table1.6) (3:2:2:1:1:1:1:1:1:1:1:2:5), where the last amplification step holds for the potential difference among the 12-th dynode and the anode (8×8 multi-anode). Making use of the Hamamatsu ratios and equation C.10 each g_n can be expressed as a function of g_1 only. Doing the math, one gets the following equation [10]:

$$g_1 = g^{\frac{1}{12}} \frac{177147^{\frac{\alpha}{8}}}{8} \tag{C.11}$$

Now, one can insert equation C.11 into equation C.9. The resulting expression does not have an analytic solution, so MINERνA uses a recursive procedure to simultaneously calculate w and g [10]:

1 Compute the pixel gain using equation C.9 and a value for w generated in the previous iteration of this procedure. $1 + w^2 = 1.24$ is used for the first iteration.

2 Use equation C.11 and the gain from the previous step to calculate g_1

3 Use equations C.7 and C.10 , and the computed value g_1 to solve $1 + w^2$.

4 If the w got in step 3 and the w provided in step 1 is less than 0.001%, use the current value of w to calculate the gain. If not, go back to step 1 with the value of w computed in step 3.

This procedure usually converges to the desired value after two loops.

C.0.2 Gain Uncertainty

"The statistical uncertainty is calculated by taking the derivative of equation C.9 and then assuming that each source of statistical uncertainty is uncorrelated and Gaussian. The resulting equation is [10]:"

$$\sigma_g = g\sqrt{\frac{2}{(\sigma_Q^2 - \sigma_P^2)^2}\left(\frac{\sigma_Q^4}{N_Q - 1} + \frac{\sigma_P^4}{N_P - 1}\right) + \frac{1}{Q^2}\left(\frac{\sigma_Q^2}{N_Q} + \frac{\sigma_P^2}{N_P}\right)} \tag{C.12}$$

Where N is the number of LI gates used to compute that anode charge distribution, and N_p is the number of gates used to measure the pedestal mean and variance. In computing C.12, it is stated that w^2 is constant. This hypothesis is acceptable because w_2 only varies by less than $\%1$ over an order of magnitude of gains [10].

C.0.3 Gain Measurements and Electronics Read-out

A typical gain measurement assumes that there is one hit per channel per gate, in this way one expects that the LI data was taken with discriminators on or off. [1] The information whether the discriminators are on or off is not saved by the DAQ, this information is usually obtained from the data. This can be done by knowing whether any hit triggered their discriminator in the very first LI gate. If the discriminators are on, it can also know whether all ADC pipelines [23] were taken by the algorithm or if the deepest pipeline was taken [2]. The pipeline readout status is determined by finding channels with more than one hit in the gate. If every channel has only one hit, then the data is deepest pipeline data [10].

The algorithm used to compute the pixel gains is modified depending on the discriminator mode and pipeline readout status. If discriminators are off, each channel has only one hit per gate and these hits are not very useful because lack of timing information. It is considered that each hit comes from an LI pulse and the charge of the hit is used to compute the mean and variance of the anode charge distribution [10].

If the discriminators are on and all pipelines are read out, each channel may have more than one hit per gate. These hits may be formed from a few sources: LI pulses, PMT after-pulsing, and dark noise that fluctuates above the discriminator threshold. The charges of these hits cannot be added together to duplicate the discriminator-off result because of discriminator dead time. Instead, the discriminator timing information is used to find the time window during which the LI pulses arrives at the PMTs. This time window is set to be the clock tick that corresponds to the timing information of the greatest number of hits, plus and minus ten clock ticks. All hits outside of this time window is rejected, and the hit inside the window is used to calculate the mean and variance of the anode charge distribution. If there is no hit inside the LI time window, the channel is assigned a new hit with a pedestal-subtracted charge of zero fluctuated about a width equal to the pedestal width. This ensures that zeroes [3] are counted correctly [10].
If the discriminators are on but only the deepest pipeline is read out, the procedure is similar to the procedure where all pipelines are read out, with one important difference: pedestal hits are not added to channels that do not have a hit inside the LI time window. This is omitted due to an effect from integrating TriP-t [25] chips in triplets that only occurs during deepest pipeline runs. The effect causes one or more of the earliest hits in the channels on a triplet of TriP-t chips to be lost during readout. With the hit lost, it is unknown whether it could have occurred during the LI time window or not.

[1] If discriminators are on, it might be more than one hit in a channel due PMT after-pulsing [24] is triggering the discriminator. If discriminators are off, each channel has one hit with PMT anode charge summed over the entire gate (there are 2000) gates per LI run.

[2] If it is the case that the deepest pipeline is read, then the DAQ only stores the earliest hit in a channel. This is the default setting for LI data that is read out between beam gates.

[3] A "zero" is a gate in which zero PEs reach the first dynode.

Therefore, a missing hit in the LI time window does not indicate that there was a pedestal hit. This difference between deepest pipeline and all pipeline data is very small; the gains measured are similar in both cases [10].

The light injection system is also used to calibrate PMTs on the test beam detector. The discriminator-off test beam LI data contains occasional hits with charges that are much larger than can be created by the LI system. These hits can have a large effect on the measurement of the gain by pulling the variance of the anode charge distribution. An outlier rejection scheme is implemented to remove these hits and is used on all data, regardless of discriminator status, because it introduces less than 1% systematic uncertainty [10].

The outlier rejection scheme works by sorting the hits in a channel in order of ascending charge. It then searches for the first occurrence of a consecutive pair of charges with a charge greater than the mean of the charge distribution and with a charge difference more than 300 fC. For a typical photomultiplier pixel, this charge difference is equal to 3.75 PEs (photo-electrons), and such a pair of charges is likely to be located in the very end of the high-side tail of the anode charge distribution. If such a pair is found, all hits with charges equal to or greater than the charge of the higher-charged hit in the pair are removed from the anode charge distribution [10].

Front End Boards

The FEBs serve two roles: supply high voltage to the PMTs via a Cockroft-Walton generator and read out the PMT anode charge. Before read out, capacitative dividers split the charge from each pixel into low, medium, and high gain channels. This splitting increases dynamic range while maintaining fine resolution on signals that are only a few photoelectrons. Read out is handled by six 32-channel Application-Specific Integrated Circuit (ASIC) chips, called TriP-t chips [12], that integrate, time-stamp, and digitize the anode charge. Digitization is handled by 12 bit Analog-to-Digital Converters (ADCs). FEB operation is controlled by a Spartan 3E Field-Programmable Gate Array (FPGA) chip, which also decodes incoming timing signals [10].

The first four TriP-t chips, numbered 0-3, read out the high and medium gain channels, while TriP-t chips 4-5 handle the low gain channels. The high and medium gain channels of a single pixel are always read out by the same TriP-t chip; under this requirement, each of the chips 0-3 read out 16 high gain channels and 16 medium gain channels. The result of this configuration is that two TriP-t chips are used to read out the three gain ranges of a single pixel. In order to avoid ambiguity during the read out process, the TriP-t chips are organized into two triplets: chips (0,1,4) and chips (2,3,5). Each triplet contains full low, medium, and high gain information for 32 pixels [10].

The fundamental unit of time on a TriP-t chip is called a clock tick, approximately 9.4 ns. The clock tick is set by a 53.1 MHz crystal contained within a master timing module that distributes a timing signal to all other read out electronics. Additionally, during charge integration, a quadrature circuit is used to achieve quarter-tick timing resolution, approximately 2.4 ns. Charge is time-stamped by the channel's discriminator, which triggers when the integrated charge exceeds a certain threshold.

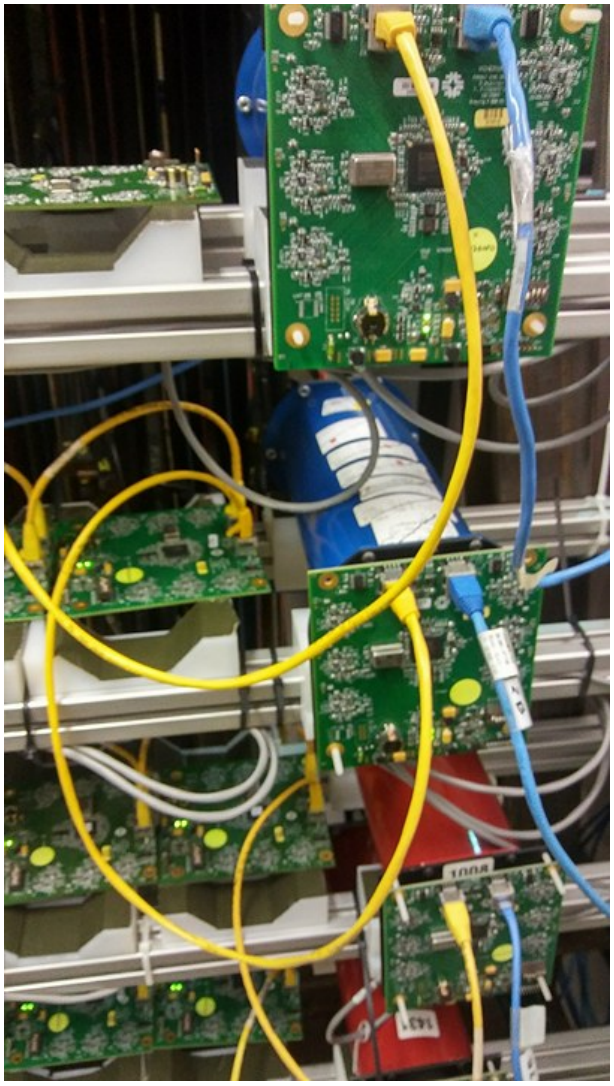

FIGURE C.1: FEBs mounted in Lab F Facility (Fermilab)

In practice, only the high gain discriminators are used because any charge that triggers a pixel's high gain discriminator will also trigger its medium and low gain discriminators. Time on each FEB is measured relative to a local counter. The counters are initialized taking into account differences in signal propagation time, synchronizing the timing across all FEBs to within one clock tick [10].
Read out is organized into gates. A gate is a 1702 clock tick (16 μs) window that starts 500 ns before the arrival of the beam spill and ends 5.5 μs after the spill ends. The TriP-t chip triplets are able to independently integrate and time-stamp their channels' charges up to seven times per gate. A triplet begins integration when one of its high gain discriminators is triggered. The integration window lasts for 16 clock ticks (150 ns), then the integrated charge is pushed into the chip's ADC pipeline; each instance of integrated charge in the ADC pipeline is called a hit. All channels on the triplet are time-stamped with T_0 , the clock tick of the earliest triggered high gain discriminator [10].
Subsequent discriminator triggers during the integration window are time-stamped with delay and quarter ticks relative to T_0 . The integrators are then reset in preparation for the next integration window. The reset requires 20 clock ticks (188 ns). After the end of the gate, all hits in the ADC

pipelines are digitized.

There a two sources of electronics dead time that arise from FEB operation. The first occurs during the reset period after an integration window. Any charge that arrives at the TriP-t chip triplet during reset is not integrated. This primarily affects read out of decay activity and neutrino interactions that are close in time and spatially overlap. The other form of dead time occurs when a triplet reaches its limit of seven time-stamped integration windows within a gate. All subsequent charge is integrated and pushed into the ADC pipeline at the end of the gate, but does not receive a time stamp [10].

Data Acquisition

The FEBs are daisy-chained into groups of nine or ten with standard ethernet cables. Both ends of the chain are connected to a custom VME module called the Chain Readout Controller (CROC), which can service up to four chains. The CROC reads out its FEBs after each gate and is also responsible for sending instructions and timing information. CROCs receive timing information from another custom VME module called the CROC Interface Module (CRIM). The CRIMs collect timing information from MINOS, which is used for event-matching between the two detectors, and the MINERA Timing Module (MvTM), which receives timing information from the Main Injector and contains the 53.1 MHz timing synchronization crystal. The signal from the MvTM controls the start of each gate relative to the beam spill. Additionally, one CRIM serves as the master CRIM, and is tasked with distributing timing triggers to the other CRIMS when collecting light injection data (see Sec. 4.1.3). In full detector running, MINERA uses two VME crates, each of which contains a CAEN V2718 Crate Controller, two CRIMS, and seven or eight CROCs. The crates are controlled and read out by separate computers installed with a CAEN A2818 PCI Card that communicates with the V2718 Crate Controller [10].

Bibliography

[1] William R. Leo. *Techniques for Nuclear and Particle Physics Experiments A how-to Approach.* Springer-Verlag, Heidelberg, Berlin, (1987).

[2] Hamamatsu Electronics. *MULTIPLIER TUBES Basics and Aplications.* HAMAMATSU PHOTONICS K. K, Japan, (2007)

[3] Jaewon Park. *Gaudi Framework.* MINERνA internal document (2018), DocDB document 10024.

[4] ROOT Collaboration. *ROOT User's Guide.* Springer-Verlag, Heidelberg, CERN, (2013).

[5] F. James. *MINUIT, Function Minimization and Error Analysis.* Computing and Network Division, Version 94.1, CERN, (1998).

[6] L. Aliaga et al. *MINERνA neutrino detector response measured with test beam data.* Nuclear Instruments and Methods in Physics Research Section A: Accelerators, Spectrometers, Detectors and Associated Equipment 789 (2015): 28-42.

[7] L. Aliaga et al. *Design, Calibration, and Performance of the MINERνA Detector.* Nucl.Instrum.Meth. A743 (2014) 130–159.

[8] N. Tagg, et al. *Arachne - A web-based event viewer for MINERνA.* Nucl.Instrum.Meth. A694 (2012) 179–192.

[9] G. Perdue, et al. *The MINERνA Data Acquisition System and Infrastructure.* Nucl.Instrum.Meth. A694 (2012) 179–192.

[10] B. Eberly,PhD Thesis. *CHARACTERIZATION OF FINAL STATE INTERACTION STRENGTH IN PLASTIC SCINTILLATOR BY MUON-NEUTRINO CHARGED CURRENT CHARGED PION PRODUCTION.* Diss. University of Pittsburgh, 2014.

[11] Jonas Rademacker. *An Exact Formula to Describe the Amplification Process in a Photomultiplier Tube.* Nuclear Instruments and Methods in Physics Research Section A: Accelerators, Spectrometers, Detectors and Associated Equipment 484.1-3 (2002): 432-443.

[12] J. Estrada, C. Garcia, B. Hoeneisen, and P. Rubinov. *MCM II and the TriP Chip. FERMILAB-TM-2226.* United States. Department of Energy. Office of Energy Research, 2003.

[13] https://root.cern.ch/pyroot

[14] https://www.science.mcmaster.ca/radgrad/images/6R06CourseResources/4R6Notes4_ScintillationDetectors.pdf

[15] http://www-physics.lbl.gov/~spieler/physics_198_notes/PDF/III-Scint.pdf

[16] http://www.nbi.dk/~xella/lecture_16Feb2009.pdf

[17] https://www-zeuthen.desy.de/~middell/public/pyroot/pyroot.html

[18] http://www.dailyherald.com/article/20150730/news/150739889/

[19] John R. Taylor *An Introduction to Error Analysis: The Study of Uncertainties in Physical Measurements.* University Science Books, 1997

[20] http://www.fnal.gov/

[21] http://minerva.fnal.gov/

[22] https://en.wikipedia.org/wiki/Robert_R._Wilson

[23] Ben Messerly. *MINERνA 101 Calibrations.* MINERνA internal document (2017), DocDB document 14579.

[24] Joel Mousseau. *The Even Crazier World of Veto Wall After Pulsing.* MINERνA internal document (2010), DocDB document 5239.

[25] Paul Rubinov and Leo Bellantoni. *TriP-T production version Testing Report.* MINERνA internal document (2005), DocDB document 90.

[26] E. Chavarria, J. Solano et al. *Measurement of total and differential cross sections of neutrino and antineutrino coherent $\pi^{\pm}$ production on carbon.* PHYSICAL REVIEW D 97, 032014 (2018)

[27] E. Chavarria, J. Solano et al. *Measurement of the muon antineutrino double-differential cross section for quasielastic-like scattering on hydrocarbon at $E_{\nu} \sim 3.5GeV$.* PHYSICAL REVIEW D 97, 052002 (2018)

[28] Ch. Berger and L. M. Sehgal. *Partially conserved axial vector current and coherent pion production by low energy neutrinos* Physical Review D 79.5 (2009): 053003.

[29] S. Agostinelli et al. *Geant4—a simulation toolkit.* Nuclear instruments and methods in physics research section A: Accelerators, Spectrometers, Detectors and Associated Equipment 506.3 (2003): 250-303.

[30] L. Aliaga et al. *Neutrino flux predictions for the NuMI beam.* Physical Review D 94.9 (2016): 092005.

[31] D. G. Michael et al. *The magnetized steel and scintillator calorimeters of the MINOS experiment.* Nuclear Instruments and Methods in Physics Research Section A: Accelerators, Spectrometers, Detectors and Associated Equipment 596.2 (2008): 190-228.

[32] Costas Andreopoulos, et al. *The GENIE Neutrino Monte Carlo Generator: Physics and User Manual.* arXiv preprint arXiv:1510.05494 (2015).

[33] K. Abe et al. *Measurements of neutrino oscillation in appearance and disappearance channels by the T2K experiment with* 6.6×10^{20} *protons on target.* Physical Review D 91.7 (2015): 072010.

[34] L. Fields et al. *Measurement of Muon Antineutrino Quasielastic Scattering on a Hydrocarbon Target at* $E_\nu \approx 3.5GeV$. Physical review letters 111.2 (2013): 022501.

[35] C.H.Llewellyn Smith. *Neutrino reactions at accelerator energies.* Phys. Rept. 3.SLAC-PUB-0958 (1971): 261-379.

[36] B. Bhattacharya, R. J. Hill, and G. Paz. *Model-independent determination of the axial mass parameter in quasielastic neutrino-nucleon scattering.* Physical Review D 84.7 (2011): 073006.

[37] R. Smith and E. Moniz. *Neutrino reactions on nuclear targets.* Nuclear Physics B 43 (1972): 605-622.

[38] J. W. Negele. *Structure of Finite Nuclei in the Local-Density Approximation.* Physical review C 1.4 (1970): 1260.

[39] J. A. Maruhn, P. G. Reinhard, and E. Suraud. *Simple Models of Many-Fermion Systems.* (Springer-Verlag, Berlin, 2009).

[40] J. Arrington, D. Higinbotham, G. Rosner, and M. Sargsian. *Hard probes of short-range nucleon–nucleon correlations.* Progress in Particle and Nuclear Physics 67.4 (2012): 898-938.

[41] K. Egiyan et al. *Measurement of Two- and Three-Nucleon Short-Range Correlation Probabilities in Nuclei.* Physical review letters 96.8 (2006): 082501.

[42] R. Shneor et al. *Investigation of Proton-Proton Short-Range Correlations via the* $^{12}C(e, e', pp)$ *Reaction.* Physical review letters 99.7 (2007): 072501.

[43] R. Subedi et al. *Probing Cold Dense Nuclear Matter.* Science (2008).

[44] A. Bodek and J. L. Ritchie. *Fermi-motion effects in deep-inelastic lepton scattering from nuclear targets.* Physical Review D 23.5 (1981): 1070.

[45] K. Gottfried. *The determination of the nuclear pair correlation function and momentum distribution.* Annals of Physics 21.1 (1963): 29-46.

[46] A. Bodek, H. Budd, and M. Christy. *Neutrino quasielastic scattering on nuclear targets.* The European Physical Journal C 71.9 (2011): 1726.

[47] J. Carlson, J. Jourdan, R. Schiavilla, and I. Sick. *Longitudinal and transverse quasielastic response functions of light nuclei.* Physical Review C 65.2 (2002): 024002.

[48] V. Mamyan, Ph.D. thesis, University of Virginia, 2010. https://arxiv.org/abs/1202.1457

[49] A. A. Aguilar-Arevalo et al. *First measurement of the muon neutrino charged current quasielastic double differential cross section.* Physical Review D 81.9 (2010): 092005.

[50] V. Lyubushkin et al. *A study of quasi-elastic muon neutrino and antineutrino scattering in the NOMAD experiment.* The European Physical Journal C 63.3 (2009): 355-381.

[51] J. Morfín, J. Nieves, and J. Sobczyk. *Recent Developments in Neutrino/Antineutrino-Nucleus Interactions.* Advances in High Energy Physics 2012 (2012).

[52] *Scintillators for the physical sciences.* Enterprises, Nuclear (1982).

[53] http://ftbf.fnal.gov/

[54] B. Everly et al. *Test beam detector calibrations.* MINERνA Technical Note No. 018 (2014), DocDB document 8686.

[55] B. Everly et al. *Light Injection Calibration System.* MINERνA internal document (2006), DocDB document 1012.

[56] C. Marshal. *Test Beam energy scale systematics from temperature effect* MINERνA internal document (2012), DocDB document 7558.

[57] DAMPE Collaboration. *Temperature dependence of the plastic scintillator detector for DAMPE* Chinese Physics C Vol. 41, No. 1 (2017) 016001.

[58] MINERν Collaboration. *Photographic Examination of Light Injection into PMT Boxes for the MINERνA Calibration System* MINERνA internal Document (2006), DocDB document 868

[59] https://byjus.com/physics/thermal-equilibrium\-and-zeroth-law-of-thermodynamics/